Alma Mater Studiorum
Università degli Studi di Bologna

SCUOLA DI SCIENZE
Dipartimento di Fisica e Astronomia
Corso di Laurea Magistrale in Astrofisica e Cosmologia

Jeans modeling of massive early-type galaxies with observed stellar kinematic profiles up to 2-3 effective radii

Tesi di Laurea Magistrale

Presentata da:
Gregorio Vettori

Relatrice:
Chiar.ma Prof. Silvia Pellegrini

Sessione IV
Anno Accademico 2021/2022

a mia Nonna e ai miei Genitori

The important thing is not to stop questioning.
Curiosity has its own reason for existence.

Albert Einstein

Table of contents

Abstract

A recent integral-field spectroscopic (IFS) survey, the MASSIVE survey (Ma et al. 2014), observed the 116 most massive ($M_K < -25.3$ mag, stellar mass $M_* > 10^{11.6}\,\mathrm{M}_\odot$) early-type galaxies (ETGs) within 108 Mpc, out to radii as large as 40 kpc, that correspond to $\sim 2-3$ effective radii (R_e). One of the major findings of the MASSIVE survey is that the galaxy sample is split nearly equally among three groups showing three different velocity dispersion profiles $\sigma(R)$ outer of a radius $\sim 5\,\mathrm{kpc}$ (falling, flat and rising with radius). The purpose of this thesis is to model the kinematic profiles of six ETGs included in the MASSIVE survey and representative of the three observed $\sigma(R)$ shapes, with the aim of investigating their dynamical structure.

Models for the chosen galaxies are built using the numerical code JASMINE (Posacki, Pellegrini, and Ciotti 2013). The code produces models of axisymmetric galaxies, based on the solution of the Jeans equations for a multicomponent gravitational potential (supermassive black hole, stars and dark matter halo). With the aim of having a good agreement between the kinematics obtained from the Jeans equations, and the observed σ and rotation velocity V of MASSIVE (Veale et al. 2016, 2018), I derived constraints on the dark matter distribution and orbital anisotropy.

This work suggests a trend of the dark matter amount and distribution with the shape of the velocity dispersion profiles in the outer regions: the models of galaxies with flat or rising velocity dispersion profiles show higher dark matter fractions f_DM both within 1 R_e and 5 R_e. Orbital anisotropy alone cannot account for the different observed trends of $\sigma(R)$ and has a minor effect compared to variations of the mass profile. Galaxies with similar stellar mass M_* that show different velocity dispersion profiles (from falling to rising) are successfully modelled with a variation of the halo mass M_h.

Sommario

Una recente survey spettroscopica a campo integrale, la survey MASSIVE (Ma et al. (2014)), ha osservato le 116 galassie early-type più massive ($M_K < -25.3$ mag, massa stellare $M_* > 10^{11.6}\,\mathrm{M}_\odot$) entro 108 Mpc, fino a raggi di 40 kpc, che corrispondono a $\sim 2-3$ raggi effettivi (R_e). Uno dei principali risultati della survey MASSIVE è che il campione di galassie è diviso quasi equamente in tre gruppi che mostrano tre diversi profili di dispersione di velocità $\sigma(R)$ oltre un raggio di $\sim 5\,\mathrm{kpc}$ (in calo, piatto e in risalita con il raggio). Lo scopo di questa tesi è quello di modellare i profili cinematici di sei galassie early-type incluse nella survey MASSIVE e rappresentative delle tre forme osservate di $\sigma(R)$, con l'obiettivo di indagare la loro struttura dinamica.

I modelli per le galassie scelte sono costruiti utilizzando il codice numerico JASMINE (Posacki, Pellegrini, and Ciotti 2013). Il codice produce modelli di galassie assisimmetriche, basati sulla soluzione delle equazioni di Jeans per un potenziale gravitazionale multicomponente (buco nero supermassivo, stelle e alone di materia oscura). Con l'obiettivo di avere un buon accordo tra la cinematica ottenuta dalle equazioni di Jeans, e la σ e la velocità di rotazione V osservate di MASSIVE (Veale et al. 2016, 2018), ho derivato dei vincoli sulla distribuzione della materia oscura e sull'anisotropia orbitale.

Questo lavoro suggerisce una correlazione tra la quantità e la distribuzione della materia oscura, e la forma dei profili di dispersione di velocità nelle regioni esterne: i modelli di galassie con profili di dispersione di velocità piatti o in risalita mostrano frazioni di materia oscura f_DM maggiori sia entro 1 R_e che entro 5 R_e. L'anisotropia orbitale da sola non può spiegare i diversi andamenti osservati di $\sigma(R)$ e ha un effetto minore rispetto alle variazioni del profilo di massa. Galassie con massa stellare M_* simile che mostrano profili di dispersione di velocità diversi (da quello in calo a quello in risalita) sono modellate con successo con una variazione della massa dell'alone M_h.

1 Introduction

Early-type galaxies (ETGs) represent the remnants of the major star formation events that occurred in our universe. They include the most massive galaxies and are generally found in dense environments, like the center of galaxy groups or clusters. They are characterised by old stellar populations, high metallicity and low star formation rates ($< 10^{-11}\, M_*\, \mathrm{yr}^{-1}$, where M_* is the stellar mass). They are apparently simple systems, but the derivation of their internal structure and kinematics can be quite challenging and requires the help of high-quality observations. In particular, measuring the stellar velocity dispersion profiles $\sigma(R)$ of early-type galaxies is crucial to estimate their dark matter content, as well to reconstruct their past evolution (Naab et al. 2014; Santucci et al. 2022).

Pre-1990 long-slit observations found most of profiles to decline with radius (Tonry 1985; Franx, Illingworth, and Heckman 1989), with a few exceptions like NGC 4889 and NGC 6909 having flat $\sigma(R)$ out to ~ 10 kpc (Davies and Illingworth 1983). Therefore, rising dispersion profiles were really uncommon. Several 1990s long-slit studies have then focused on brightest group or cluster galaxies (BGGs or BCGs), but again found mostly flat or falling dispersion profiles (Carter, Bridges, and Hau 1999), with just 4 out of 60 galaxies having $\sigma(R)$ rising outward. However, in the last decade it became clearer that rising dispersion profiles may be more common than this, especially at large radius (Murphy, Gebhardt, and Cradit 2014; Smith, Lucey, and Edge 2017). Newman et al. (2013) measured seven more distant BCGs to about 30 kpc, and found all to be strikingly homogeneous in their rising dispersion profiles. Globular cluster (GC) kinematic measurements have identified other galaxies (e.g. NGC 3311) with a rising $\sigma(R)$ (Richtler et al. 2011). GC studies of several other galaxies have found instead flat and falling $\sigma(R)$ (Richtler et al. 2014). Inferring global conclusions from heterogeneous studies can be therefore challenging, since different tracer populations (e.g. GCs and starlight) in general have different spatial distribution and orbital configurations.

In more recent years, Integral Field Spectroscopic (IFS) surveys produce two-dimensional maps of stellar kinematics for large samples of galaxies, providing a much more comprehensive picture of velocity dispersion profiles than 1D long-slit observations. The ATLAS^{3D} survey (Emsellem et al. 2011) measured stellar kinematics for 260 early-type galaxies up to the effective radius R_e (the radius that encloses half of the total galaxy light), but only 6 of these have $M_* > 10^{11.5}\, \mathrm{M}_\odot$ and the survey is volume limited to a distance of 42 Mpc. The SLUGGS survey (Arnold et al. 2014; Brodie et al. 2014) mapped the kinematics of GCs for 25 ATLAS^{3D} galaxies up to $\sim 3\, R_\mathrm{e}$. The SAMI survey (van de Sande et al. 2017) probed ETGs up to $\sim 1 - 2\, R_\mathrm{e}$.

The MASSIVE survey (Ma et al. 2014) is instead designed to systematically investigate the high-mass regime that was little explored in previous surveys. It is a volume-limited, multi-wavelength, integral-field spectroscopic (IFS) and photometric survey of the kinematics of the 116 most massive ($M_K < -25.3$ mag, stellar

mass $M_* > 10^{11.6}\,\mathrm{M}_\odot$) ETGs within 108 Mpc in the northern sky, observed out to radii as large as 40 kpc. Their demographics, structural and environmental properties have been further analysed in a series of papers, considering in particular their: angular momentum, velocity dispersion, higher moments and environment (Ma et al. 2014; Veale et al. 2016, 2017, 2018; Ene et al. 2019, 2020); stellar population trends (Greene et al. 2015, 2019); molecular, hot and warm ionized gas (Davis et al. 2016, 2019; Goulding et al. 2016; Pandya et al. 2017); isophotal and instrinsic shapes (Goullaud et al. 2018; Ene et al. 2018).

One of the many interesting results from these papers is that MASSIVE galaxies present different outer $\sigma(R)$ trends (falling, flat and rising), split nearly equally among the three types. This underlines again the importance of having observations extended up to a few R_e. It was suggested that rising dispersion profiles are caused (at least in part) by variations in the total mass profiles rather than in the velocity anisotropy alone (Veale et al. 2018). Merger history also affects the anisotropy and mass profile of a galaxy (Schauer et al. 2014; van de Sande et al. 2021), and thus its $\sigma(R)$. To investigate this further, in this thesis I make numerical modelings of a representative sub-sample of MASSIVE ETGs, with the aim of recovering important information on their internal structure. The code used for this purpose produces models of axisymmetric galaxies, based on the solution of the Jeans equations for a multicomponent gravitational potential.

In this introductory chapter I illustrate the MASSIVE survey observations and the procedure used by Veale et al. (2018) to quantify the shape of the velocity dispersion profiles. After listing some typical properties of galaxies with a rising $\sigma(R)$, I present the selection criteria adopted to choose the six galaxies studied in this work. In Section 2 I describe the numerical modeling code, focusing on the role of the chosen free parameters and a brief description of the Jeans equations. I present the models in Section 3, investigating the dynamical structure of each galaxy. Finally, I present the results and discuss their implications in Section 4. Appendix A concerns the numerical grid adopted in the code. Appendix B shortly describes the procedure to project the main kinematic quantities of the models and obtain v_los and σ_los, the line-of-sight velocity and velocity dispersion fields, respectively.

1.1 The MASSIVE survey

The MASSIVE survey (Ma et al. 2014) includes the most massive ($M_K < -25.3$ mag, stellar mass $M_* > 10^{11.6}\,\mathrm{M}_\odot$) early-type galaxies (ETGs) within 108 Mpc in the northern sky. In this section I present a brief summary of the observations, focusing in particular on the spectrograph used, the spectral range considered and the adopted binning scheme.

MASSIVE galaxies are observed using the Mitchell/VIRUS-P integral-field spectrograph on the 2.7 m Harlan J. Smith Telescope at McDonald Observatory. The Mitchell spectrograph covers a 107" × 107" field of view and consists of 246 evenly-spaced fibers with a diameter of ∼ 4". The spectral range of the IFS spans 3650-5850 Å, which includes the Ca H+K region, Hβ and several Fe absorption features. The instrumental resolution varies with wavelength and fiber position of approximately 4.5 Å.

The fibers cover annular bins of varying radial size, with the radius of each bin calculated through a luminosity-weighted average of the individual fiber radii. Each annulus is cut into an even number of equal-sized angular bins, with its thickness set to have a signal-to-noise ratio S/N exceeding 20 (right panel of Figure 1). The central fiber typically reaches S/N above 50. An example of the binning scheme used is shown in the left panel of Figure 1.

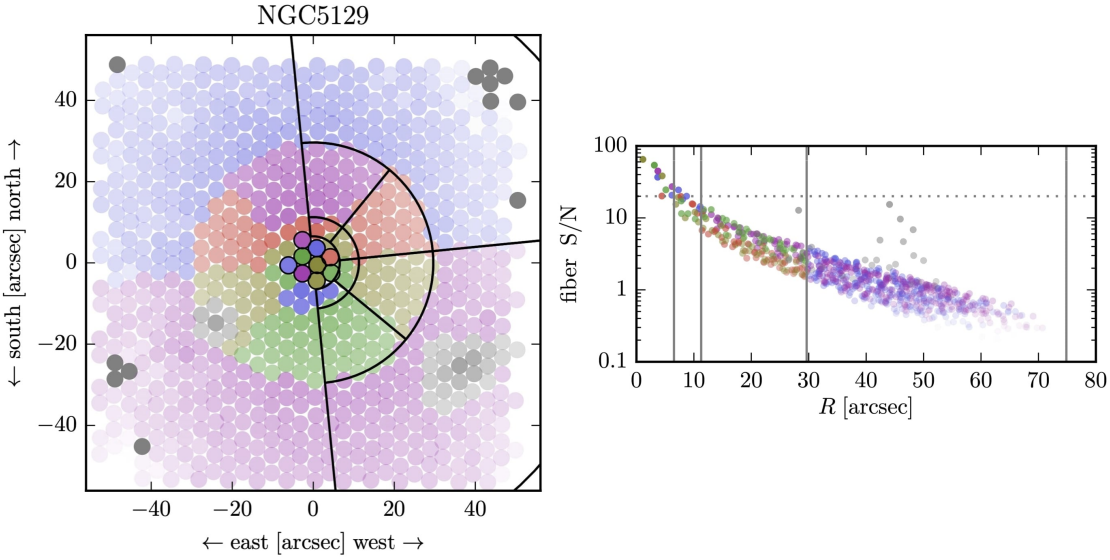

Figure 1: Example binning scheme for NGC 5129 (left panel). All fibers have a radius of 2 arcseconds and those in the same bin are shown with matching colors. The level of transparency corresponds to the total integrated flux from that fiber. A few fibers on the edges are discarded due to poor data quality (dark grey) or contamination from nearby objects (lighter gray). The S/N of each fiber versus radius is shown in the right panel, with bin divisions shown as vertical lines and the S/N threshold shown as a dotted horizontal line.

In many galaxies, some fibers at the outskirts of the field are discarded when the remaining outer fibers cannot achieve sufficient S/N. Typically, a small number of fibers for a given galaxy are contaminated by light from neighboring stars or galaxies, or other data problems: these are removed by hand. In the case of very bright or extended contaminants, an additional ring of fibers is removed around those that are contaminated: the data reduction process is described in detail in the appendix of Murphy et al. (2011).

1.2 Velocity distribution and angular momentum

In this section I briefly describe the method used by Veale et al. (2016) to extract the stellar line-of-sight velocity distribution (LOSVD) function, $f(v)$, from the absorption line features of each fiber spectrum. The determination of the first moments of the LOSVD allows to quantify velocity, dispersion and angular momentum profiles of each galaxy.

From the Mitchell spectrograph observations, Veale et al. (2016) extracted $f(v)$ for the 41 most massive ETGs ($M_K < -25.7$ mag, stellar mass $M_* > 10^{11.8}\,\mathrm{M}_\odot$) of the MASSIVE survey. With the penalized pixel-fitting (pPXF) method (Cappellari and Emsellem 2004), they convolve a set of spectra from template stars with $f(v)$ modeled as a Gauss-Hermite series up to order $n = 6$:

$$f(v) \propto \frac{e^{-\frac{(v-V)^2}{\sigma^2}}}{\sqrt{2\pi\sigma^2}}\left[1 + \sum_{m=3}^{n} h_m H_m\left(\frac{v-V}{\sigma}\right)\right], \tag{1}$$

where V is the mean velocity, σ is the velocity dispersion and $H_m(x)$ is the mth Hermite polynomial given by

$$H_m(x) = \frac{1}{\sqrt{m!}} e^{x^2}\left(-\frac{1}{\sqrt{2}}\frac{\partial}{\partial x}\right)^m e^{-x^2}. \tag{2}$$

The third moment h_3 is a measure of the skewness of the distribution (asimmetry of the absorption line, associated with rotation) and the fourth moment h_4 is a measure of the kurtosis (deviation of the absorption line from the Gaussian distribution, associated with anisotropy). Monte Carlo calculations are performed to determine the error bars on the best-fit velocity moments returned by pPXF.

Angular momentum is measured using the dimensionless parameter λ (Emsellem et al. 2007), calculated as a luminosity-weighted average over all spatial bins enclosed within radius R:

$$\lambda(< R) = \frac{\langle R|V|\rangle}{\langle R\sqrt{V^2+\sigma^2}\rangle}. \tag{3}$$

This parameter is used in a similar way as V/σ to quantify the dynamical importance of rotation relative to dispersion in a galaxy. The parameter λ_e is calculated

within the effective radius $R_{\rm e}$, which is the radius that encloses half of the total light. In addition to this, for each galaxy Veale et al. (2016) also find $\sigma_{\rm e}$ and $\sigma_{\rm e8}$, calculated as a luminosity-weighted average over all spatial bins enclosed within $R_{\rm e}$ and $R_{\rm e}/8$, respectively.

Veale et al. (2016) classify the ETGs of their sample as slow or fast rotators using a criterion that takes into account inclinations and applies specifically to measurements within an aperture of $R_{\rm e}$. Slow and fast rotators are, respectively, those with $\lambda_{\rm e} < 0.31\sqrt{\varepsilon}$ or $\lambda_{\rm e} > 0.31\sqrt{\varepsilon}$, where $\varepsilon = 1 - b/a$ is the observed ellipticity, and a and b are the major and minor semi-axis.

1.3 Velocity dispersion profiles

In this section I present the procedure used to quantify the shape of the outer velocity dispersion trends.

With the same method described in Paper V, Veale et al. (2018) obtained the best-fitting velocity V, dispersion σ and higher moments h_3, h_4, h_5 and h_6 for 90 MASSIVE galaxies. Starting from 2D observations, their purpose here is to characterise the velocity dispersion profile of each galaxy. Therefore, they calculate a local σ with a luminosity-weighted average over only the bins in the same annulus at a radius R. To quantify the overall shape of $\sigma(R)$, they fit the profile to a broken power-law:

$$\sigma(R) = \sigma_0 \left(\frac{2x}{1+x}\right)^{\gamma_1} \left(\frac{1+x}{2}\right)^{\gamma_2}, \tag{4}$$

where $x = R/R_{\rm b}$, the break radius $R_{\rm b}$ is fixed at 5 kpc and $\sigma_0 \equiv \sigma(R_{\rm b})$ is the profile normalization. Degeneracies between $R_{\rm b}$, γ_1 and γ_2 allow as good a fit for every galaxy with this fixed $R_{\rm b}$ as with a free $R_{\rm b}$. The logarithmic slope of the broken power-law is

$$\frac{d\ln\sigma(R)}{d\ln R} = \gamma_1 + \big(\gamma_2 - \gamma_1\big)\frac{x}{1+x}, \tag{5}$$

where γ_1 and γ_2 are the respective limits for $x \ll 1$ and $x \gg 1$. Of course, the observations only cover a limited range of R and that is why Veale et al. (2018) first consider $\gamma_{\rm inner}$ and $\gamma_{\rm outer}$, the local logarithmic slopes at 2 kpc ($x = 2/5$) and 20 kpc ($x = 4$), respectively defined as

$$\gamma_{\rm inner} = \left.\frac{d\ln\sigma(R)}{d\ln R}\right|_{R=2\,{\rm kpc}} = \frac{5}{7}\,\gamma_1 + \frac{2}{7}\,\gamma_2 \tag{6}$$

$$\gamma_{\rm outer} = \left.\frac{d\ln\sigma(R)}{d\ln R}\right|_{R=20\,{\rm kpc}} = \frac{1}{5}\,\gamma_1 + \frac{4}{5}\,\gamma_2. \tag{7}$$

From these it is easy to obtain γ_1 and γ_2 as

$$\gamma_1 = \frac{14}{9}\,\gamma_{\rm inner} - \frac{5}{9}\,\gamma_{\rm outer} \tag{8}$$

$$\gamma_2 = -\frac{7}{18}\,\gamma_{\rm inner} + \frac{25}{18}\,\gamma_{\rm outer}. \tag{9}$$

$\gamma_{\rm outer}$ is determined only for the 56 galaxies ($\sim 2/3$ of the sample) with data reaching at least 20 kpc. Most of them have a negative $\gamma_{\rm inner}$ (often in the range $-0.2 < \gamma_{\rm inner} < 0$), while $\gamma_{\rm outer}$ ranges from ~ -0.5 to $\sim +0.4$.

Veale et al. (2018) classify the ETGs of their sample in three categories depending on their velocity dispersion profiles in the outer regions. Falling, flat and rising profiles, shown in Figure 2, are those with $\gamma_{\rm outer} < 0$, $\gamma_{\rm outer} \sim 0$ within errors, and $\gamma_{\rm outer} > 0$, respectively.

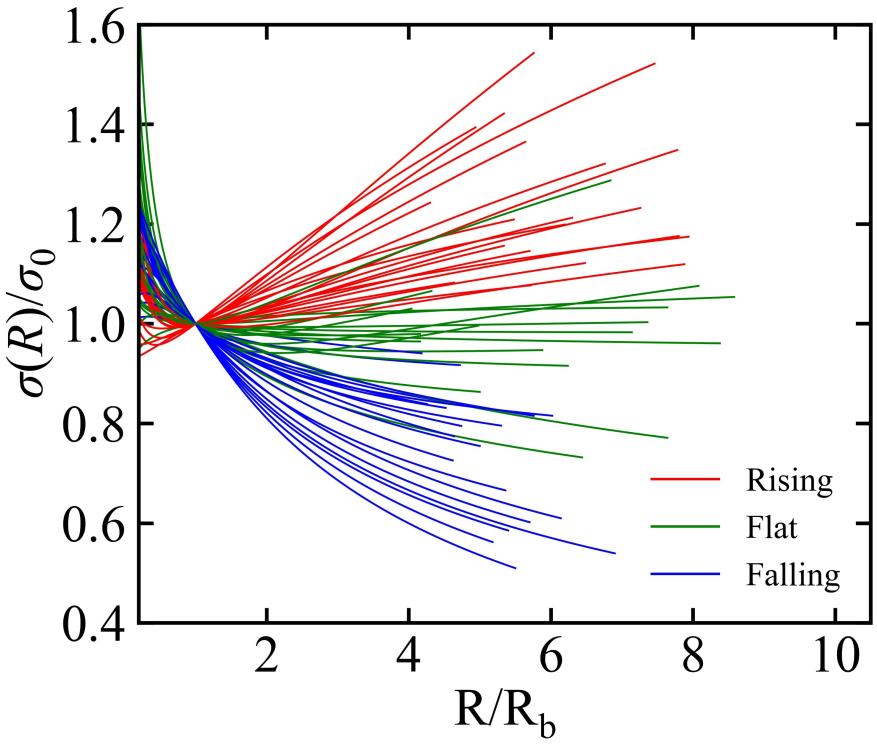

Figure 2: Double power-law fits $\sigma(R)$ for the 56 MASSIVE galaxies with binned data extended over 20 kpc. R is normalized to $R_{\rm b} = 5\,$kpc and $\sigma(R)$ is normalized to σ_0: this implies the intersection of all profiles at $R/R_{\rm b} = 1$. The rising profiles are shown in red, the flat in green and the falling in blue.

It is quite remarkable that this 56-galaxies sample is split nearly equally among the three types: 36% rising (20 galaxies), 30% flat (17 galaxies) and 34% falling (19 galaxies). This means that each of the three outer shapes is common among massive ETGs, and is well represented in the MASSIVE survey.

If a galaxy is in a group with at least three members in the HDC catalogue (Crook et al. 2007, 2008), Veale et al. (2017) assign it to be 'Satellite'; otherwise it is indicated as 'Isolated'. Classification as a brightest group galaxy (BGG) is based entirely on the K-band luminosity, and is not necessarily equivalent to being the central galaxy. Figure 3 shows outer slope $\gamma_{\rm outer}$ versus total absolute K-band

magnitude M_K for the 56 MASSIVE galaxies with binned data extended over 20 kpc. Satellite galaxies tend to have a slightly higher $\gamma_{\rm outer}$ and the most steeply rising profiles are found in satellite galaxies. Moreover, 10 out of the 11 most luminous galaxies ($M_K < -26$) have rising or nearly flat σ profiles. Figure 4 shows $\lambda_{\rm e}$ within $R_{\rm e}$ versus observed ellipticity ε: the three profile shapes are found at all ε and most ETGs in the sample have low (< 0.15) $\lambda_{\rm e}$.

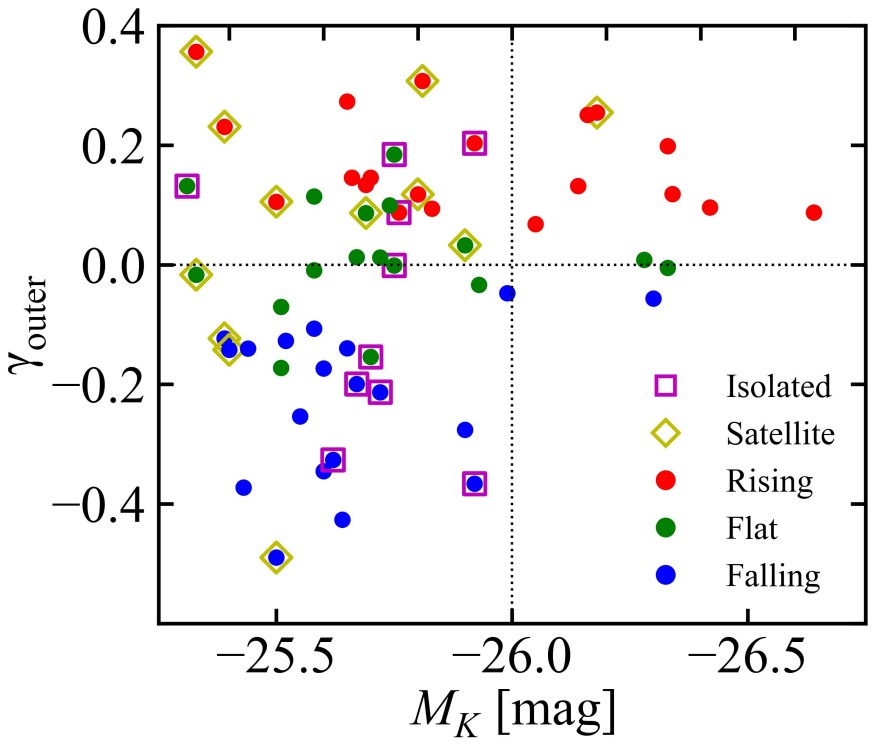

Figure 3: Outer slope $\gamma_{\rm outer}$ versus total absolute K-band magnitude M_K for the 56 MASSIVE galaxies with binned data extended over 20 kpc. Group membership is highlighted (yellow diamonds for satellite galaxies with more than three group members and magenta squares for isolated galaxies with fewer than three group members). Velocity dispersion trends are highlighted: rising (red), flat (green) and falling (blue). The black dotted lines correspond to $\gamma_{\rm outer} = 0$ and $M_K = -26$.

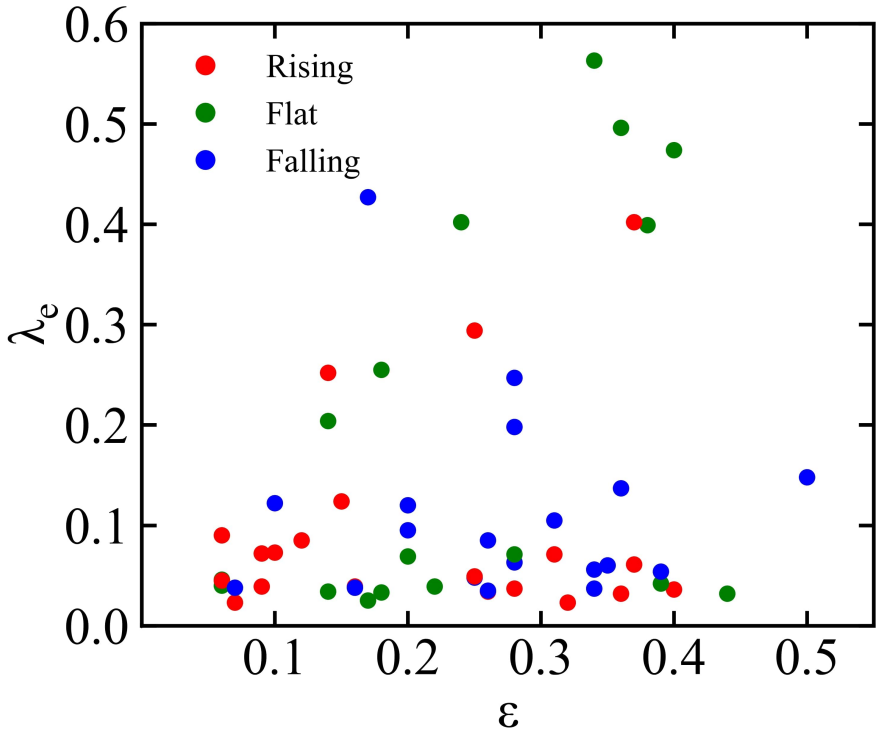

Figure 4: λ_e within R_e versus observed ellipticity ε for the 56 MASSIVE galaxies with binned data extended over 20 kpc. Velocity dispersion trends are highlighted: rising (red), flat (green) and falling (blue).

1.4 Representative sub-sample of MASSIVE ETGs

In this thesis I mainly focus on modeling the velocity dispersion profiles of six MASSIVE galaxies representative of the velocity dispersion trends (falling, flat and rising) described in Section 1.3.

I consider the 41 most massive early-type galaxies ($M_K < -25.7$ mag, stellar mass $M_* > 10^{11.8}\,\mathrm{M}_\odot$) of the MASSIVE survey, presented in Veale et al. (2016) and further studied in Veale et al. (2018), for which both V and σ observations are available. I aim to reproduce the velocity dispersion profiles within a confidence region bounded by $\sigma(R) \pm \Delta\sigma(R)$, where $\sigma(R)$ is that in Equation (4), and $\Delta\sigma(R)$ is estimated by error propagation on $\sigma(R)$ and is defined as

$$\Delta\sigma(R) = \sigma(R)\left[\left(\frac{\Delta\sigma_0}{\sigma_0}\right)^2 + \left(\ln\frac{2x}{1+x}\right)^2(\Delta\gamma_1)^2 + \left(\ln\frac{1+x}{2}\right)^2(\Delta\gamma_2)^2\right]^{1/2}. \quad (10)$$

In order to perform a comparison as close as possible with the observed $\sigma(R)$ (Veale et al. 2018), for models I consider $\sigma_{\rm los}^{\rm LA}(R)$, the luminosity-weighted average over annuli of given radius R of the line-of-sight velocity dispersion $\sigma_{\rm los}$ (Appendix B).

The adopted selection criteria require low errors on γ_1 and γ_2 to have a sufficiently narrow confidence region and thus a stronger constraint for the models. The outer regions of the galaxies are the most interesting to model (this is the advantage of the MASSIVE survey); thus I require data up to $2-3\,R_{\rm e}$ and extended over 20 kpc at least. Moreover, I would like to have three slow rotators and three fast rotators among the best ETGs chosen for the modeling, in order for the selected sub-sample to be representative of this major property, and check if results show significant differences among the two types. In the restricted 41-galaxies sample of Veale et al. (2016) there is no fast rotator ETG with a falling σ profile. NGC 4555 is a borderline galaxy with $\lambda_{\rm e} = 0.120 < 0.31\sqrt{\varepsilon} = 0.139$, but I consider it in this work since it is the galaxy with the highest $\lambda_{\rm e}$ in the sample among those with a falling σ profile.

Based on these criteria, this work will study six galaxies: NGC 0410 ($\lambda_{\rm e} = 0.048$, $\gamma_{\rm outer} = -0.276$), NGC 4555 ($\lambda_{\rm e} = 0.120$, $\gamma_{\rm outer} = -0.366$), NGC 2340 ($\lambda_{\rm e} = 0.032$, $\gamma_{\rm outer} = 0.033$), NGC 3158 ($\lambda_{\rm e} = 0.255$, $\gamma_{\rm outer} = 0.009$), NGC 4073 ($\lambda_{\rm e} = 0.023$, $\gamma_{\rm outer} = 0.199$) and NGC 0383 ($\lambda_{\rm e} = 0.252$, $\gamma_{\rm outer} = 0.307$). Other main properties are listed in Table 1, including: distance D, stellar mass M_*, effective radius $R_{\rm e}$, observed ellipticity ε, maximum radial extent of the binned data $R_{\rm max}$, velocity dispersion $\sigma_{\rm e}$ within $R_{\rm e}$ and group membership.

The fit parameters used to quantify the overall shape of their $\sigma(R)$ profile (σ_0, γ_1 and γ_2) are listed in Table 2 with their associated errors. $\gamma_{\rm inner}$ and $\gamma_{\rm outer}$ are also included. Their observed velocity dispersion σ and velocity V are shown in Figure 5 and 6. Red lines in Figure 5 indicate the double power-law fit $\sigma(R)$ for each galaxy. Point colour corresponds to the angular location of the bin: black and white points correspond to 0 and 180 degrees from the positive semi-major axis respectively, and grey points correspond to bins near the minor axis.

Since the observation resolution (radius of the fibers) is 2 arcseconds, I convert it in kpc as

$$R_{\rm min}[{\rm kpc}] = 9.7 \cdot 10^{-3}\, D[{\rm Mpc}], \tag{11}$$

where D is the distance of the galaxy. I study the velocity dispersion luminosity-weighted average $\sigma_{\rm los}^{\rm LA}$ and line-of-sight velocity $v_{\rm los}$ along the major axis from $R_{\rm min}$ to $\sim 2-3\,R_{\rm e}$, depending on the maximum radial extent of the observed σ and V profiles of each galaxy.

Table 1. Main global properties of the MASSIVE galaxies studied in this work

Galaxy	D (Mpc)	M_K (mag)	$\log_{10}M_*$ ($M_\odot$)	R_e (kpc)	ε	R_{max} (kpc)	λ_e	σ_e (km/s)	env
(1)	(2)	(3)	(4)	(5)	(6)	(7)	(8)	(9)	(10)
NGC 0410	71.3	-25.90	11.86	7.6	0.25	26.9	0.048	247	B
NGC 4555	103.6	-25.92	11.86	6.4**	0.20	34.6	0.120	277	I
NGC 2340	89.4	-25.90	11.86	14.3	0.44*	43.0	0.032	235	S
NGC 3158	103.4	-26.28	12.02	8.1*	0.18	36.9	0.255	289	B
NGC 4073	91.5	-26.33	12.05	10.2*	0.32	33.9	0.023	292	B
NGC 0383	71.3	-25.81	11.82	7.1*	0.14	26.8	0.252	257	S

Table 1: Columns are (1) Galaxy name. (2) Distance in Mpc. (3) Extinction-corrected 2MASS total absolute K-band magnitude. (4) Stellar mass estimated from M_K (see Section 2.1 of Veale et al. (2016)). (5) Observed effective radius from Ene et al. (2020) where available, from Davis et al. (2019) (indicated by *) or Gu et al. (2022) (indicated by **). (6) Observed ellipticity from NSA where available, from 2MASS otherwise (indicated by *). (7) Maximum radial extent of the binned data. (8) λ_e within R_e. (9) Velocity dispersion within R_e. (10) Group membership according to the 2MRS HDC catalogue: 'B' for BGGs (classification based entirely on the K-band luminosity), 'S' for satellites with more than three group members and 'I' for isolated galaxies with fewer than three group members.

Table 2. Parameters of $\sigma(R)$ of the MASSIVE galaxies studied in this work

Galaxy	σ_0 (km/s)	γ_1	γ_2	$\Delta\sigma_0$ (km/s)	$\Delta\gamma_1$	$\Delta\gamma_2$	γ_{inner}	γ_{outer}
(1)	(2)	(3)	(4)	(5)	(6)	(7)	(8)	(9)
NGC 0410	236.5	-0.035	-0.336	1.8	0.032	0.050	-0.121	-0.276
NGC 4555	273.0	0.053	-0.471	3.2	0.065	0.108	-0.097	-0.366
NGC 2340	233.5	-0.061	0.056	1.9	0.034	0.041	-0.028	0.033
NGC 3158	282.0	-0.058	0.025	2.2	0.031	0.039	-0.034	0.009
NGC 4073	283.0	-0.268	0.315	3.0	0.051	0.058	-0.101	0.199
NGC 0383	244.5	-0.392	0.482	3.5	0.074	0.090	-0.143	0.307

Table 2: Columns are (1) Galaxy name. (2) Profile normalization. (3) Logarithmic slope of $\sigma(R)$ at small radius. (4) Logarithmic slope of $\sigma(R)$ at large radius. (5) σ_0 error. (6) γ_1 error. (7) γ_2 error. (8) Logarithmic slope of $\sigma(R)$ at 2 kpc. (9) Logarithmic slope of $\sigma(R)$ at 20 kpc.

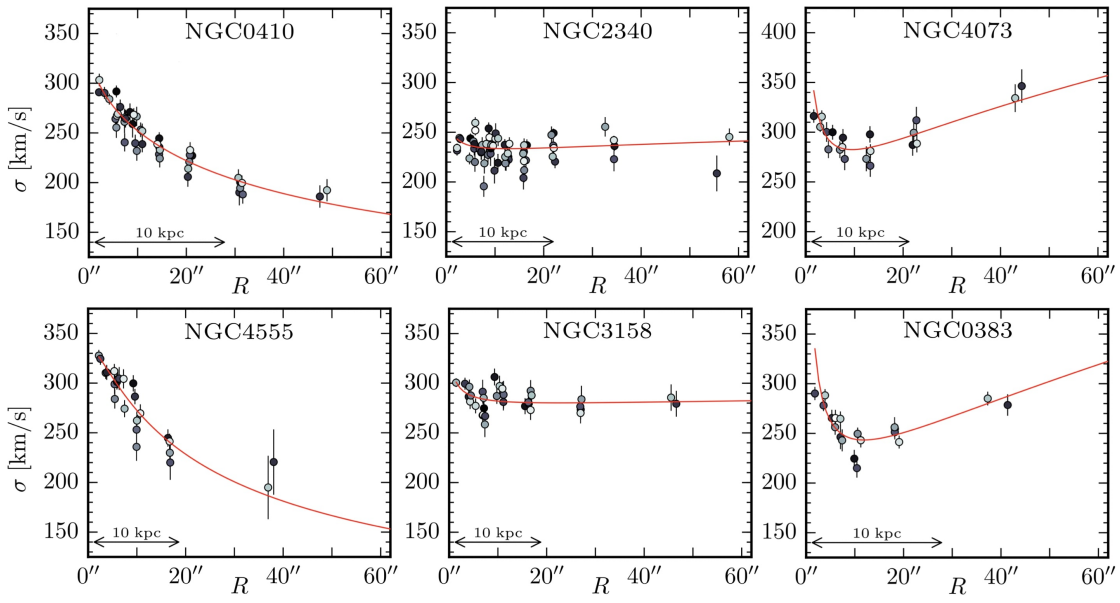

Figure 5: Observed velocity dispersion profiles (Veale et al. 2018) for NGC 0410, 2340, 4073, 4555, 3158, and 0383. Within each galaxy, σ is shown with error bars, with point colour corresponding to the angular location of the bin: black and white points correspond to positive and negative major semi-axis respectively, and grey points correspond to bins near the minor axis. The red line indicates the double power-law fits $\sigma(R)$, described in Equation 4.

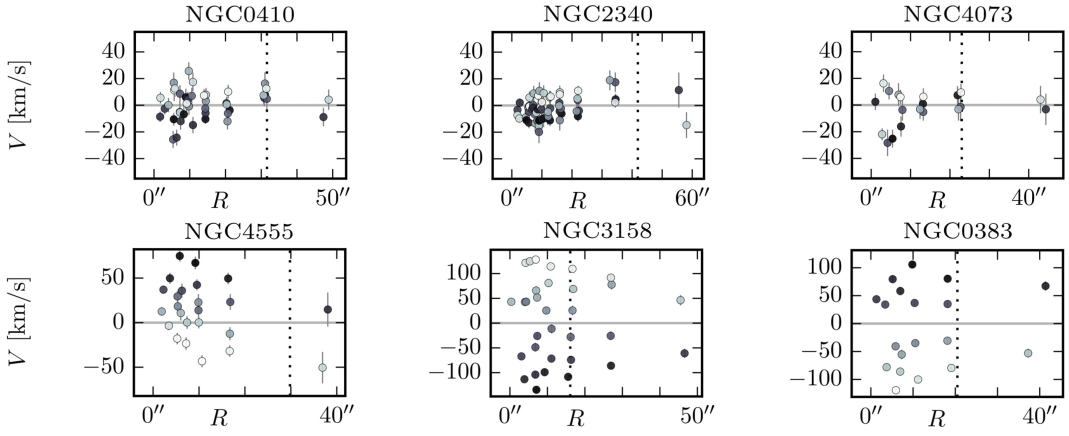

Figure 6: Observed velocity profiles (Veale et al. 2016) for NGC 0410, 2340, 4073, 4555, 3158, and 0383. Within each galaxy, V is shown with error bars, with point colour corresponding to the angular location of the bin: black and white points correspond to positive and negative major semi-axis respectively, and grey points correspond to bins near the minor axis.

2 The galaxy models

Models for the chosen galaxies are built using the numerical code JASMINE (Jeans AxiSymmetric Models of galaxies IN Equilibrium) (Posacki, Pellegrini, and Ciotti 2013). The code produces models of axisymmetric galaxies, based on the solution of the Jeans equations for a multicomponent gravitational potential (supermassive black hole, stars and dark matter halo). Considering the only non-zero streaming motion in the azimuthal direction ($\overline{v_R} = \overline{v_z} = 0$), the Jeans equations (Binney and Tremaine 1987) in cylindrical coordinates (R, φ, z) read:

$$\frac{\partial \rho_* \sigma_z^2}{\partial z} = -\rho_* \frac{\partial \Phi_{\rm tot}}{\partial z} \tag{12}$$

$$\frac{\partial \rho_* \sigma_R^2}{\partial R} - \rho_* \frac{\Delta}{R} = -\rho_* \frac{\partial \Phi_{\rm tot}}{\partial R}, \tag{13}$$

where $\Phi_{\rm tot} = \Phi_{\rm h} + \Phi_* + \Phi_{\rm BH}$ is the total gravitational potential and σ_R is the radial component of the velocity dispersion tensor, that is assumed to be diagonal and aligned with the coordinate system. $\Delta = \overline{v_\varphi^2} - \sigma_R^2 \equiv \overline{v_\varphi}^2 + \sigma_\varphi^2 - \sigma_R^2$ determines how much the azimuthal motions prevail on the radial motions: $\overline{v_\varphi}$ is the average azimuthal velocity and σ_φ is the azimuthal velocity dispersion.

Potential and Jeans solvers are both developed in `Fortran 90`, and they run in parallel using three processors. The Potential solver is needed to evaluate the gravitational potentials that cannot be expressed analytically and requires a computational time of less than two hours. The Jeans solver receives as input the gravitational potentials, solves the Jeans equations, and projects the kinematic fields obtaining $\sigma_{\rm los}$ and $v_{\rm los}$ (see Appendix B). The two solvers can run separately: this allows to do different modelings (varying the orbital configuration) using only the Jeans solver, which requires a much lower computational time. Moreover, if the analytical potential of the halo component is available, I can also change the dark matter distribution without having to use the Potential solver.

The output data of both Potential and Jeans solvers are stored in HDF5 files (in binary format), and then read as input in the `Python 3` code that I developed for the post-processing of the model results. With this additional code I determine the confidence region $\sigma(R) \pm \Delta\sigma(R)$ (Section 1.4) and compute the luminosity-weighted average $\sigma_{\rm los}^{\rm LA}(R)$ for each radius R (Appendix B). For the purpose of this work, I partially upgraded the JASMINE code with:

- The addition of a Jaffe density profile for stars (Section 2.1);
- The possibility of having radial or tangential anisotropy (Section 2.3);
- A spatially varying rotational support (Section 2.4);
- A fixed logarithmic grid for all models (Appendix A).

In this chapter I illustrate the mass components and orbital configuration that are given as input to the Jeans equations. The accurate choice of the model parameters is of paramount importance here to properly investigate the role of anisotropy and total mass distribution in determining the galaxy kinematics.

2.1 Stellar component

For the stellar density I consider an axisymmetric distribution described by a Jaffe profile (Jaffe 1983) as

$$\rho_{\rm J}(R,z) = \frac{r_{\rm JAF}\, M_*}{4\pi\, q\, r_q^2 (r_{\rm JAF}+r_q)^2}, \tag{14}$$

where $r_q = \sqrt{R^2+z^2/q^2}$, $r_{\rm JAF} \sim 4R_{\rm e0}/3$ is the Jaffe scale radius and M_* is the total stellar mass. The effective radius for a face-on (FO) view is $R_{\rm e0} = R_{\rm e}/\sqrt{q}$, where $R_{\rm e}$ is the circularized effective radius for an edge-on (EO) view and q is the intrinsic flattening parameter ($q \leq 1$): the minor axis is aligned with the z axis.

The gravitational potential associated with the stellar component (Φ_*) is computed numerically by the JASMINE code, since it cannot be expressed analytically in the axisymmetric case. For a spherical mass distribution, the gravitational potential Φ is related to the density ρ through the following Poisson equation:

$$\frac{1}{r^2}\frac{d}{dr}\left(r^2\frac{d\Phi}{dr}\right) = 4\pi G\rho, \tag{15}$$

where $G = 6.67\cdot 10^{-8}\,{\rm g}^{-1}\,{\rm cm}^3\,{\rm s}^{-2}$ is the universal gravitational constant.
Therefore, for a spherical Jaffe profile ($q = 1$) I would have:

$$\rho(r) = \frac{r_{\rm JAF}\, M_*}{4\pi\, r^2 (r_{\rm JAF}+r)^2} \tag{16}$$

$$\Phi = -\frac{GM_*}{r_{\rm JAF}}\ln(1+r_{\rm JAF}/r). \tag{17}$$

2.1.1 Flattening parameter

In the general case, the observed ellipticity ε is related to q as (Lanzoni and Ciotti 2003):

$$(1-\varepsilon)^2 = \cos^2 i + q^2 \sin^2 i, \tag{18}$$

from which I have

$$q = \frac{\sqrt{\sin^2 i - \varepsilon(2-\varepsilon)}}{\sin i}, \tag{19}$$

where i is the l.o.s. inclination angle. $i = 0$ and $i = \pi/2$ indicate FO and EO views, respectively. A limitation of the models is that currently JASMINE computes the

projection of the intrinsic kinematic quantities only for FO and EO views. On the other hand, the inclination angles of the MASSIVE ETGs are not available in the literature. Therefore, I assume that the examined galaxies are observed edge-on ($i = \pi/2$). With this assumption in mind, I directly have that $q = 1 - \varepsilon$ from the ε values in Table 1. Using also the observed effective radius $R_{\rm e}$ from Table 1, I derive $R_{\rm e0}$.

2.1.2 Stellar mass

Equation (14) shows that $\rho_{\rm J}(R, z)$ is directly proportional to M_*, which I do not adopt as a fixed parameter in the models. As described in Veale et al. (2018), M_* in Table 1 is estimated from the absolute K-band magnitude M_K:

$$\log_{10} M_* \sim 10.58 - 0.44\,(M_K + 23). \tag{20}$$

This relation is based on the ATLAS$^{\rm 3D}$ dynamical masses $M_{\rm JAM}$, assuming that $M_* = M_{\rm JAM}$ as discussed in Section 4.3 of Cappellari et al. (2013). Equation (20) is uncalibrated at high masses, while $M_K < -25.8$ for the galaxies of this study. I found that a $\log_{10} M_*$ value within a range of ~ 0.36, which corresponds to 2.6σ from the best-fitting relation (Figure 7), always provides a good $\sigma(R)$ profile in the central galactic region (see Section 3). Note that M_* is independent of the choice of $R_{\rm e}$ and q.

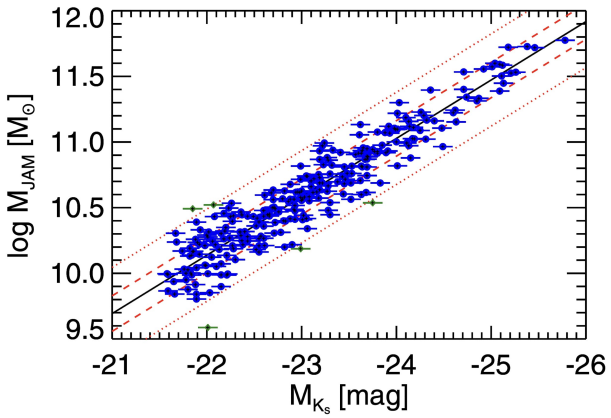

Figure 7: Best-fitting relation (solid line) between the dynamical mass $M_{\rm JAM} \approx M_*$ and the absolute K-band magnitude M_K, from Cappellari (2013). Dashed and dotted lines indicate the 1σ and 2.6σ bands, respectively.

I assume a supermassive black hole with mass $M_{\rm BH} = 2 \cdot 10^{-3}\, M_*$, as found in McConnell and Ma (2013). The black hole presence produces the gravitational potential

$$\Phi_{\rm BH} = -\frac{G M_{\rm BH}}{r}, \tag{21}$$

where $r = \sqrt{R^2 + z^2}$.

2.2 Halo component

For the dark matter density I consider a spherical distribution described by a Navarro-Frenk-White (NFW) profile (Navarro, Frenk, and White 1997) as

$$\rho_{\rm NFW}(r) = \frac{M_{\rm h}}{4\pi\, r\, (r_{\rm h}+r)^2\, f(c)}, \tag{22}$$

where $r = \sqrt{R^2+z^2}$ and $r_{\rm h} = \beta\, R_{\rm e}$ is the NFW scale radius. The gravitational potential associated with the halo component is therefore

$$\Phi_{\rm h} = -\frac{GM_{\rm h}}{r}\,\frac{\ln(1+r/r_{\rm h})}{f(c)}, \tag{23}$$

where $M_{\rm h}$ is the dark matter mass enclosed within the truncation radius $r_{\rm t} = c\, r_{\rm h}$, c is the concentration parameter and $f(c) = \ln(1+c) - c/(1+c)$.

I consider $\beta \geq 3$ in the modeling since dark matter prevails in the outer regions compared to the stellar component (Thomas et al. 2005; Cappellari et al. 2013). I take $c = 10$, a plausible value for the dark matter halo of galaxies as massive as those in the present investigation (Dutton and Macciò 2014). $f(c)$ is only slightly dependent on c: for $c = 10$, $f(c) = 1.49$. For $c = 8$ and $c = 12$ I would have $f(c) = 1.31$ and $f(c) = 1.64$, respectively. With the main goal of reproducing the velocity dispersion profiles within the confidence region (especially outside $R_{\rm e}$), $M_{\rm h}$ and β are the free parameters.

For a given $R_{\rm e}$, the extent of dark matter distribution ($r_{\rm t}$) is directly determined by β and c as $r_{\rm t} = c\,\beta\, R_{\rm e}$, and this leads to a careful choice of the physical extent of the numerical grid. In principle, I would like to have a grid extended enough to include $r_{\rm t}$ of all models, thus also the ones with a high β. In the matter of fact, I verified that the presence of dark matter beyond 500 kpc has barely no effect on the $\sigma_{\rm los}^{\rm LA}$ profile within $\sim 5\, R_{\rm e}$. For this reason, I use a numerical grid extended up to 500 kpc for all models (see Appendix A).

2.3 Anisotropy parameter

Once the associated gravitational potentials for the three mass components (supermassive black hole, stars and dark matter halo) are computed, the JASMINE code derives the kinematical structure of the galaxy.

I consider the anisotropy parameter $b \equiv \sigma_R^2/\sigma_z^2$ (Cappellari 2008) as a free parameter in the modeling, but constant throughout the galaxy. In a realistic case instead, $b \sim 1$ in the inner regions, and it should increase with R. This comes from galaxy formation mechanisms that determine a greater anisotropy in the outer regions of the galaxy (positive h_4 gradients found in Veale et al. (2018)). $b = 1$ corresponds to the isotropic case, $b > 1$ determines radial anisotropy, and $b < 1$ indicates tangential anisotropy.

Regular rotators are found to span a range of b at given intrinsic ellipticity $\varepsilon_{\rm intr} = 1 - q$, with the range increasing with $\varepsilon_{\rm intr}$: more flattened galaxies (lower q) are consistent with a wider range of b (Cappellari 2016). Regular rotators are found to have b below the following linear relation, which I assume as an upper limit in the modeling, for both fast and slow rotators (Cappellari et al. 2007):

$$b \sim \frac{1}{1 - 0.7\,\varepsilon_{\rm intr}}. \tag{24}$$

The solution to the Jeans equations (12 and 13) reads

$$\sigma_z^2 = \frac{1}{\rho_*} \int_z^\infty \rho_* \, \frac{\partial \Phi_{\rm tot}}{\partial z} \, dz \tag{25}$$

$$\Delta = b \, \frac{R}{\rho_*} \frac{\partial \rho_* \sigma_z^2}{\partial R} + R \, \frac{\partial \Phi_{\rm tot}}{\partial R}, \tag{26}$$

where σ_z^2 and Δ depend only on $\Phi_{\rm tot}$, ρ_* and b. The case of a negative Δ is not frequently encountered in applications but it is not impossible; for example, it can occur in density distributions with multiple stellar components or elongated along the symmetry axis (Caravita, Ciotti, and Pellegrini 2021). The case of $\Delta \geq 0$ is more common in models with a single stellar distribution and guarantees that $\overline{v_\varphi^2} = \Delta + \sigma_R^2$ is positive. For our models I find that Δ is always > 0.

2.4 Description of the rotation velocity

To obtain the ordered and random components of the azimuthal velocity field ($\overline{v_\varphi}$ and σ_φ), I use Satoh's k-decomposition (Satoh 1980).

If $\Delta \geq 0$, this decomposition assumes that

$$\overline{v_\varphi}^2 = k^2 \, \Delta, \tag{27}$$

and then

$$\sigma_\varphi^2 \equiv \overline{v_\varphi^2} - \overline{v_\varphi}^2 = \sigma_R^2 + (1 - k^2)\Delta. \tag{28}$$

The Satoh's parameter $k \leq 1$ determines the amount of rotational support.
If $b = 1$, $k = 1$ corresponds to the isotropic rotator ($\sigma_\varphi = \sigma_R$) and $k = 0$ means the absence of rotation ($\overline{v_\varphi} = 0$), so that all the flattening is due to the azimuthal velocity dispersion σ_φ.

With the aim of better reproducing the V profiles of the chosen galaxies, I consider a spatially varying rotational support (Negri, Ciotti, and Pellegrini 2014):

$$k(r) = k_0 + (k_\infty - k_0) \frac{r}{\xi_0 + r}, \tag{29}$$

where $r = \sqrt{R^2 + z^2}$. $k_0 \leq 1$ is the central value of $k(r)$, $k_\infty \leq 1$ is the value of

$k(r)$ for $r \gg \xi_0$ and ξ_0 is the profile scale radius, at which $k(r) = (k_0 + k_\infty)/2$. I verified that considering $k_\infty = 0$ (no rotation at $r \gg \xi_0$) and varying only the other two parameters (k_0 and ξ_0) allows to model reasonably well the observed velocity (Figure 6). Therefore, I consider $k(r) = k_0[1 - r/(\xi_0 + r)]$ in the modeling.

It is interesting to better understand how b and k influence the galaxy kinematics. For ease of notation, I define α as the logarithmic slope of $\rho_* \sigma_z^2$, which depends only on $\Phi_{\rm tot}$ and ρ_*:

$$\alpha = \frac{R}{\rho_* \sigma_z^2} \frac{\partial \rho_* \sigma_z^2}{\partial R}. \tag{30}$$

The circular velocity v_c^2 is defined as

$$v_c^2 = R \frac{\partial \Phi_{\rm tot}}{\partial R}, \tag{31}$$

so that, using Equation (26), I have:

$$\Delta = b\,\alpha\,\sigma_z^2 + v_c^2 \tag{32}$$

$$\overline{v_\varphi}^2 = k^2\,(b\,\alpha\,\sigma_z^2 + v_c^2) \tag{33}$$

$$\sigma_\varphi^2 = b\,[1 + \alpha\,(1 - k^2)]\,\sigma_z^2 + (1 - k^2) v_c^2 \tag{34}$$

$$\overline{v_\varphi^2} = b\,(1 + \alpha)\,\sigma_z^2 + v_c^2. \tag{35}$$

As b increases, $\overline{v_\varphi}^2$ decreases if $\alpha < 0$ (Equation 33) and σ_φ^2 decreases if $k^2 < 1 + 1/\alpha$ (Equation 34). Note that α is generally in the same range of values of the logarithmic slope of ρ_*, that in the case of a Jaffe profile is between -2 and -4. If in some regions of space there are high values of k (above ~ 0.7), then σ_φ^2 increases as b increases (e.g. in the inner regions of fast rotators). Radial anisotropy (higher b) determines a higher σ_R^2 throughout the galaxy and a lower σ_φ^2 in the outer regions compared to the isotropic case: $\sigma_{\rm los}$ is therefore higher at the centre and lower in the outer regions.

3 Results of the modeling

In this chapter I investigate the dynamical structure and dark matter distribution of the six early-type galaxies chosen in Section 1.4. I model them considering $R_{\rm e}$ from Table 1, $q = 1 - \varepsilon$, and $c = 10$ as fixed parameters. With the aim of having $\sigma_{\rm los}^{\rm LA}(R)$ within the confidence region given by observations (Equation 10) and $v_{\rm los}(R, z = 0)$ in agreement with the observed V along the major axis (Veale et al. 2016), I vary M_*, β, $M_{\rm h}$, k_0, ξ_0 and b as free parameters. Here I briefly illustrate the modeling procedure that I have followed for each galaxy.

I make preliminary models with $b = 1$, a constant $k(r)$ (0.1 for slow rotators and 0.5 for fast rotators) and no dark matter to identify the value of M_* (within 2.6σ from Equation 20) that is more appropriate to reproduce $\sigma(R)$ in the inner regions. With the M_* found, and using the previous values of b and $k(r)$, I add a dark matter halo varying β and $M_{\rm h}$, to reproduce $\sigma(R)$ in the outer regions. With these β and $M_{\rm h}$, I consider a spatially varying $k(r)$ given in Equation (29): I determine the appropriate k_0 and ξ_0 to reproduce the observed V along the major axis. Note that k_0 and ξ_0 have slight effects on $\sigma_{\rm los}^{\rm LA}(R)$. With the previous values of M_*, β and $M_{\rm h}$, I add radial or tangential anisotropy ($b \neq 1$). Since b significantly influences $v_{\rm los}$, the presence of orbital anisotropy requests different values of k_0 and/or ξ_0 to reproduce the observed V. Generally, the values of β and $M_{\rm h}$ found in the isotropic case result to be also appropriate to reproduce the outer $\sigma(R)$ when $b \neq 1$.

With the procedure just described it is easy to achieve convergence in the values of the free parameters, finding β, $M_{\rm h}$ and b that allow to have $\sigma_{\rm los}^{\rm LA}(R)$ within the confidence region and $v_{\rm los}(R, z = 0)$ in agreement with the observed V. Besides this, I also aim to have plausible values of the dark matter fraction $f_{\rm DM} = M_{\rm h}(r)/M_{\rm tot}(r)$ within $1\,R_{\rm e}$ and $5\,R_{\rm e}$, where $f_{\rm DM}$ is defined as the ratio of the dark matter mass to the total mass contained within a given radius r. The $f_{\rm DM}$ values within $1\,R_{\rm e}$ found for well studied ETGs from stellar dynamics and gravitational lensing studies are $\sim 0.1 - 0.5$ (Gerhard et al. 2001; Treu and Koopmans 2004; Santucci et al. 2022). $f_{\rm DM}$ within $5\,R_{\rm e}$ is generally $\sim 0.6 - 0.9$ for galaxies as massive as those in the present investigation (Alabi et al. 2017).

3.1 Falling profiles

In this section I present the modeling of NGC 0410 and NGC 4555, the two galaxies with a falling σ profile chosen for this work. Here the aim is to check how the dark matter distribution can influence the velocity dispersion profiles in the outer regions and, therefore, to put eventual constraints on β and $M_{\rm h}$.

3.1.1 NGC 0410

NGC 0410 has a falling $\sigma(R)$ profile in the outer regions ($\gamma_{\rm outer} = -0.276$) and $\lambda_{\rm e} = 0.048$. From Table 1, its $R_{\rm e} = 7.6\,{\rm kpc}$. I consider $q = 1 - \varepsilon = 0.75$ and $b < 1.21$, from Equation (24). In the preliminary modeling I find $10^{11.79}\,{\rm M}_\odot$ (lower than the value in Table 1 but within 0.5σ from Cappellari (2013) relation) to be an appropriate value to reproduce the central velocity dispersion profile. I start examining the isotropic case ($b = 1$); for this case $k_0 = 0.1$ and $\xi_0 = 2\,R_{\rm e}$ reproduce well the observed V profile along the major axis. With a Jaffe profile for the stellar density, the model with no dark matter almost reproduces the observed falling $\sigma(R)$ (black curve in Figure 8).

I add a dark matter halo starting with $\beta = 3$ since dark matter prevails in outer regions compared to the stellar component (Thomas et al. 2005; Cappellari et al. 2013). Having β fixed, I vary the dark matter mass $M_{\rm h}$ accordingly: $M_{\rm h}/M_* = 2$ is found to produce $\sigma^{\rm LA}_{\rm los}$ within the confidence region, though $\sigma(R)$ has a steeper profile in the outer parts (red curve in Figure 8). $f_{\rm DM}$ within $R_{\rm e}$ is ~ 0.11 in this case, but I would expect larger values for $M_{\rm h}/M_*$. For instance, galaxies with stellar mass $M_* > 10^{11}\,{\rm M}_\odot$ generally have $M_{\rm h}/M_* > 50$ (Moster et al. 2010).

Since increasing $M_{\rm h}$ only would make $\sigma^{\rm LA}_{\rm los}(R)$ larger, especially outside $R_{\rm e}$, I thus increase β to 6 and obtain a good model for $M_{\rm h}/M_* = 5$ (green curve in Figure 8). The red and green curves in Figure 8 are very close, showing how in this modeling an increase of β and $M_{\rm h}$ can leave $\sigma^{\rm LA}_{\rm los}$ unchanged, at least within a few $R_{\rm e}$. Taking a step back, this can be better understood by seeing how the NFW profile is defined in Equation (22). $\rho_{\rm NFW}$ directly determines $\Phi_{\rm h}$ which has an important influence on the kinematics. Therefore, I expect that models with a similar dark matter density profile present a similar kinematics, even if their β and $M_{\rm h}$ are different. For instance, maintaining the same $\rho_{\rm NFW}(r = 2\,R_{\rm e})$ as β, $M_{\rm h}$ or c vary would require the conservation of the following quantity:

$$M_{\rm h}\,(\beta + 2)^{-2}\,f(c)^{-1} \sim {\rm cost.} \tag{36}$$

Therefore, increasing β leads to a significant reduction of the dark matter density in the inner regions, and this effect can be compensated by increasing $M_{\rm h}/M_*$. The higher β and $M_{\rm h}$ (flatter density profile in Figure 9) leads to a $\sigma^{\rm LA}_{\rm los}$ profile that is steeper in the inner regions and flatter in the outer ones. Isotropic models with $\beta = 3$ and a low quantity of dark matter already reproduce $\sigma(R)$ observations up to $2\,R_{\rm e}$.

I check next how radial anisotropy can influence $\sigma_{\rm los}^{\rm LA}(R)$, in particular making it steeper as would be required. With the constraint of $b < 1.21$, I increase the anisotropy parameter b to 1.2, starting with $\beta = 3$ and $M_{\rm h}/M_* = 2$ as found in the isotropic case (green curve in the upper panel in Figure 10). The difference is subtle but, as expected, the presence of radial anisotropy leads to a $\sigma_{\rm los}^{\rm LA}$ profile that is overall steeper, and also within the confidence region up to $2.5\,R_{\rm e}$. For the models with $b = 1.2$, $k_0 = 0.2$ and $\xi_0 = 1.5\,R_{\rm e}$ reproduce the observed V along the major axis, which has typical values in the range of $\sim 5 - 15$ km/s (lower panel in Figure 10). As expected from the considerations in Section 2.4, $v_{\rm los}$ decreases at the increase of b (since $\alpha < 0$), and this effect can be compensated by decreasing ξ_0 and/or increasing k_0, as done here for $b = 1.2$. ξ_0 also allows to model the steepness of $k(r)$ and therefore of the $v_{\rm los}$ profile.

Veale et al. (2018) suggested that radial anisotropy can be requested to reproduce falling $\sigma(R)$ profiles, but in this case the isotropic model ($b = 1$) already determines a good fit with the observations. A low quantity of dark matter suffices ($M_{\rm h}/M_* = 2$) and the constraints on β are weak: low values of β ($\sim 3 - 6$) determine a good agreement between models and the observed $\sigma(R)$.

Figures 11 and 12 show the 2D maps of the velocity dispersion and velocity fields, respectively, for the model with $b = 1, \beta = 3, M_{\rm h}/M_* = 2$. As a comparison, Figure 13 shows the 2D map of $\sigma_{\rm los}$ in the presence of radial anisotropy ($b = 1.2$). The white contours (indicating regions of equal $\sigma_{\rm los}$) are more flattened along the minor axis in the isotropic case.

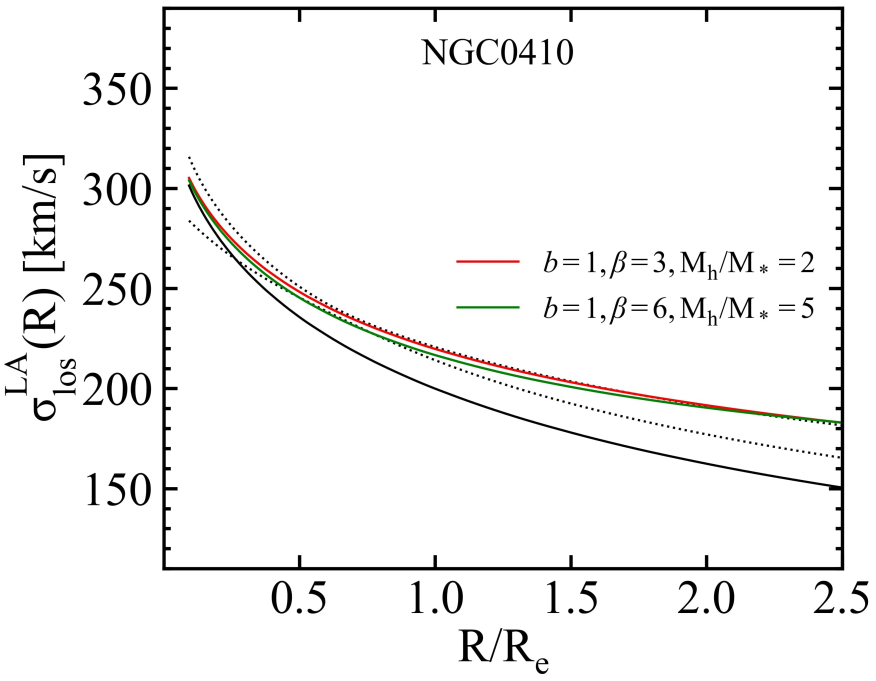

Figure 8: Velocity dispersion luminosity-weighted average $\sigma^{\rm LA}_{\rm los}(R)$ for NGC 0410. The models considered are: no dark matter (black), $\beta = 3, M_{\rm h}/M_* = 2$ (red) and $\beta = 6, M_{\rm h}/M_* = 5$ (green). $b = 1$, $k_0 = 0.1$ and $\xi_0 = 2\,R_{\rm e}$ in all three models. The dotted black curves define the confidence region given by $\sigma(R) \pm \Delta\sigma(R)$.

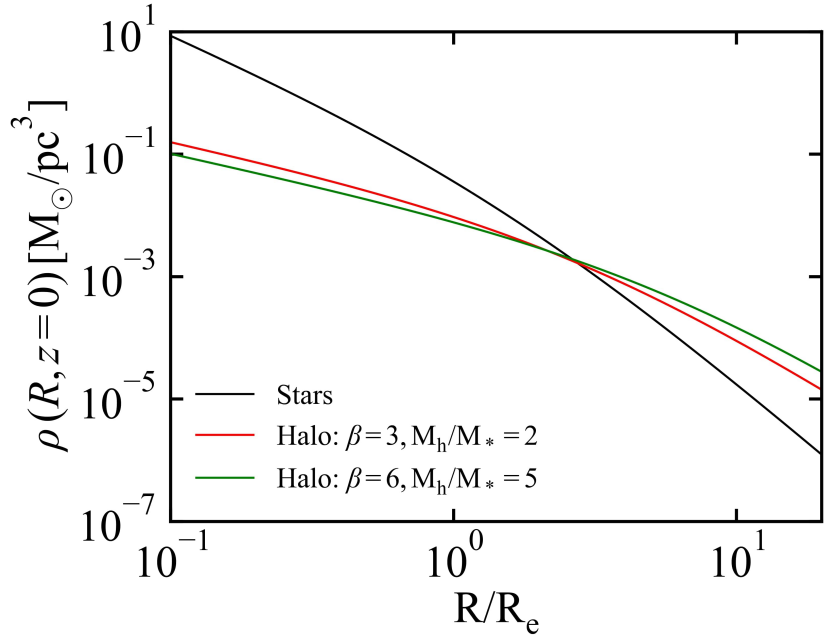

Figure 9: Density profiles for the models in Figure 8: stellar component along the major axis with $M_* = 10^{11.79}\,{\rm M}_\odot$ (black), halo component with $\beta = 3, M_{\rm h}/M_* = 2$ (red) and $\beta = 6, M_{\rm h}/M_* = 5$ (green).

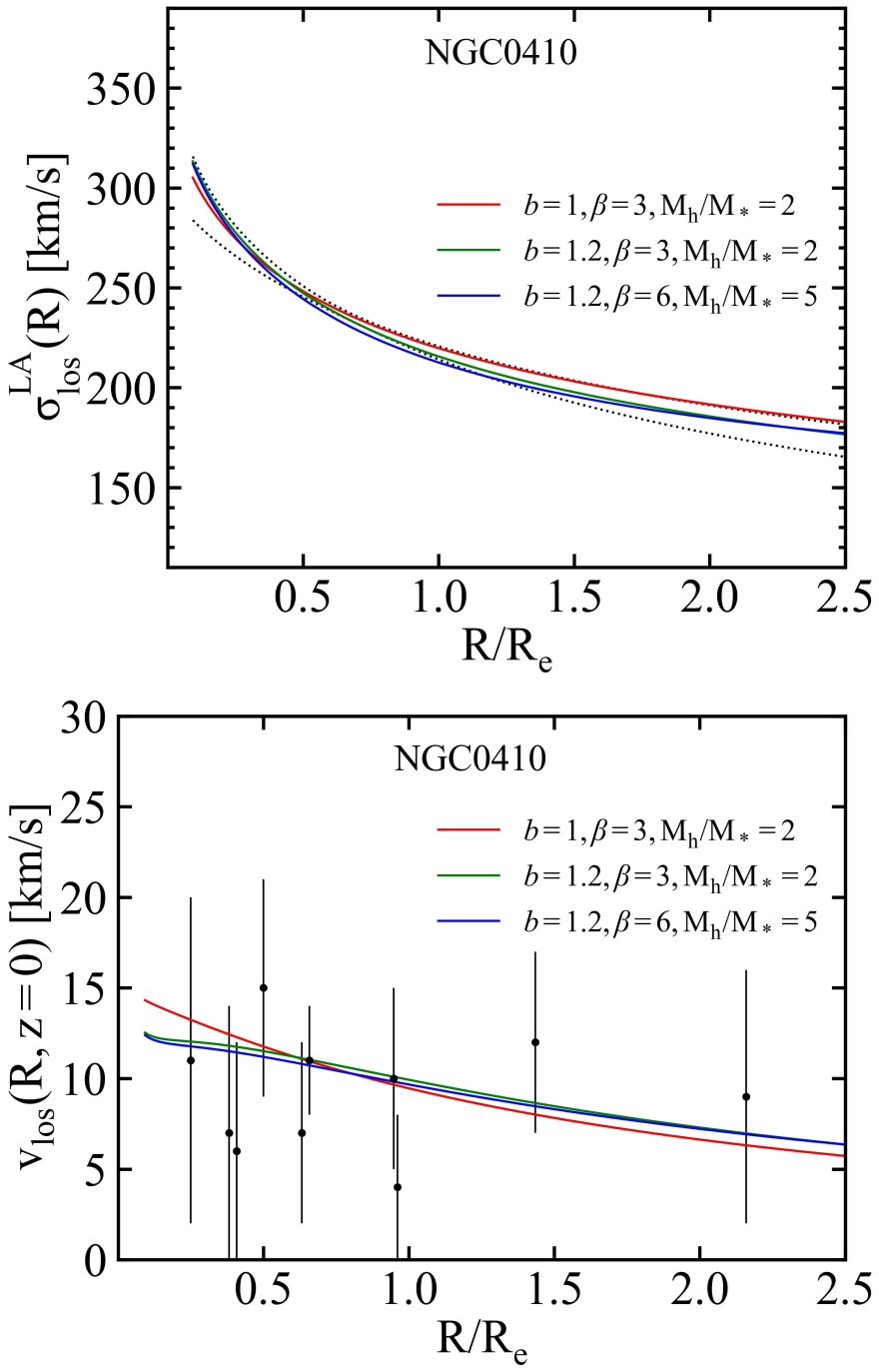

Figure 10: Velocity dispersion luminosity-weighted average $\sigma^{\rm LA}_{\rm los}(R)$ (upper panel) and line-of-sight velocity $v_{\rm los}$ along the major axis (lower panel) for NGC 0410. $k_0 = 0.1$ and $\xi_0 = 2\,R_{\rm e}$ for the model with $b = 1$ (red curve). $k_0 = 0.2$ and $\xi_0 = 1.5\,R_{\rm e}$ for the models with $b = 1.2$ (green and blue curves). In the upper panel, the dotted black curves define the confidence region given by $\sigma(R) \pm \Delta\sigma(R)$. In the lower panel, the black points with error bars correspond to the observed V along the major axis from Veale et al. (2016).

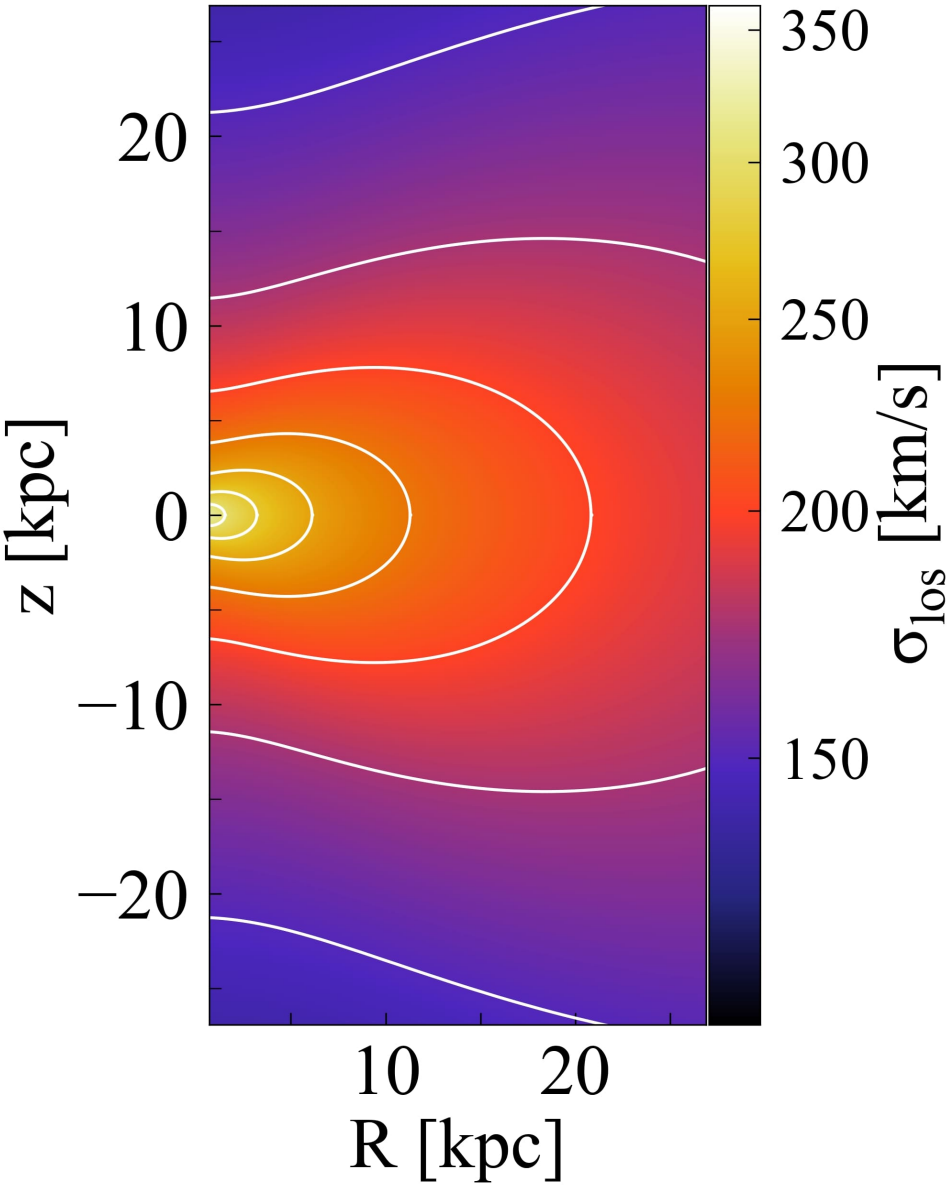

Figure 11: 2D map of the stellar velocity dispersion field $\sigma_{\rm los}$ for NGC 0410. The model considered is $M_* = 10^{11.79}\,{\rm M}_\odot, b = 1, \beta = 3, M_{\rm h}/M_* = 2$. White contours correspond to 150, 175, 200, 225, 250, 275 and 300 km/s.

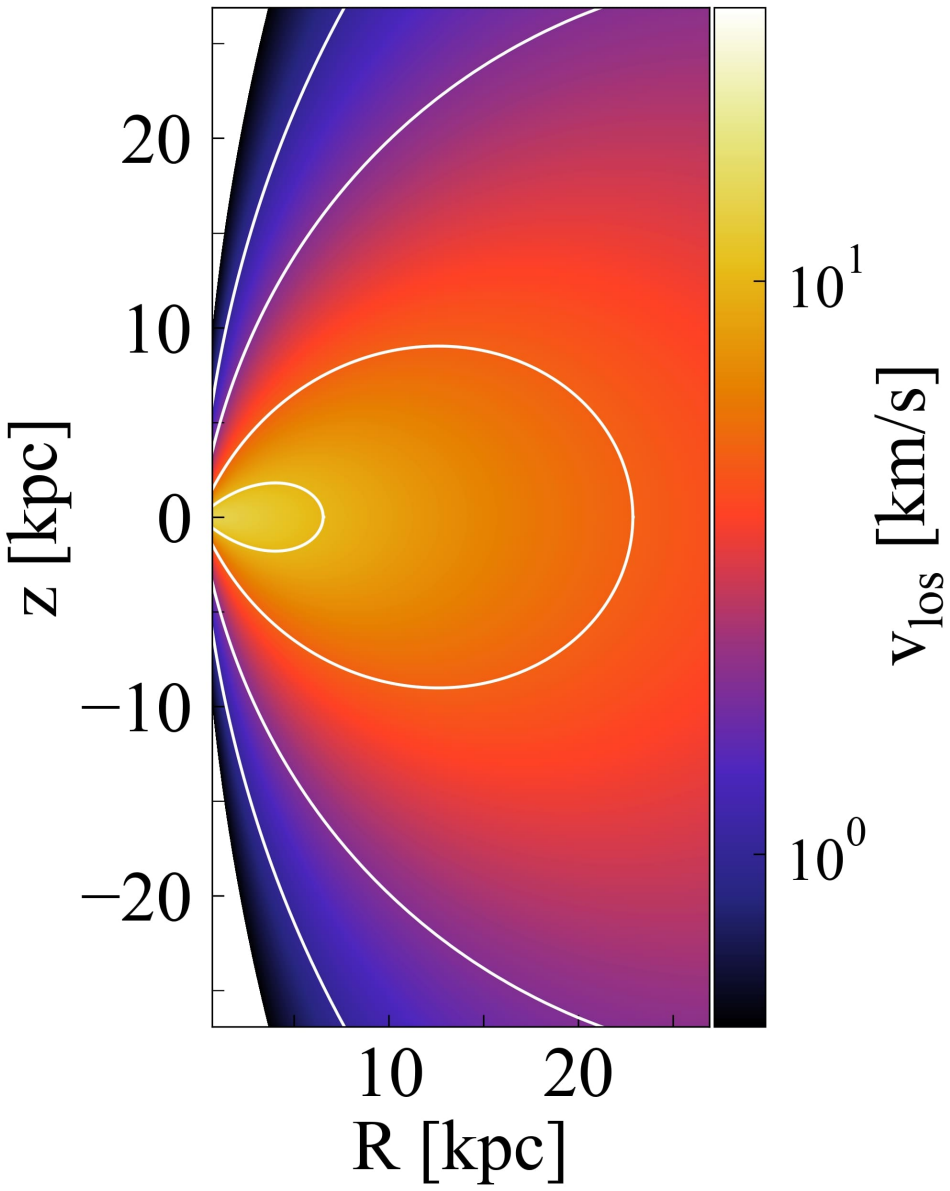

Figure 12: 2D map of the stellar velocity field $v_{\rm los}$ for NGC 0410. The model considered is $M_* = 10^{11.79}\,{\rm M}_\odot, b = 1, \beta = 3, M_{\rm h}/M_* = 2$. White contours correspond to 1, 2, 5 and 10 km/s.

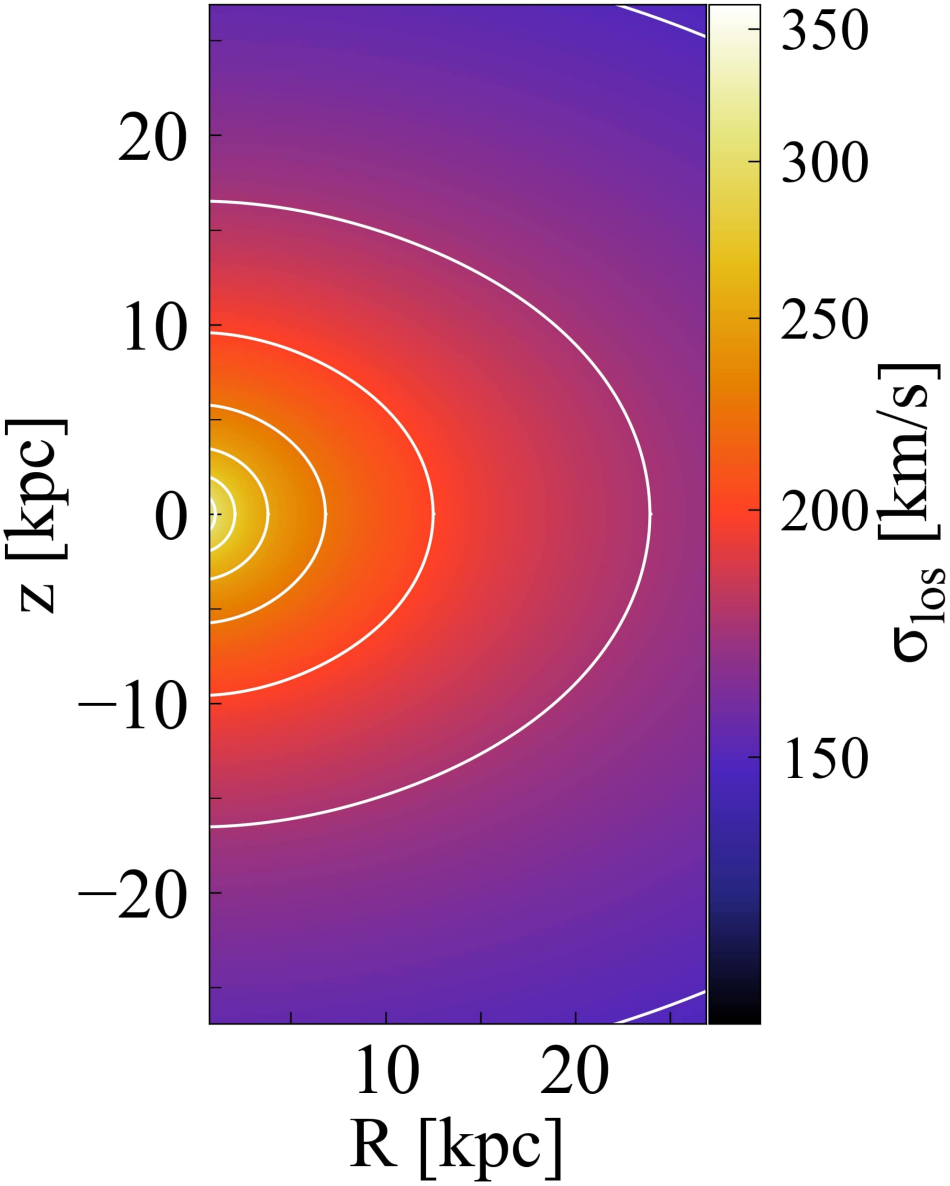

Figure 13: 2D map of the stellar velocity dispersion field $\sigma_{\rm los}$ for NGC 0410. The model considered is $M_* = 10^{11.79}\,{\rm M}_\odot, b = 1.2, \beta = 3, M_{\rm h}/M_* = 2$. White contours correspond to 150, 175, 200, 225, 250, 275 and 300 km/s.

3.1.2 NGC 4555

NGC 4555 has a falling $\sigma(R)$ profile in the outer regions ($\gamma_{\rm outer} = -0.366$) and $\lambda_{\rm e} = 0.120$, and it has been selected here as representative of a fast rotator. From Table 1, its $R_{\rm e} = 6.4\,{\rm kpc}$. I consider $q = 1 - \varepsilon = 0.80$ and $b < 1.16$, from Equation (24). The stellar mass in Table 1 ($M_* = 10^{11.86}\,{\rm M}_\odot$) is an appropriate value to reproduce the central velocity dispersion profile. For the isotropic case ($b = 1$), $k_0 = 0.65$ and $\xi_0 = 1.5\,R_{\rm e}$ reproduce the observed V profile along the major axis. Also in this case, the model with no dark matter almost reproduces the observed falling σ trend (black curve in Figure 14).

If I add a dark matter halo with $\beta = 3$ and $M_{\rm h}/M_* = 2$ (the same found for NGC 0410), the resulting $\sigma^{\rm LA}_{\rm los}$ profile turns out again to be within the confidence region up to $3.5\,R_{\rm e}$; $f_{\rm DM}$ within $R_{\rm e}$ is again ~ 0.11 (red curve in Figure 14). This result is not totally unexpected because q, M_* and $R_{\rm e}$ are similar to those of NGC 0410.

With the same b and $k(r)$, I consider a dark matter halo with $\beta = 6$ and $M_{\rm h}/M_* = 5$. The difference in the $\sigma^{\rm LA}_{\rm los}(R)$ profile is subtle due to the small amount of dark matter (green curve in Figure 14). From the density profiles shown in Figure 15, dark matter density starts to become more relevant than the stellar density from $\sim 2 - 3\,R_{\rm e}$.

In order to obtain a steeper $\sigma(R)$ profile I increase the anisotropy parameter to 1.1 ($b < 1.16$), using the previous values of β and $M_{\rm h}/M_*$ (green curve in the upper panel of Figure 16). The profile of $\sigma^{\rm LA}_{\rm los}$ is now just a bit steeper, and reproduces the observed σ just a bit better. For the models with $b = 1.1$, $k_0 = 1$ and $\xi_0 = 1\,R_{\rm e}$ reproduce the observed V along the major axis, which has typical values in the range of $\sim 20 - 80$ km/s with a high statistical dispersion: I refer to the highest values of V (lower panel of Figure 16). Note that k_0 must be ≤ 1, so ξ_0 can help reproducing $v_{\rm los}$ in the cases in which a further increase of k_0 is not allowed.

As for NGC 0410, also in this case I find a good agreement between models and observations by consering a halo with $\beta \sim 3 - 6$ and a small amount of dark matter. Even considering a higher radial anisotropy (b above the upper limit of Equation 24), the request of a low $M_{\rm h}$ would remain.

Figures 17 and 18 show the 2D maps of the velocity dispersion and velocity fields, respectively, for the model with $b = 1, \beta = 3, M_{\rm h}/M_* = 2$. As a comparison, Figure 19 shows the 2D map of $\sigma_{\rm los}$ in the presence of radial anisotropy ($b = 1.1$), with a white contours shape analogous to that found in the NGC 0410 modeling.

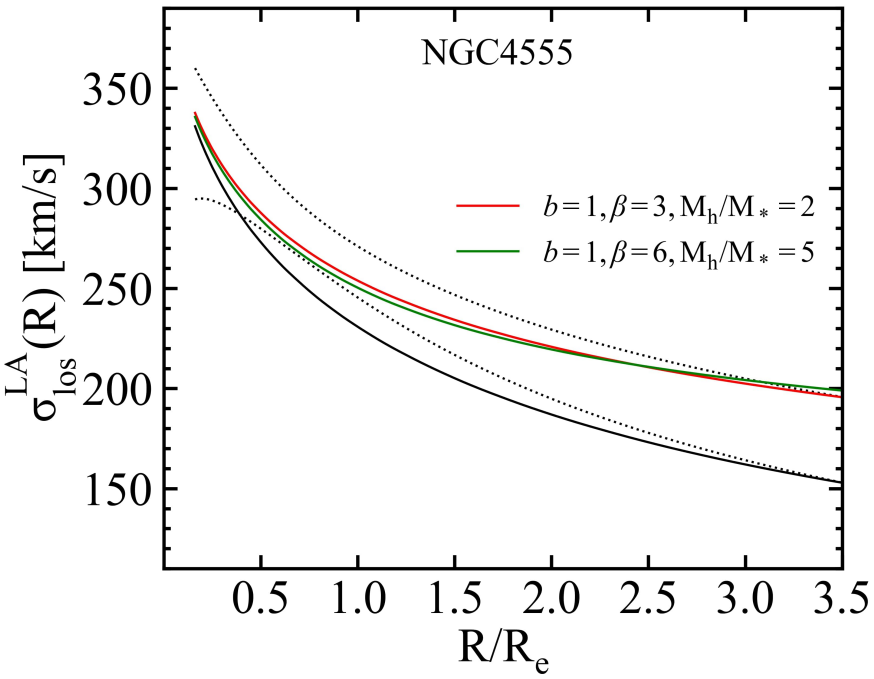

Figure 14: Velocity dispersion luminosity-weighted average $\sigma_{\rm los}^{\rm LA}(R)$ for NGC 4555. The models considered are: no dark matter (black), $\beta = 3, M_{\rm h}/M_* = 2$ (red) and $\beta = 6, M_{\rm h}/M_* = 5$ (green). $b = 1$, $k_0 = 0.65$ and $\xi_0 = 1.5\, R_{\rm e}$ in all three models. The dotted black curves define the confidence region given by $\sigma(R) \pm \Delta\sigma(R)$.

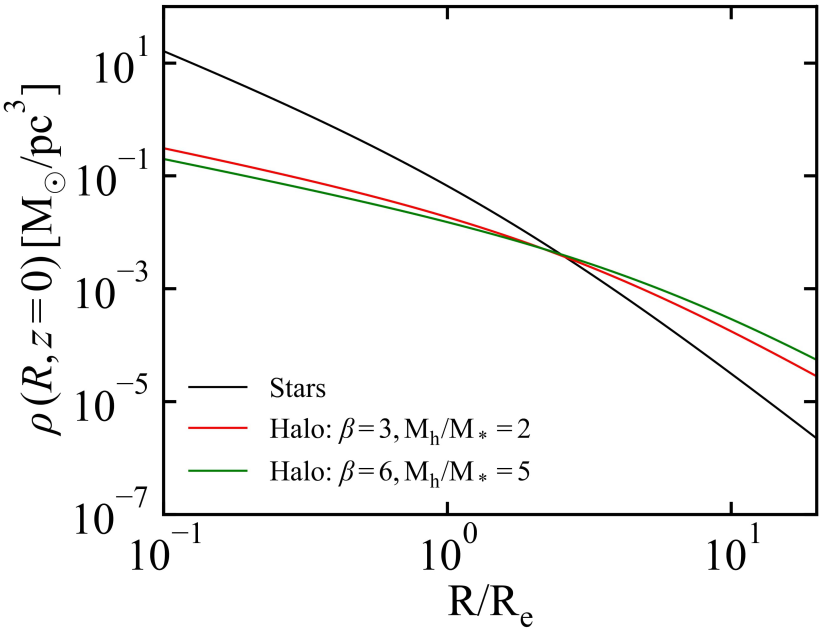

Figure 15: Density profiles for the models in Figure 14: stellar component along the major axis with $M_* = 10^{11.86}\,{\rm M}_\odot$ (black), halo component with $\beta = 3, M_{\rm h}/M_* = 2$ (red) and $\beta = 6, M_{\rm h}/M_* = 5$ (green).

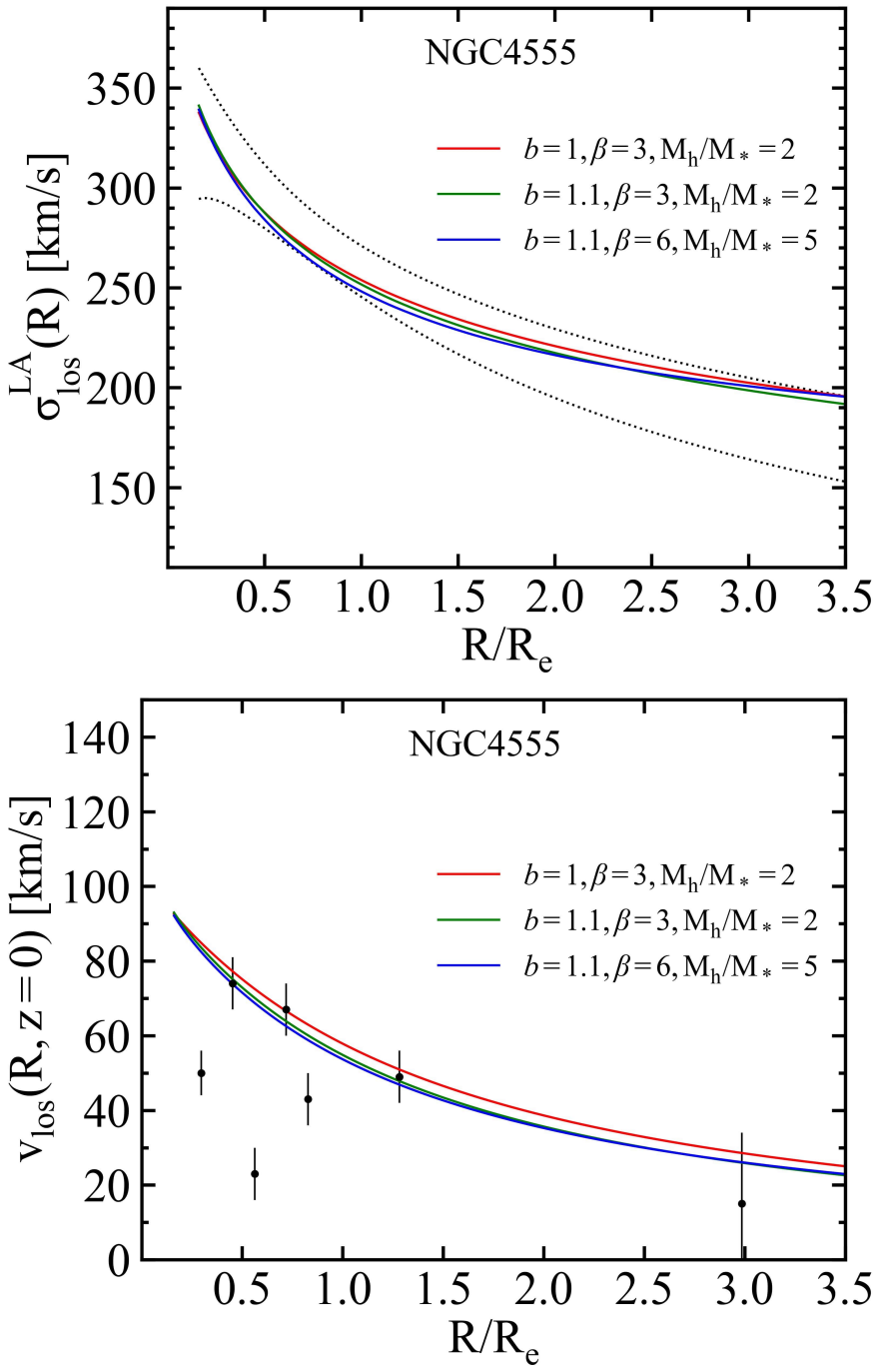

Figure 16: Velocity dispersion luminosity-weighted average $\sigma^{\rm LA}_{\rm los}(R)$ (upper panel) and line-of-sight velocity $v_{\rm los}$ along the major axis (lower panel) for NGC 4555. $k_0 = 0.65$ and $\xi_0 = 1.5\,R_{\rm e}$ for the model with $b = 1$ (red curve). $k_0 = 1$ and $\xi_0 = 1\,R_{\rm e}$ for the models with $b = 1.1$ (green and blue curves). In the upper panel, the dotted black curves define the confidence region given by $\sigma(R) \pm \Delta\sigma(R)$. In the lower panel, the black points with error bars correspond to the observed V along the major axis from Veale et al. (2016).

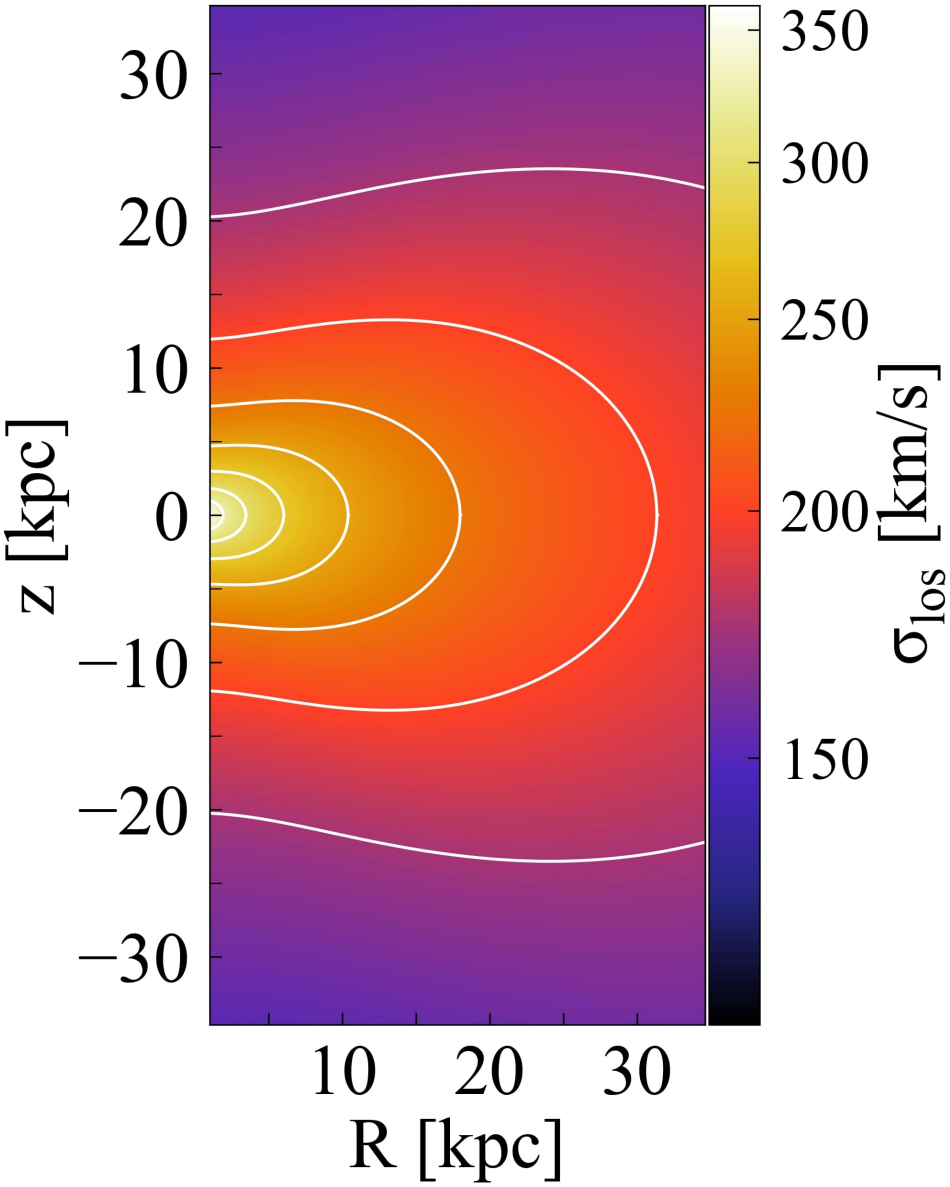

Figure 17: 2D map of the stellar velocity dispersion field $\sigma_{\rm los}$ for NGC 4555. The model considered is $M_* = 10^{11.86}\,{\rm M}_\odot, b = 1, \beta = 3, M_{\rm h}/M_* = 2$. White contours correspond to 175, 200, 225, 250, 275, 300 and 325 km/s.

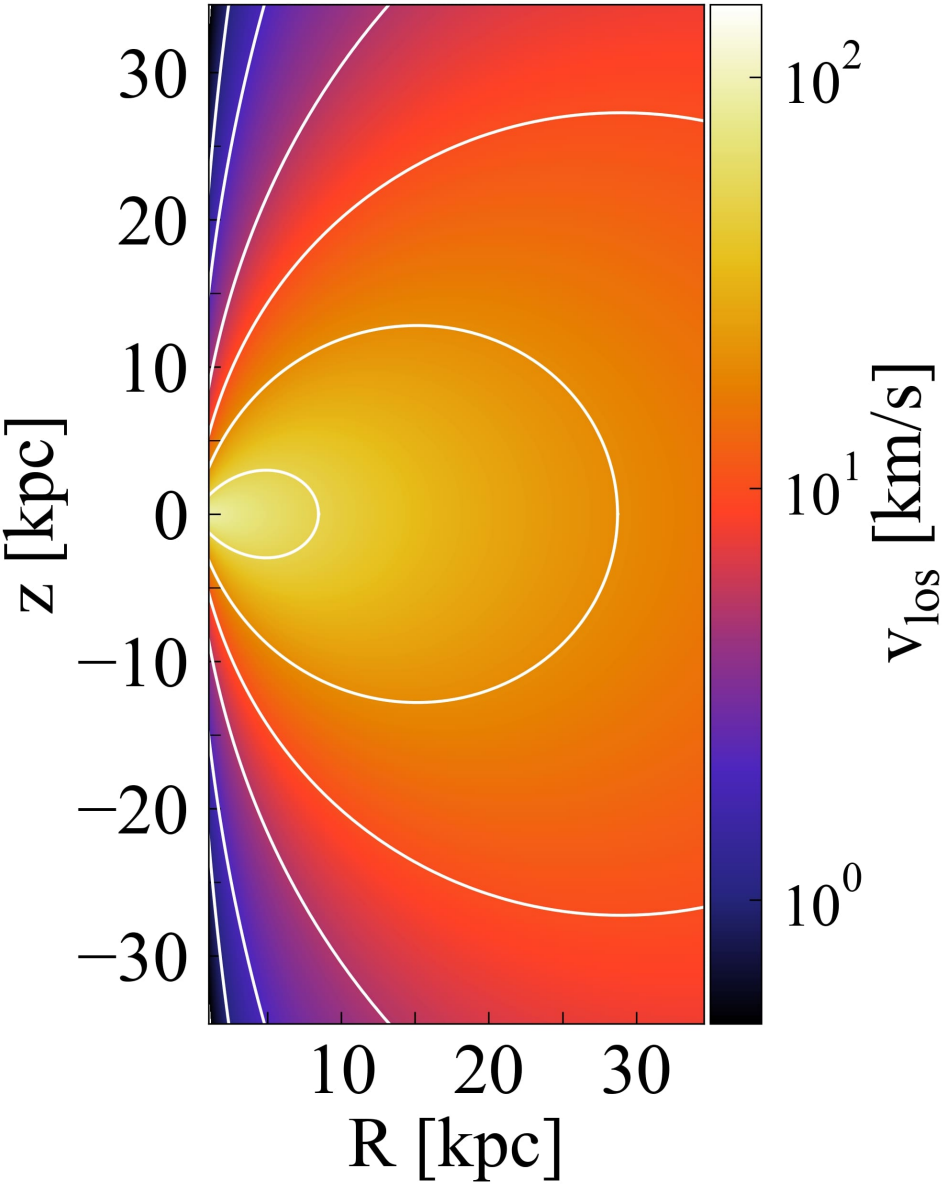

Figure 18: 2D map of the stellar velocity field $v_{\rm los}$ for NGC 4555. The model considered is $M_* = 10^{11.86}\,{\rm M}_\odot, b = 1, \beta = 3, M_{\rm h}/M_* = 2$. White contours correspond to 1, 2, 5, 10, 20 and 50 km/s.

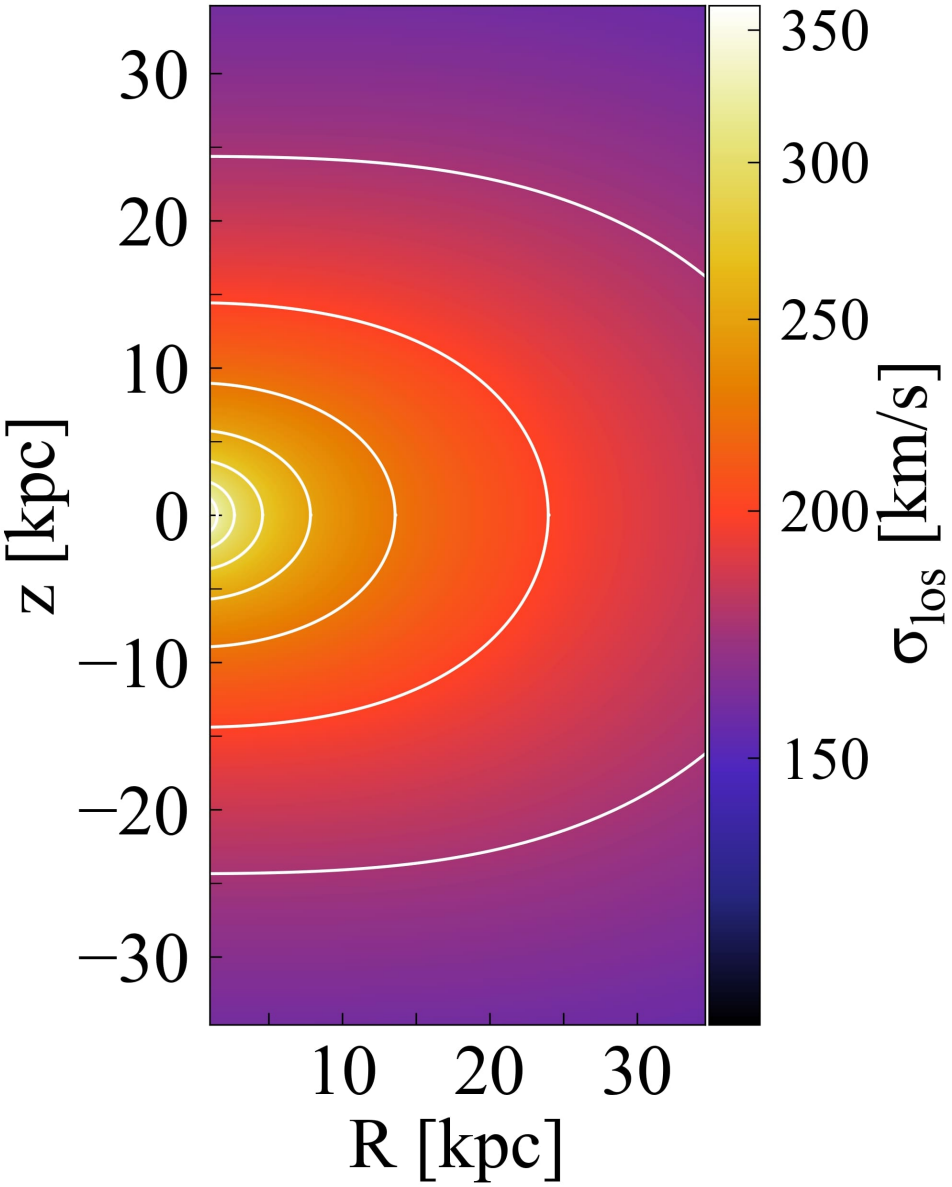

Figure 19: 2D map of the stellar velocity dispersion field $\sigma_{\rm los}$ for NGC 4555. The model considered is $M_* = 10^{11.86}\,{\rm M}_\odot, b = 1.1, \beta = 3, M_{\rm h}/M_* = 2$. White contours correspond to 175, 200, 225, 250, 275, 300 and 325 km/s.

3.2 Flat profiles

In this section I present the modeling of NGC 2340 and NGC 3158, the two galaxies with a flat σ profile chosen for this work. Here the aim is to check if the modeling results are different, in terms of b, β and $M_{\rm h}$, from those found for the two galaxies with falling σ profiles.

3.2.1 NGC 2340

NGC 2340 has a flat $\sigma(R)$ profile in the outer regions ($\gamma_{\rm outer} = 0.033$) and $\lambda_{\rm e} = 0.032$. From Table 1, its $R_{\rm e} = 14.3\,{\rm kpc}$. I consider $q = 1 - \varepsilon = 0.56$ and $b < 1.45$, from Equation (24). The stellar mass value in Table 1 ($M_* = 10^{11.86}\,{\rm M}_\odot$) is already appropriate to reproduce the central velocity dispersion profile. For the isotropic case ($b = 1$), $k_0 = 0.05$ and $\xi_0 = 2\,R_{\rm e}$ reproduce well the observed V profile along the major axis. The model with no dark matter results to be much lower than the observed $\sigma(R)$ profile (black curve in Figure 20).

The first step I take in the modeling is the addition of a dark matter halo with $\beta = 3$ and $M_{\rm h}/M_* = 2$, the same considered for the previous two galaxies: the $\sigma^{\rm LA}_{\rm los}$ profile is still far from the confidence region (red curve in Figure 20). With $\beta = 3$, I increase $M_{\rm h}/M_*$ until the observed σ is reproduced reasonably well. I find a good agreement with $M_{\rm h}/M_* = 10$ (green line in Figure 23): this leads to a higher dark matter fraction ($f_{\rm DM} \sim 0.39$ within $R_{\rm e}$) compared to those of the successful model of the previous two galaxies.

With the same b and $k(r)$ I consider $\beta = 6$: I need to increase $M_{\rm h}/M_*$ by a factor of ~ 3, up to 30. Even if this ratio would be more plausible, this model is less appropriate to reproduce the observed σ (blue curve in Figure 23). The $\sigma^{\rm LA}_{\rm los}$ profile is now steeper within $0.5\,R_{\rm e}$ and rising in the outer regions, with $f_{\rm DM} \sim 0.37$ within $R_{\rm e}$. From Figure 21, dark matter density overcomes the stellar density from $\sim 1\,R_{\rm e}$. In the modeling of the falling profiles of NGC 0410 and NGC 4555, instead, the dark matter started to become relevant outside $\sim 2 - 3\,R_{\rm e}$.

With the constraint of $b < 1.45$ (since $\varepsilon = 0.56$), I make a model with radial anisotropy ($b = 1.4$). In this case, the high value of b significantly raises the central velocity dispersion. This effect can be compensated for by lowering M_* to $10^{11.79}\,{\rm M}_\odot$ (0.5σ from Cappellari (2013) relation), so I adopt this stellar mass value for the models with $b = 1.4$. Differently from β and $M_{\rm h}$, the stellar mass M_* significantly influences $\sigma^{\rm LA}_{\rm los}(R)$ in the central regions. I consider again a dark matter halo with $\beta = 3$ and vary the amount of dark matter, until I obtain a profile within the confidence region for $M_{\rm h}/M_* = 14$ (green curve in the upper panel of Figure 22). In this case ($b = 1.4$), $k_0 = 0.1$ and $\xi_0 = 1\,R_{\rm e}$ reproduce well the observed V along the major axis, which has typical values in the range of $\sim 5 - 15$ km/s (lower panel of Figure 22). Quite remarkably, for NGC 2340 I can reproduce the observed σ profile with two distinct models, having different M_*, $M_{\rm h}$ and b. Since I decreased M_* and increased $M_{\rm h}$, the model with radial anisotropy has a higher dark matter fraction: $f_{\rm DM} \sim 0.47$ within $R_{\rm e}$. I also model a dark matter

halo with $\beta = 6$ and $M_{\rm h}/M_* = 40$ (blue curve in the upper panel of Figure 22) but, as I noted for the isotropic model, this leads to a $\sigma_{\rm los}^{\rm LA}$ profile that is steeper within $0.5\,R_{\rm e}$ and rising in the outer regions, with $f_{\rm DM} \sim 0.44$ within $R_{\rm e}$.

For NGC 2340, the requested $M_{\rm h}/M_*$ is higher by a factor of $\sim 5-7$ compared to those of the previous two galaxies: this leads to $f_{\rm DM}$ within $R_{\rm e}$ being higher by a factor of $\sim 3-4$ but still in agreement with that of cosmological simulations in the literature (Lovell et al. 2018). The constraint on β is now stronger compared to what I found for NGC 0410 and NGC 4555: β must be low (~ 3) so that the $\sigma_{\rm los}^{\rm LA}$ profile shows no decline within $0.5\,R_{\rm e}$ and is almost always flat. The isotropic model already reproduces the observations, but radial anisotropy is still plausible (red and green curves in the upper panel of Figure 22). Recall that M_* is lower in the anisotropic case.

Figures 23 and 24 show the 2D maps of the velocity dispersion and velocity fields, respectively, for the model with $b = 1, \beta = 3, M_{\rm h}/M_* = 10$. The white contours, indicating regions of equal $\sigma_{\rm los}$, are no longer closed (as for NGC 0410) due to the presence of a more massive dark matter halo. Note that $\sigma_{\rm los}$ is always above 250 km/s along the major axis but often below 200 km/s along the minor axis. This still allows to have a flat $\sigma_{\rm los}^{\rm LA}$ profile since it is a luminosity-weighted average made for each radius R. As a comparison, Figure 25 shows the 2D map of $\sigma_{\rm los}$ in the presence of radial anisotropy ($b = 1.4$). In this case $\sigma_{\rm los}$ has more homogeneous values considering different R and z.

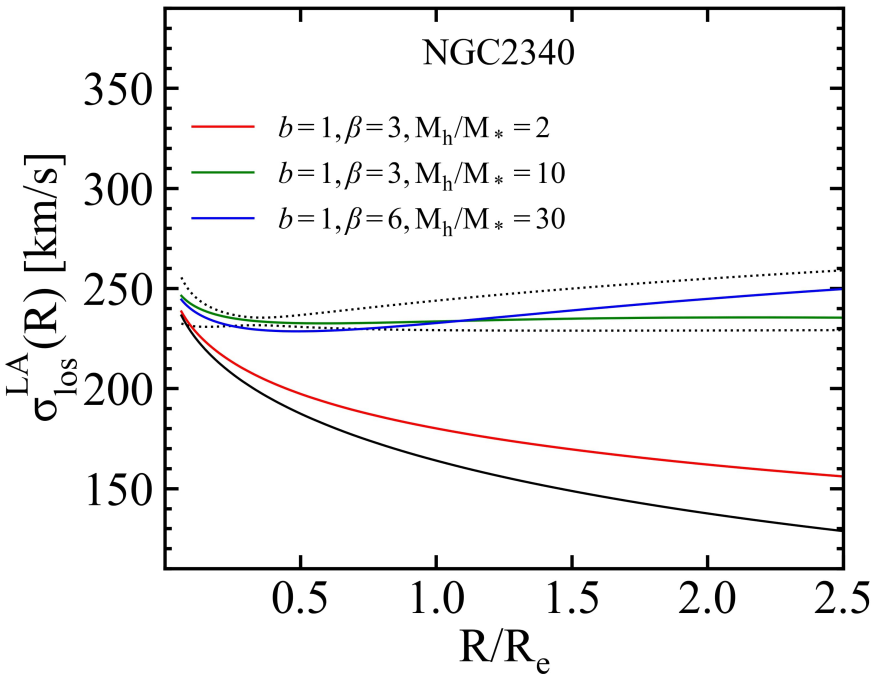

Figure 20: Velocity dispersion luminosity-weighted average $\sigma^{\mathrm{LA}}_{\mathrm{los}}(R)$ for NGC 2340. The models considered are: no dark matter (black), $\beta = 3, M_{\mathrm{h}}/M_* = 2$ (red), $\beta = 3, M_{\mathrm{h}}/M_* = 10$ (green) and $\beta = 6, M_{\mathrm{h}}/M_* = 30$ (blue). $b = 1$, $k_0 = 0.05$ and $\xi_0 = 2\,R_{\mathrm{e}}$ in all four models. The dotted black curves define the confidence region given by $\sigma(R) \pm \Delta\sigma(R)$.

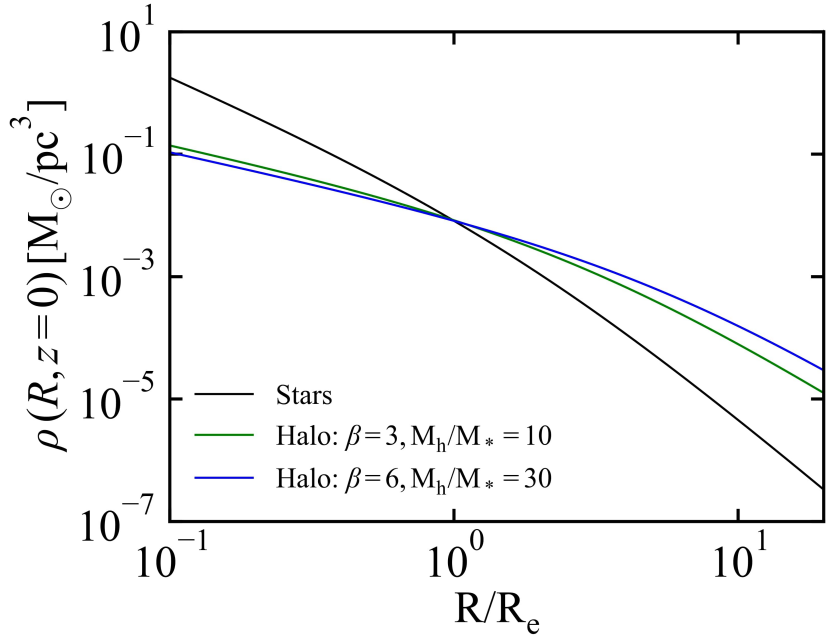

Figure 21: Density profiles for the models in Figure 20: stellar component along the major axis with $M_* = 10^{11.86}\,\mathrm{M}_\odot$ (black), halo component with $\beta = 3, M_{\mathrm{h}}/M_* = 10$ (green) and $\beta = 6, M_{\mathrm{h}}/M_* = 30$ (blue).

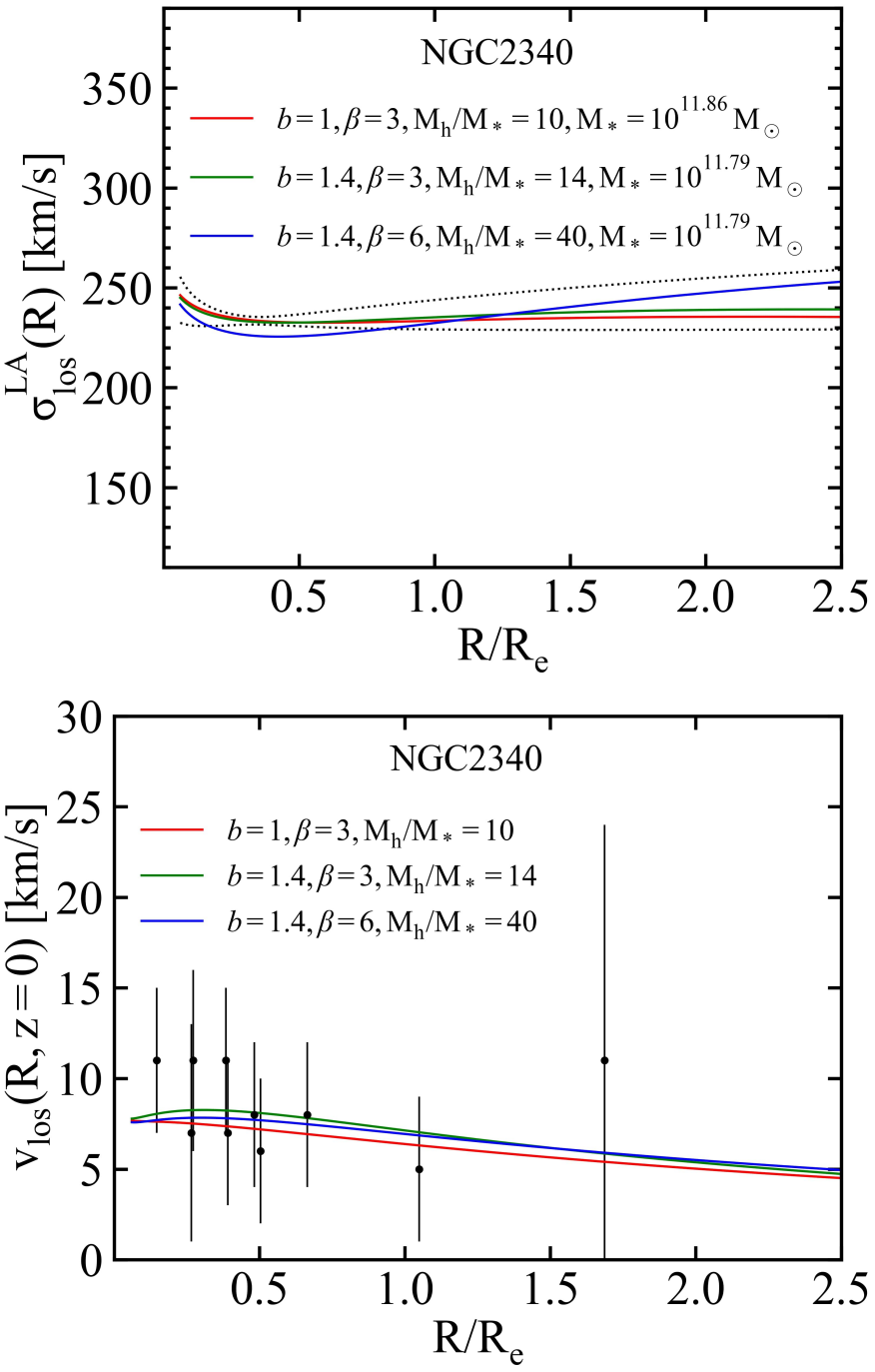

Figure 22: Velocity dispersion luminosity-weighted average $\sigma_{\rm los}^{\rm LA}(R)$ (upper panel) and line-of-sight velocity $v_{\rm los}$ along the major axis (lower panel) for NGC 2340. $k_0 = 0.05$ and $\xi_0 = 2\,R_{\rm e}$ for the model with $b = 1$ (red curve). $k_0 = 0.1$ and $\xi_0 = 1\,R_{\rm e}$ for the models with $b = 1.4$ (green and blue curves). Note that the models with $b = 1.4$ have $M_* = 10^{11.79}\,{\rm M}_\odot$. In the upper panel, the dotted black curves define the confidence region given by $\sigma(R) \pm \Delta\sigma(R)$. In the lower panel, the black points with error bars correspond to the observed V along the major axis from Veale et al. (2016).

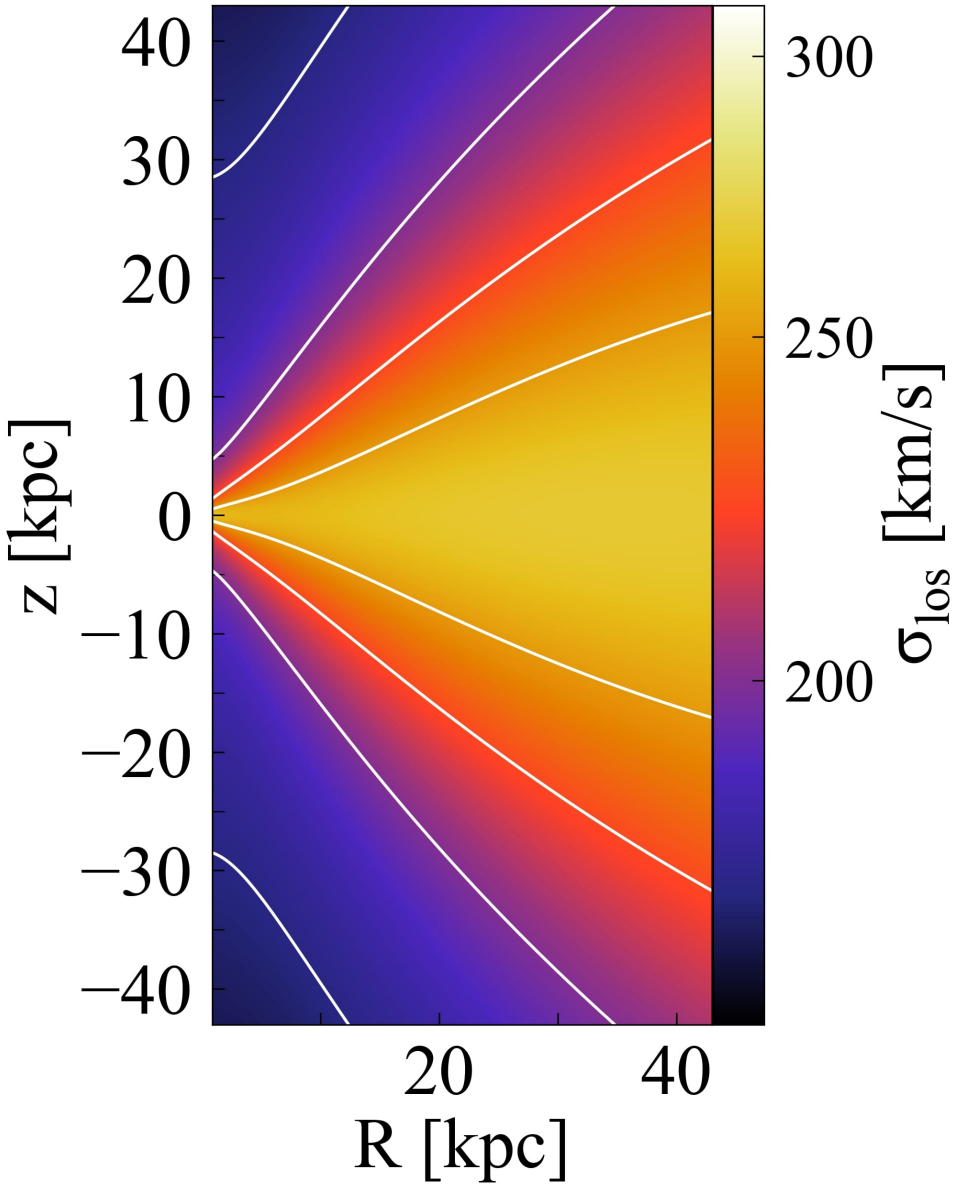

Figure 23: 2D map of the stellar velocity dispersion field $\sigma_{\rm los}$ for NGC 2340. The model considered is $M_* = 10^{11.86}\,{\rm M}_\odot, b = 1, \beta = 3, M_{\rm h}/M_* = 10$. White contours correspond to 175, 200, 225 and 250 km/s.

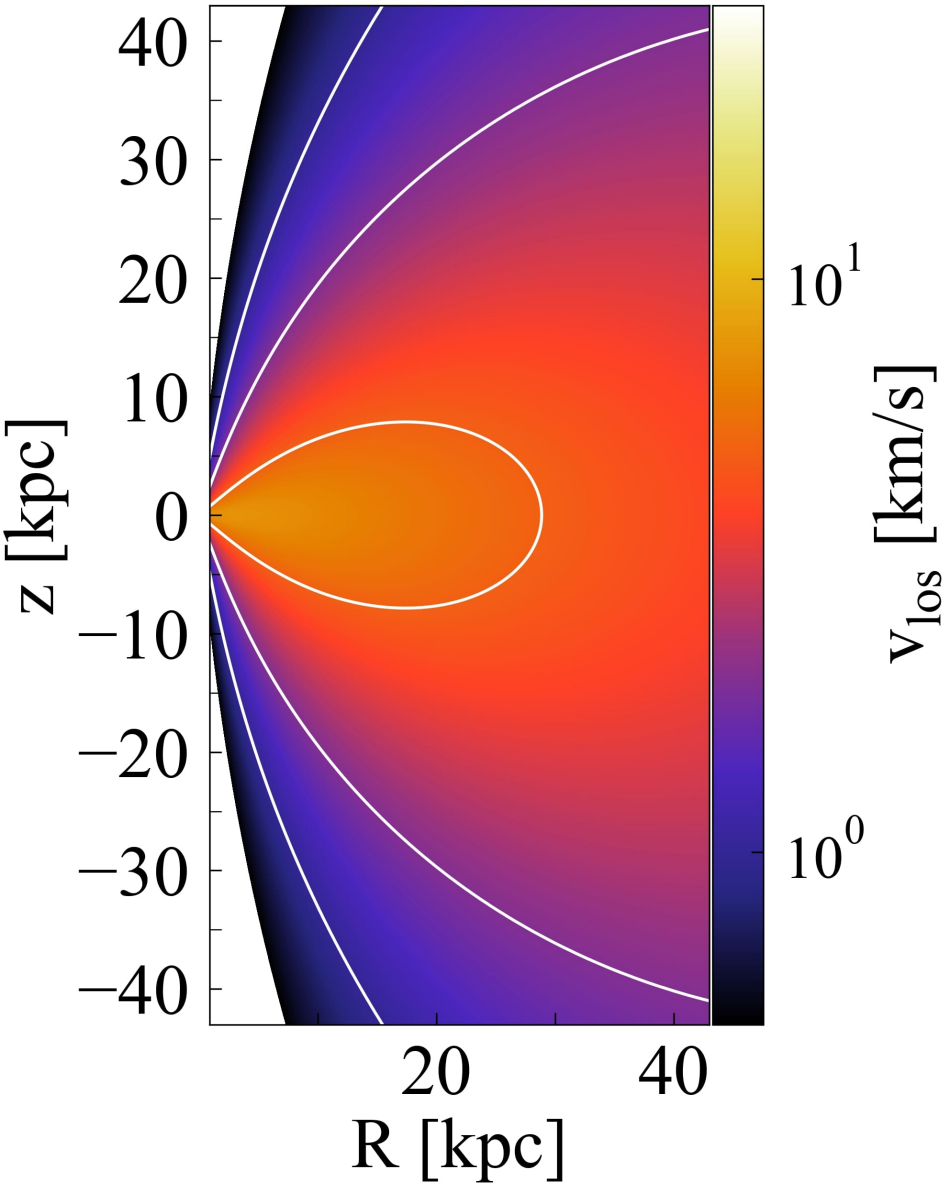

Figure 24: 2D map of the stellar velocity field $v_{\rm los}$ for NGC 2340. The model considered is $M_* = 10^{11.86}\,{\rm M}_\odot, b = 1, \beta = 3, M_{\rm h}/M_* = 10$. White contours correspond to 1, 2 and 5 km/s.

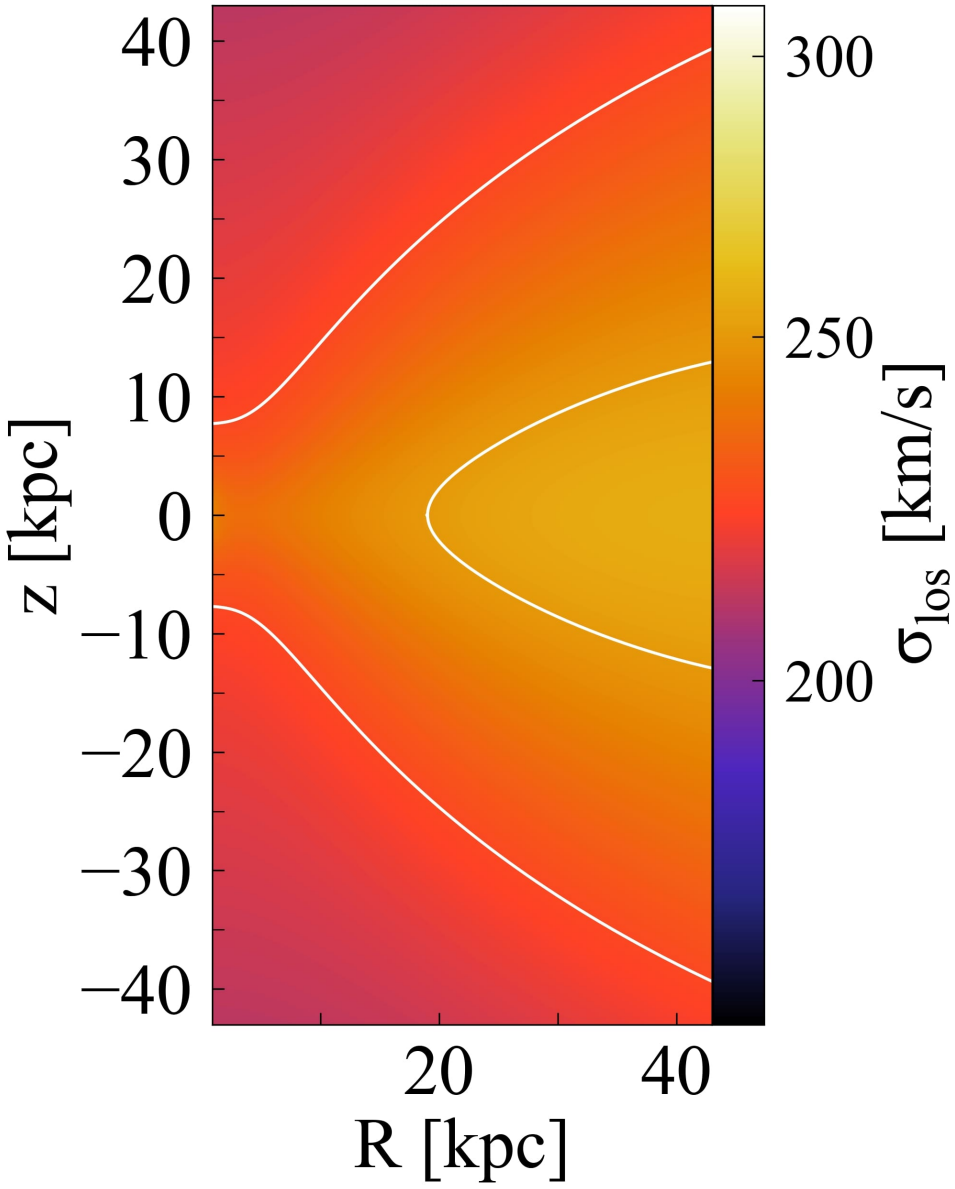

Figure 25: 2D map of the stellar velocity dispersion field $\sigma_{\rm los}$ for NGC 2340. The model considered is $M_* = 10^{11.79}\,\mathrm{M}_\odot, b = 1.4, \beta = 3, M_{\rm h}/M_* = 14$. White contours correspond to 225 and 250 km/s.

3.2.2 NGC 3158

NGC 3158 has a flat $\sigma(R)$ profile in the outer regions ($\gamma_{\rm outer} = 0.008$) and $\lambda_{\rm e} = 0.255$. From Table 1, its $R_{\rm e} \sim 8.1\,{\rm kpc}$. I consider $q = 1 - \varepsilon = 0.82$ and $b < 1.14$, from Equation (24). The stellar mass in Table 1 is $10^{12.02}\,{\rm M}_\odot$, but in the preliminary modeling I find $M_* = 10^{11.74}\,{\rm M}_\odot$ (2σ from Cappellari (2013) relation) more appropriate to reproduce the central velocity dispersion profile. For the isotropic case ($b = 1$), $k_0 = 0.95$ and $\xi_0 = 2\,R_{\rm e}$ reproduce the observed V profile along the major axis. Also in this case, the model with no dark matter results to be too low with respect to the observed σ profile (black curve in Figure 26).

I first add a dark matter halo with $\beta = 3$ and $M_{\rm h}/M_* = 2$ (like the one considered for NGC 0410 and NGC 4555), and again the $\sigma^{\rm LA}_{\rm los}$ profile is too low (red curve in Figure 26). Then, with $\beta = 3$, I can reproduce well the observations increasing $M_{\rm h}/M_*$ to 15 (green line in Figure 26): this results in $f_{\rm DM} \sim 0.48$ within $R_{\rm e}$. With the same b and $k(r)$, for $\beta = 6$ I need to increase $M_{\rm h}/M_*$ up to 40; as happened for NGC 2340, this results in low $\sigma^{\rm LA}_{\rm los}$ values within $1\,R_{\rm e}$ and a rising profile in the outer regions ($f_{\rm DM} \sim 0.42$ within $R_{\rm e}$). Density profiles are shown in Figure 27: dark matter is already relevant within $\sim 1\,R_{\rm e}$.

With the constraint of $b < 1.14$, I increase the anisotropy parameter to 1.1, and adopt the previous values of β and $M_{\rm h}/M_*$. I find a slightly better agreement with the observed σ profile, especially in the inner regions (green curve in the upper panel of Figure 28). The observed V along the major axis has typical values in the range of $\sim 60 - 120$ km/s (lower panel in Figure 28): for the models with $b = 1.1$ I consider $k_0 = 1$ and $\xi_0 = 2.5\,R_{\rm e}$, but the observed V is reproduced better in the isotropic case.

Remarkably, I find similar results (in terms of β and $M_{\rm h}/M_*$) as obtained for NGC 2340, the other galaxy with a flat σ profile: also in this case I find $\beta \sim 3$ and $M_{\rm h}/M_*$ significantly higher than for NGC 0410 and NGC 4555. I find a similar amount and distribution of the dark matter component between slow and fast rotators with the same observed shape of the σ profile. Both values of b (1 and 1.1) allow to reproduce the observed σ but the isotropic model reproduces better the observed V, for the adopted parameterization of $\overline{v_\varphi}$ (it depends on k_0 and ξ_0).

Figures 29 and 30 show the 2D maps of the velocity dispersion and velocity fields, respectively, for the model with $b = 1, \beta = 3, M_{\rm h}/M_* = 15$. In this case, $\sigma_{\rm los}$ values go from ~ 250 km/s to ~ 300 km/s. The addition of radial anisotropy smooths the $\sigma_{\rm los}$ 2D map (Figure 31): values are almost everywhere around 275 km/s.

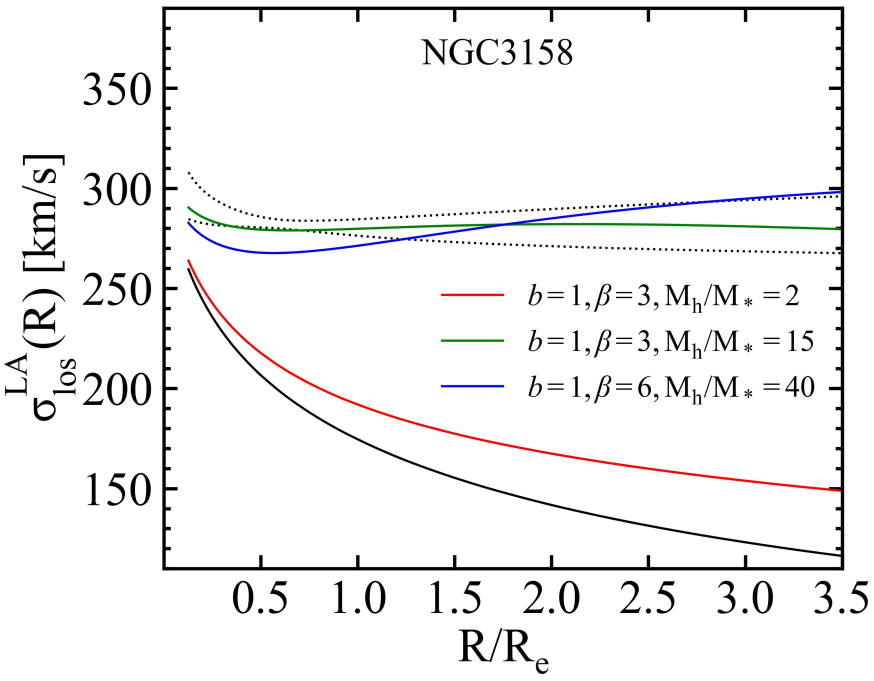

Figure 26: Velocity dispersion luminosity-weighted average $\sigma^{\rm LA}_{\rm los}(R)$ for NGC 3158. The models considered are: no dark matter (black), $\beta = 3, M_{\rm h}/M_* = 2$ (red), $\beta = 3, M_{\rm h}/M_* = 15$ (green) and $\beta = 6, M_{\rm h}/M_* = 40$ (blue). $b = 1$, $k_0 = 0.95$ and $\xi_0 = 2\,R_{\rm e}$ in all four models. The dotted black curves define the confidence region given by $\sigma(R) \pm \Delta\sigma(R)$.

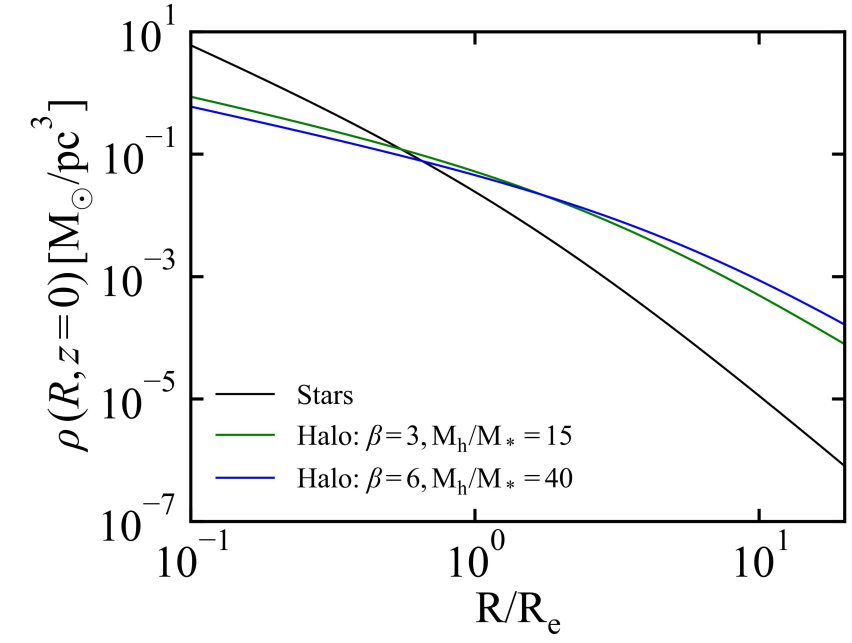

Figure 27: Density profiles for the models in Figure 26: stellar component along the major axis with $M_* = 10^{11.74}\,{\rm M}_\odot$ (black), halo component with $\beta = 3, M_{\rm h}/M_* = 15$ (green) and $\beta = 6, M_{\rm h}/M_* = 40$ (blue).

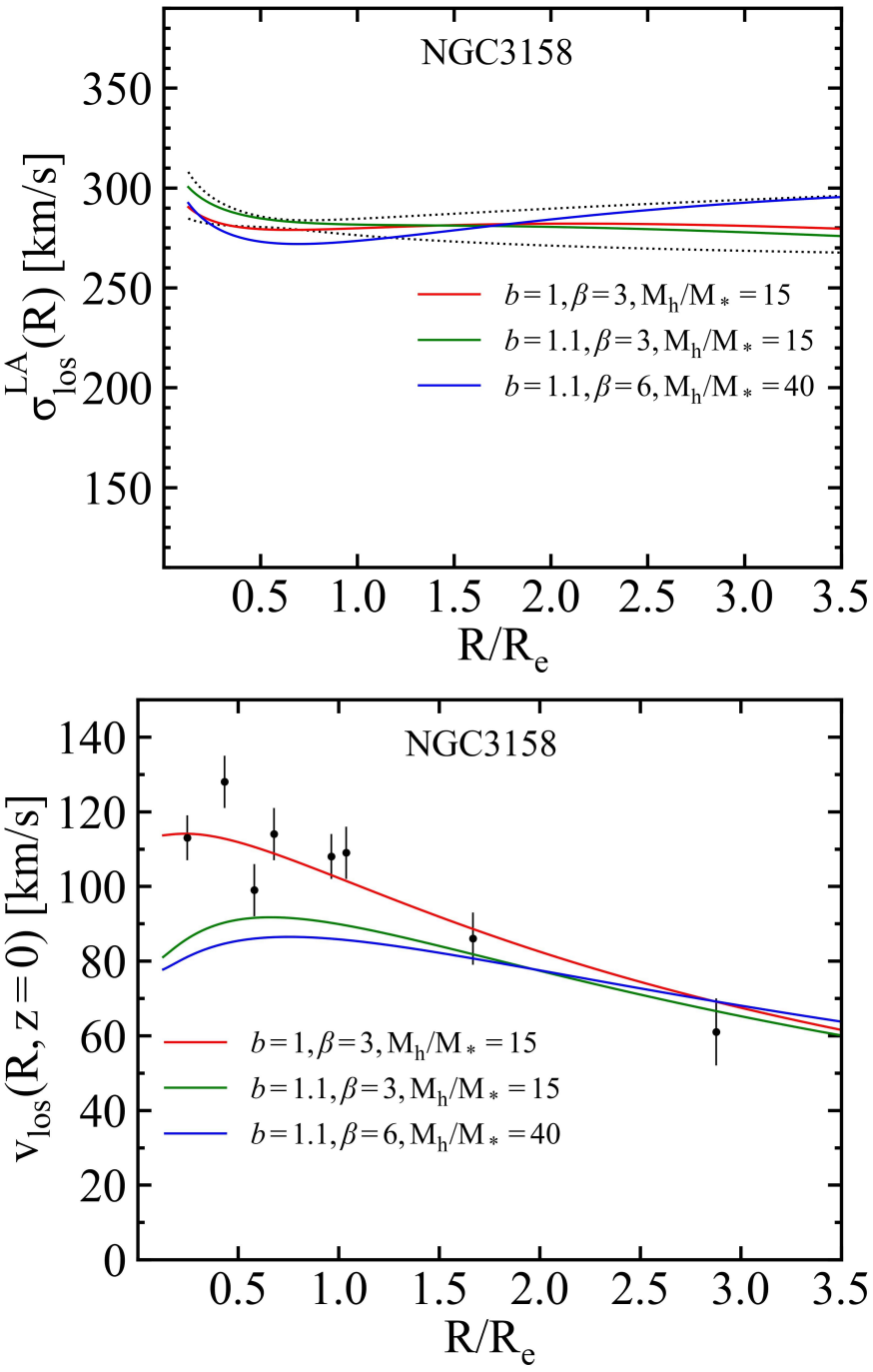

Figure 28: Velocity dispersion luminosity-weighted average $\sigma^{\rm LA}_{\rm los}(R)$ (upper panel) and line-of-sight velocity $v_{\rm los}$ along the major axis (lower panel) for NGC 3158. $k_0 = 0.95$ and $\xi_0 = 2\,R_{\rm e}$ for the model with $b = 1$ (red curve). $k_0 = 1$ and $\xi_0 = 2.5\,R_{\rm e}$ for the models with $b = 1.1$ (green and blue curves). In the upper panel, the dotted black curves define the confidence region given by $\sigma(R) \pm \Delta\sigma(R)$. In the lower panel, the black points with error bars correspond to the observed V along the major axis from Veale et al. (2016).

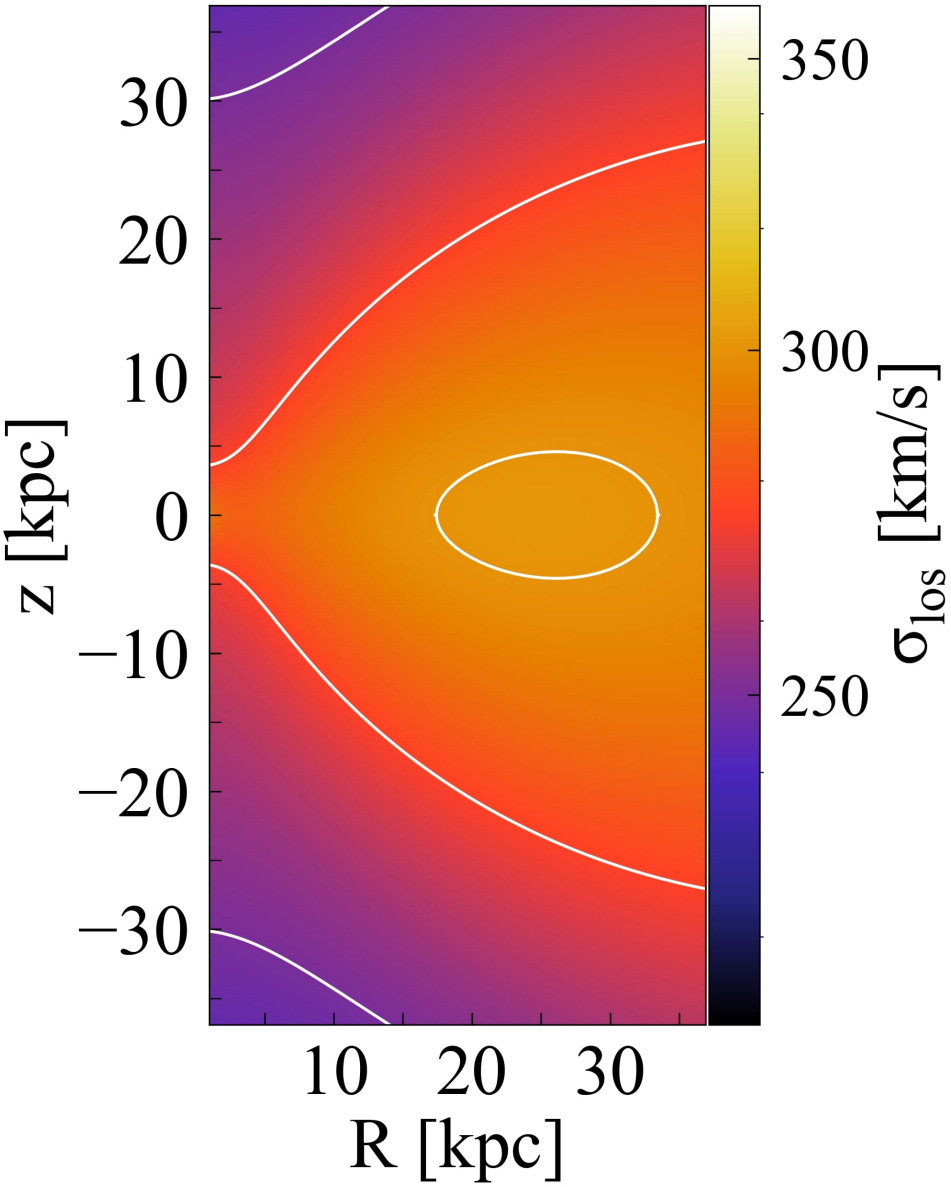

Figure 29: 2D map of the stellar velocity dispersion field $\sigma_{\rm los}$ for NGC 3158. The model considered is $M_* = 10^{11.74}\,{\rm M}_\odot, b = 1, \beta = 3, M_{\rm h}/M_* = 15$. White contours correspond to 250, 275 and 300 km/s.

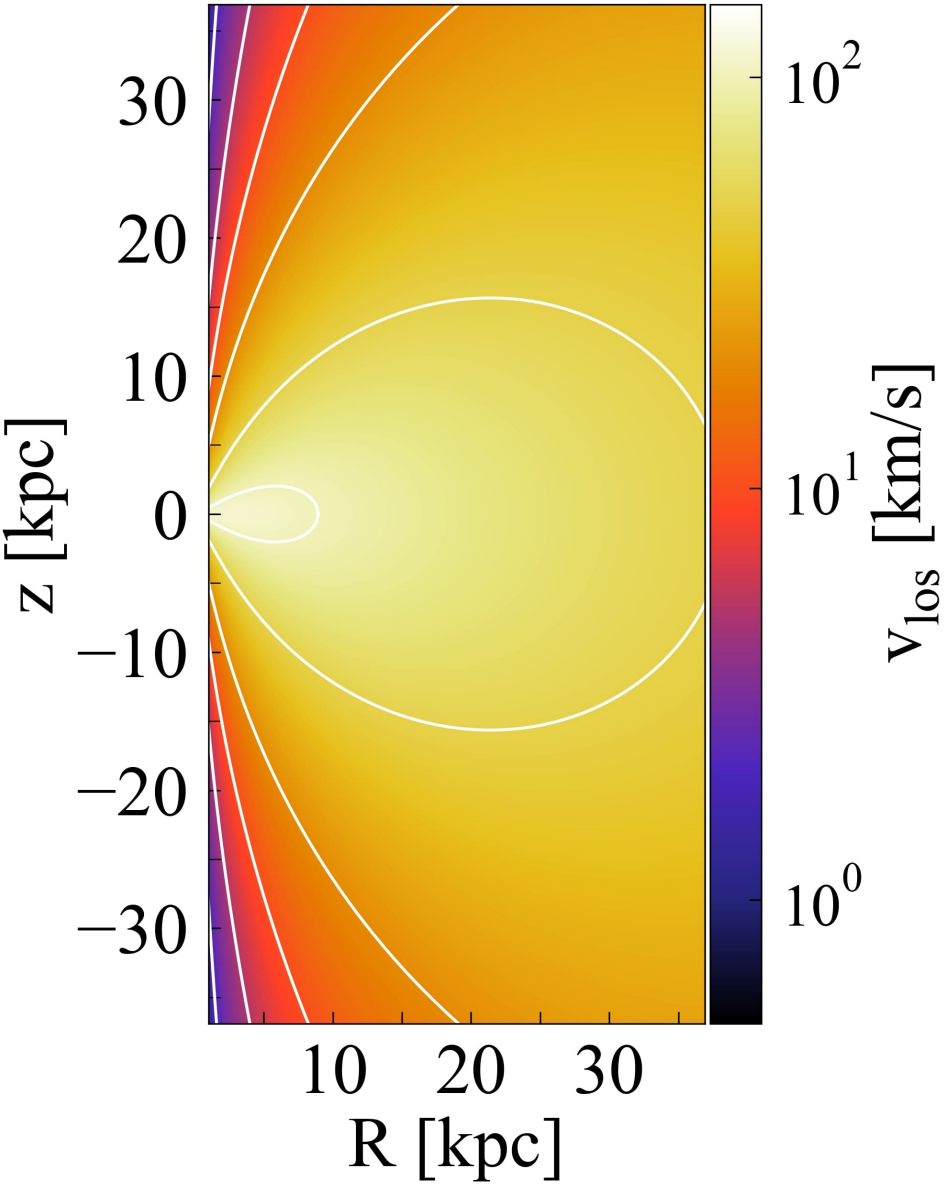

Figure 30: 2D map of the stellar velocity field $v_{\rm los}$ for NGC 3158. The model considered is $M_* = 10^{11.74}\,{\rm M}_\odot, b = 1, \beta = 3, M_{\rm h}/M_* = 15$. White contours correspond to 2, 5, 10, 20, 50 and 100 km/s.

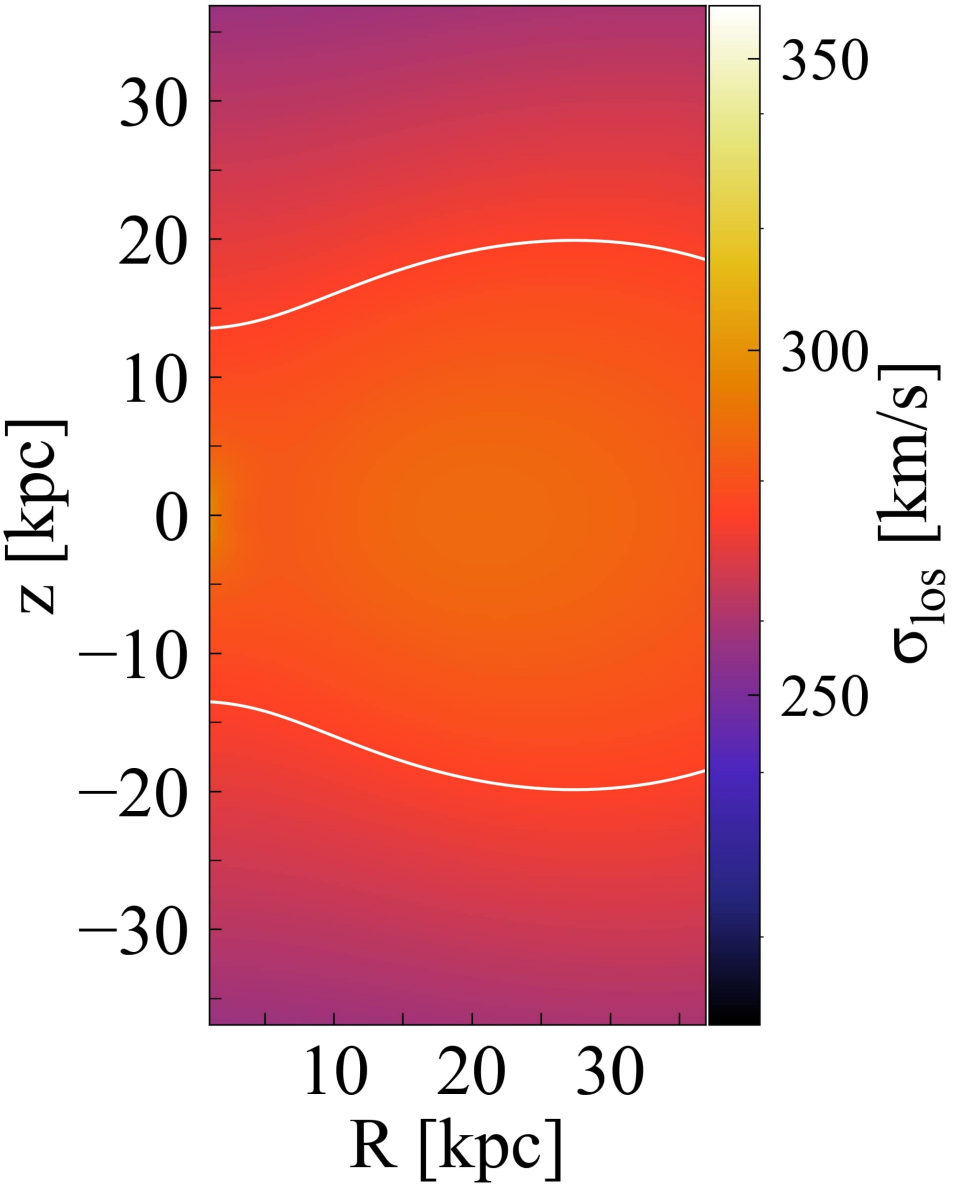

Figure 31: 2D map of the stellar velocity dispersion field $\sigma_{\rm los}$ for NGC 3158. The model considered is $M_* = 10^{11.74}\,{\rm M}_\odot, b = 1.1, \beta = 3, M_{\rm h}/M_* = 15$. The white contour correspond to 275 km/s.

3.3 Rising profiles

In this section I present the modeling of NGC 4073 and NGC 0383, the two galaxies with a rising σ profile chosen for this work. Here the aim is to check if the suggested positive trend of the dark matter amount at the increase of $\gamma_{\rm outer}$ still holds for galaxies with rising σ profiles. The purpose is also to better understand if anisotropy is important to explain the different observed σ trends among massive early-type galaxies, or if variations of the mass profile have a primary role in this.

3.3.1 NGC 4073

NGC 4073 has a rising $\sigma(R)$ profile in the outer regions ($\gamma_{\rm outer} = 0.198$) and $\lambda_{\rm e} = 0.023$. From Table 1, its $R_{\rm e} \sim 10.2\,$kpc. I consider $q = 1 - \varepsilon = 0.68$ and $b < 1.29$, from Equation (24). The stellar mass in Table 1 is $10^{12.05}\,{\rm M}_{\odot}$, but in the preliminary modeling I find $M_* = 10^{11.91}\,{\rm M}_{\odot}$ (1σ from Cappellari (2013) relation) more appropriate to reproduce the central velocity dispersion profile. For the isotropic case ($b = 1$), $k_0 = 0.05$ and $\xi_0 = 2\,R_{\rm e}$ reproduce well the observed V profile along the major axis. The model with no dark matter (black curve in Figure 32) as always leads to a falling velocity dispersion profile.

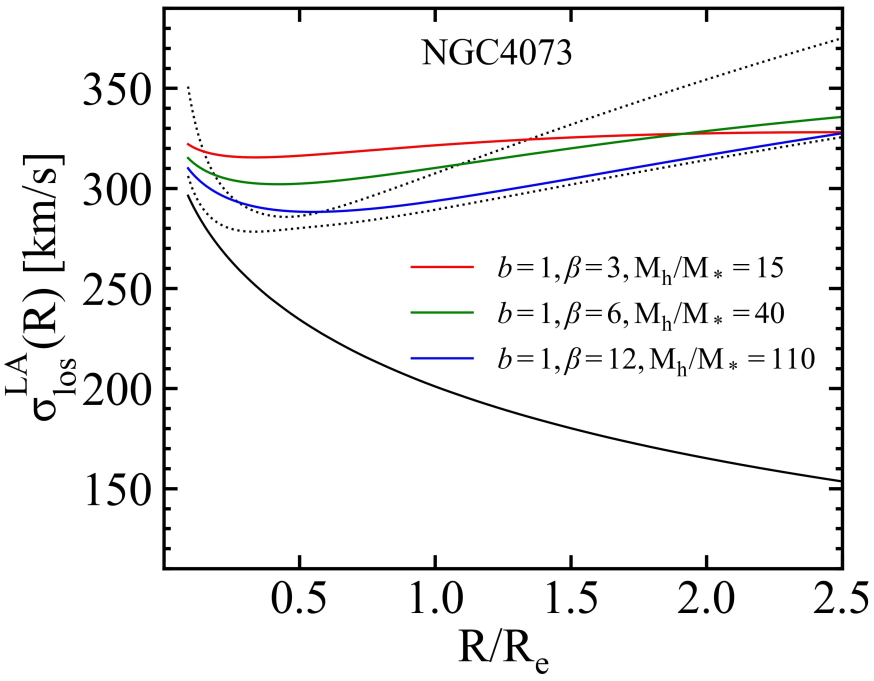

Figure 32: Velocity dispersion luminosity-weighted average $\sigma^{\rm LA}_{\rm los}(R)$ for NGC 4073. The models considered are: no dark matter (black), $\beta = 3, M_{\rm h}/M_* = 15$ (red), $\beta = 6, M_{\rm h}/M_* = 40$ (green) and $\beta = 12, M_{\rm h}/M_* = 110$ (blue). $b = 1$, $k_0 = 0.05$ and $\xi_0 = 2\,R_{\rm e}$ in all four models. The dotted black curves define the confidence region given by $\sigma(R) \pm \Delta\sigma(R)$.

I add a dark matter halo like the one that gives a good modeling for NGC 3158, with $\beta = 3$ and $M_{\rm h}/M_* = 15$ (red curve in Figure 32). The resulting model shows a $\sigma_{\rm los}^{\rm LA}$ profile well above the confidence region within $\sim 1\,R_{\rm e}$. This suggests to increase β to lower the dark matter amount in the central part of the galaxy (as seen in the modeling of the previous case).

As expected, with $\beta = 6$ and $M_{\rm h}/M_* = 40$ I can reproduce better σ in the central region (green line in Figure 32). This model allows to have a little decline in the $\sigma_{\rm los}^{\rm LA}$ profile within $\sim 0.5\,R_{\rm e}$ and a rise in the outer regions, with $f_{\rm DM} \sim 0.42$ within $R_{\rm e}$. Following this line of reasoning, I further increase β to 12 and change the dark matter mass accordingly, finding a good model with $M_{\rm h}/M_* = 110$ (blue line in Figure 32): in this case $f_{\rm DM} \sim 0.36$ within $R_{\rm e}$. For the three haloes considered, dark matter density starts to become more relevant than the stellar density from $\sim 1\,R_{\rm e}$ (Figure 33).

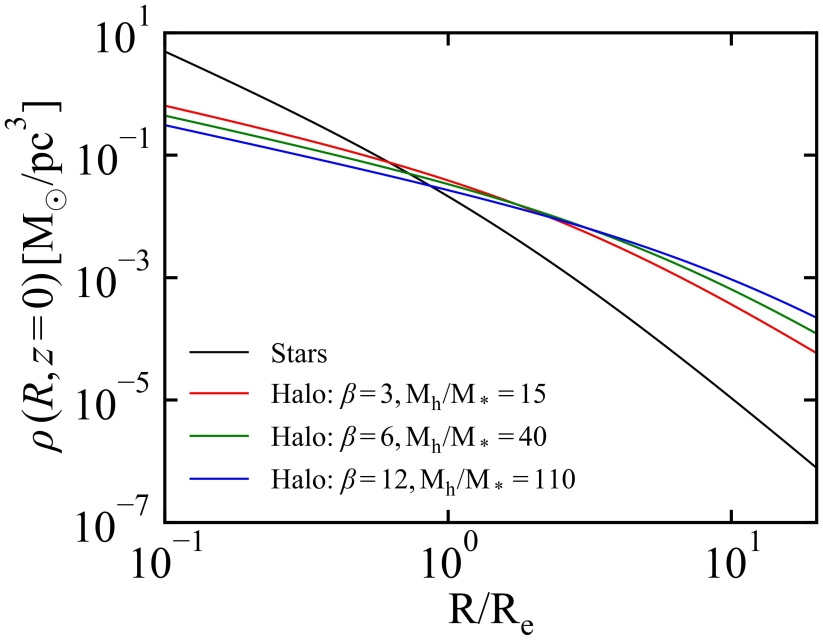

Figure 33: Density profiles for the models in Figure 32: stellar component along the major axis with $M_* = 10^{11.91}\,\mathrm{M}_\odot$ (black), halo component with $\beta = 3, M_{\rm h}/M_* = 15$ (red), $\beta = 6, M_{\rm h}/M_* = 40$ (green) and $\beta = 12, M_{\rm h}/M_* = 110$ (blue).

Since adding radial anisotropy would result in a less rising σ profile in the outer regions, an effect opposite to that needed, I further model this galaxy by adding tangential anisotropy ($b < 1$). For the previous values of $\beta = 12$ and $M_{\rm h}/M_* = 110$, adopting $b = 0.8$ allows to reproduce σ a bit better in the inner regions (blue curve in the upper panel of Figure 34). For these models with $b = 0.8$, $k_0 = 0.05$ and $\xi_0 = 1.5\,R_{\rm e}$ reproduce the observed V along the major axis, which has typical values in the range of $\sim 0 - 15$ km/s (lower panel in Figure 34). The model with $\beta = 6$ would require a more extreme tangential anisotropy to reproduce the observed σ profile (green curve in the upper panel of Figure 34), but I do not go

further with this modeling here. MASSIVE galaxies observations usually report positive values of the Gauss-Hermite parameter h_4 in the outer galactic regions, which is indicative of radial anisotropy, for typical mass density profiles of early-type galaxies (Gerhard et al. 1998). Therefore, tangential anisotropy is unlikely to be extreme (Veale et al. 2018).

Early-type galaxies with rising σ profiles are in general characterised by a steep decline in the velocity dispersion within $\sim 0.5\,R_{\rm e}$, which can be reproduced by considering a diffuse dark matter halo ($\beta \sim 12$). This produces, in the modeling, a large $r_{\rm t}$ and then more extended dark matter haloes, with a consequent larger amount of dark matter. The $M_{\rm h}/M_*$ values, though, do not exceed what can be expected for massive early-type galaxies (Moster et al. 2010).

Figures 35 and 36 show the 2D maps of the velocity dispersion and velocity fields, respectively, for the model with $b = 1, \beta = 12, M_{\rm h}/M_* = 110$. As a comparison, Figure 37 shows the 2D map of $\sigma_{\rm los}$ in the presence of tangential anisotropy ($b = 0.8$), which determines steeper gradients in the $\sigma_{\rm los}$ field throughout the galaxy.

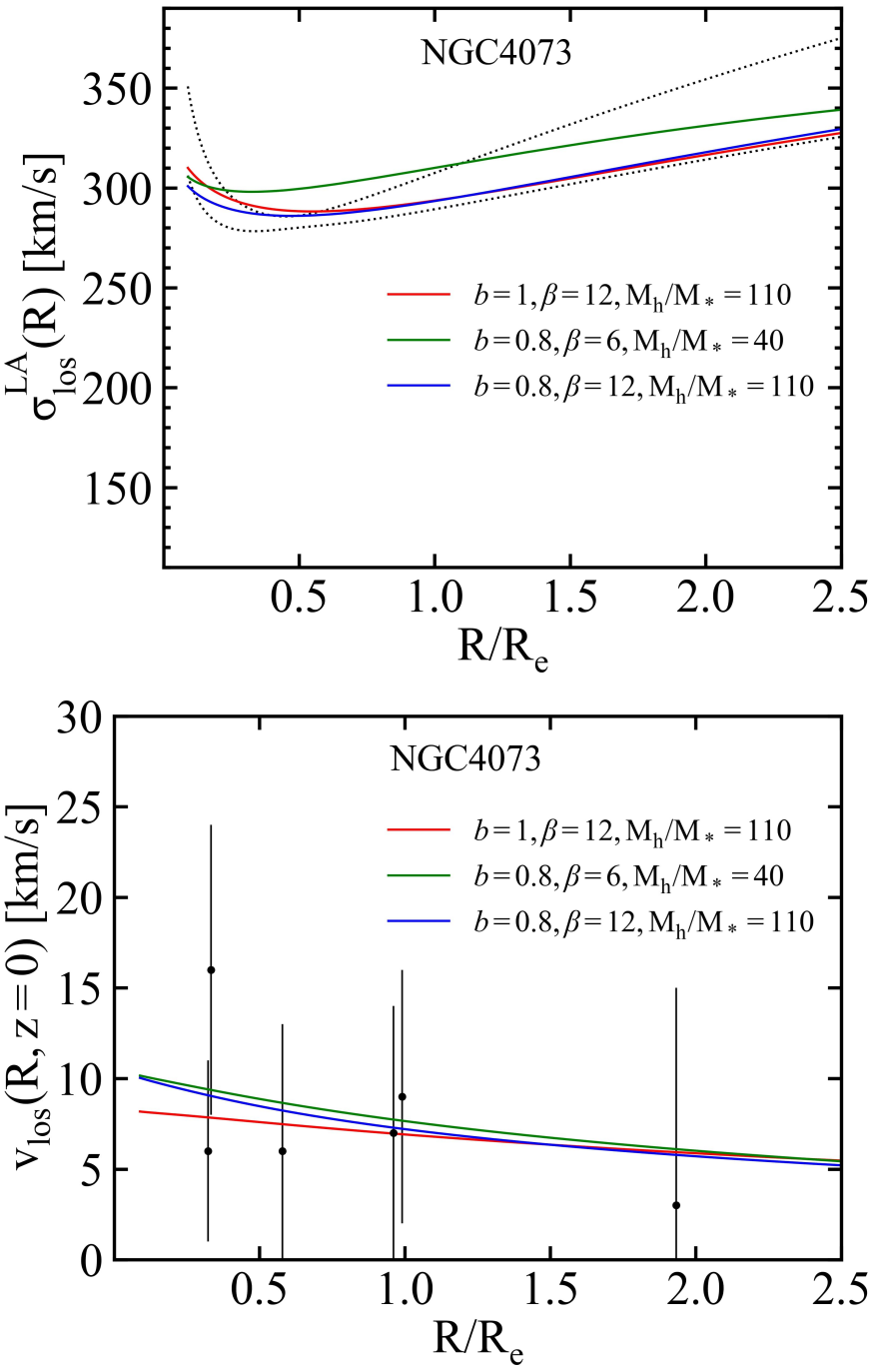

Figure 34: Velocity dispersion luminosity-weighted average $\sigma^{\rm LA}_{\rm los}(R)$ (upper panel) and line-of-sight velocity $v_{\rm los}$ along the major axis (lower panel) for NGC 4073. $k_0 = 0.05$ and $\xi_0 = 2\,R_{\rm e}$ for the model with $b = 1$ (red curve). $k_0 = 0.05$ and $\xi_0 = 1.5\,R_{\rm e}$ for the models with $b = 0.8$ (green and blue curves). In the upper panel, the dotted black curves define the confidence region given by $\sigma(R) \pm \Delta\sigma(R)$. In the lower panel, the black points with error bars correspond to the observed V along the major axis from Veale et al. (2016).

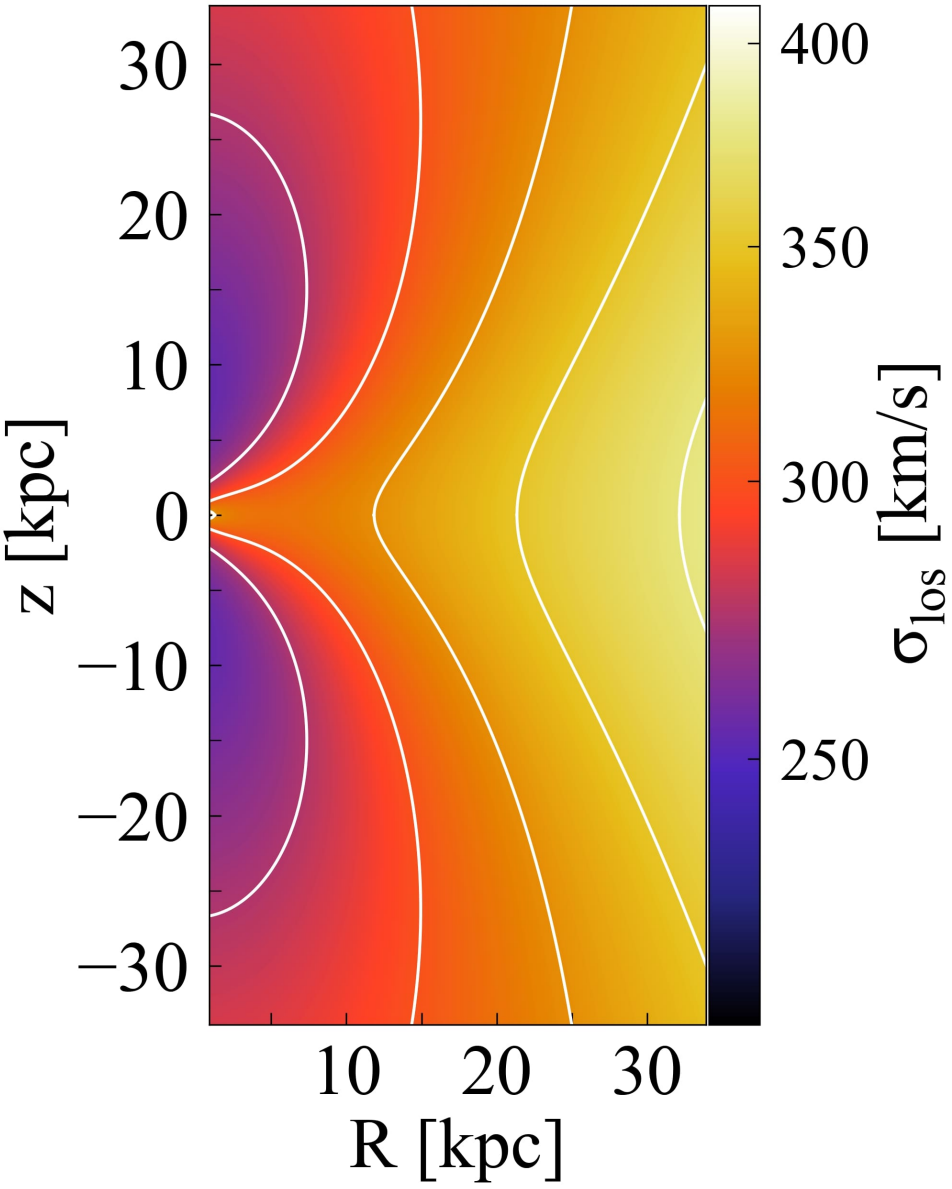

Figure 35: 2D map of the stellar velocity dispersion field $\sigma_{\rm los}$ for NGC 4073. The model considered is $M_* = 10^{11.91}\,{\rm M}_\odot, b = 1, \beta = 12, M_{\rm h}/M_* = 110$. White contours correspond to 275, 300, 325, 350 and 375 km/s.

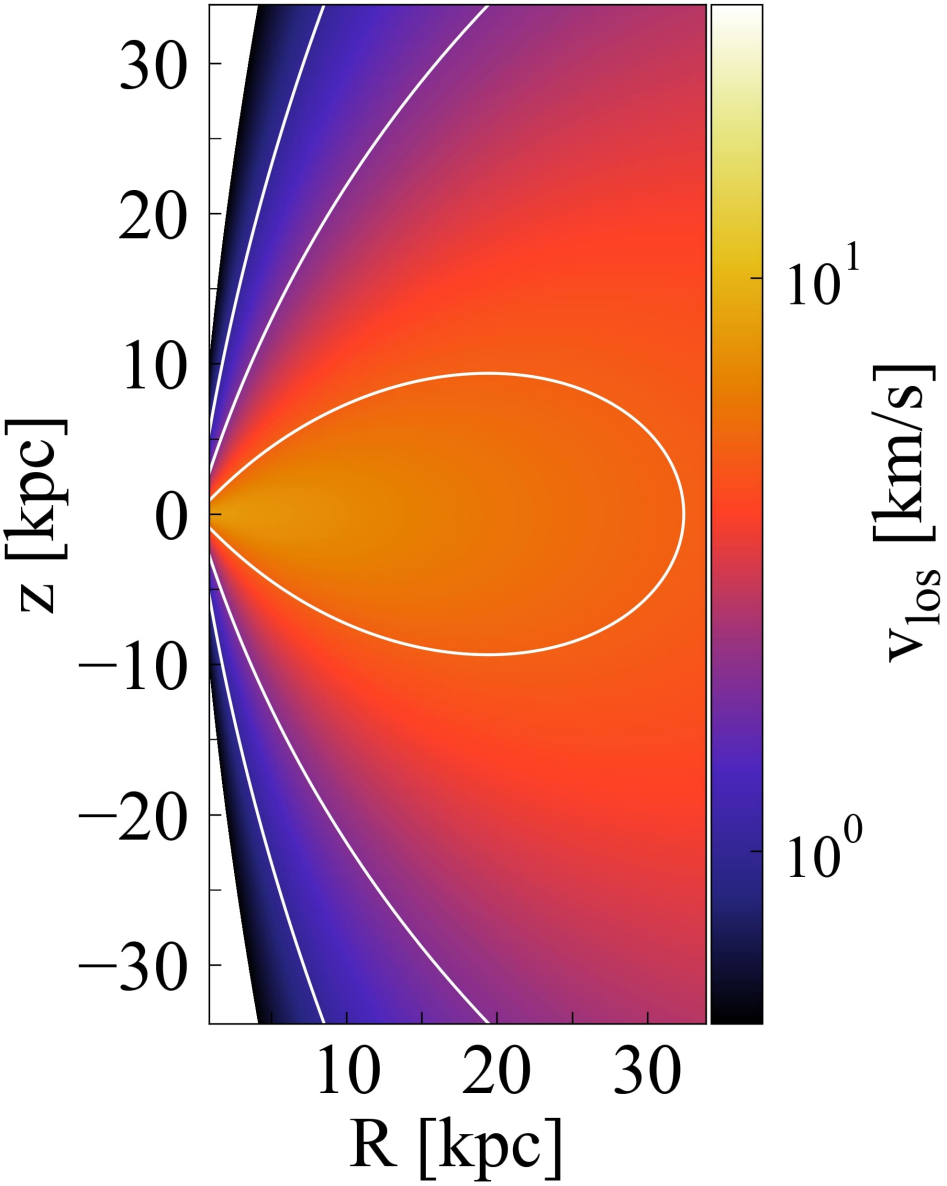

Figure 36: 2D map of the stellar velocity field $v_{\rm los}$ for NGC 4073. The model considered is $M_* = 10^{11.91}\,{\rm M}_\odot, b = 1, \beta = 12, M_{\rm h}/M_* = 110$. White contours correspond to 1, 2 and 5 km/s.

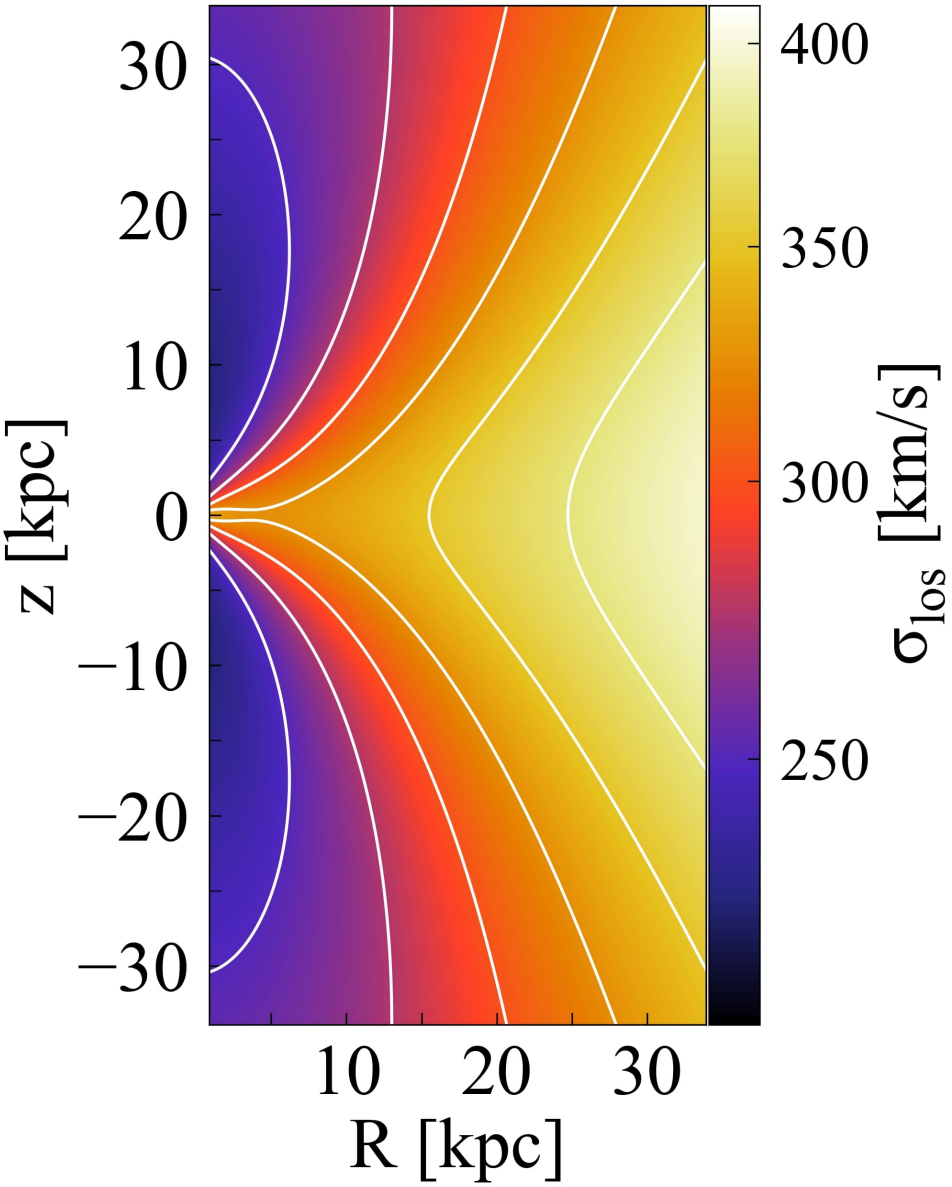

Figure 37: 2D map of the stellar velocity dispersion field $\sigma_{\rm los}$ for NGC 4073. The model considered is $M_* = 10^{11.91}\,{\rm M}_\odot, b = 0.8, \beta = 12, M_{\rm h}/M_* = 110$. White contours correspond to 250, 275, 300, 325, 350 and 375 km/s.

3.3.2 NGC 0383

NGC 0383 has a rising $\sigma(R)$ profile in the outer regions ($\gamma_{\rm outer} = 0.307$) and $\lambda_{\rm e} = 0.252$. From Table 1, its $R_{\rm e} = 7.1\,{\rm kpc}$. I consider $q = 1 - \varepsilon = 0.86$ and $b < 1.11$, from Equation (24). The stellar mass in Table 1 is $10^{11.82}\,{\rm M}_\odot$, but in the preliminary modeling I find $M_* = 10^{11.68}\,{\rm M}_\odot$ (1σ from Cappellari (2013) relation) more appropriate to reproduce the central velocity dispersion profile. For the isotropic case ($b = 1$), $k_0 = 0.95$ and $\xi_0 = 2\,R_{\rm e}$ reproduce the observed V profile along the major axis.

I first add a dark matter halo equal to the best model for the class of flat profiles, that has $\beta = 3$ and $M_{\rm h}/M_* = 15$; this is not appropriate to reproduce the observed σ, especially within $1.5\,R_{\rm e}$ (red curve in Figure 38). Recalling the procedure followed for NGC 4073, an increase of β to 6 produces an effect in the right direction (green curve in Figure 38), but an even more diffuse dark matter halo (with $\beta = 12$) is needed. Remarkably, also for this galaxy as for NGC 4073, I find a good result with the same $M_{\rm h}/M_* = 110$ ($f_{\rm DM} \sim 0.34$ within $R_{\rm e}$), even though $\sigma^{\rm LA}_{\rm los}$ is still not in the confidence region between $0.5\,R_{\rm e}$ and $1\,R_{\rm e}$ (blue curve in Figure 38). Note that the region bounded by $\sigma(R) \pm \Delta\sigma(R)$ is by definition narrower at $R = R_{\rm b} = 5\,{\rm kpc}$. From Figure 39, with this modeling dark matter starts to become relevant within $\sim 1\,R_{\rm e}$.

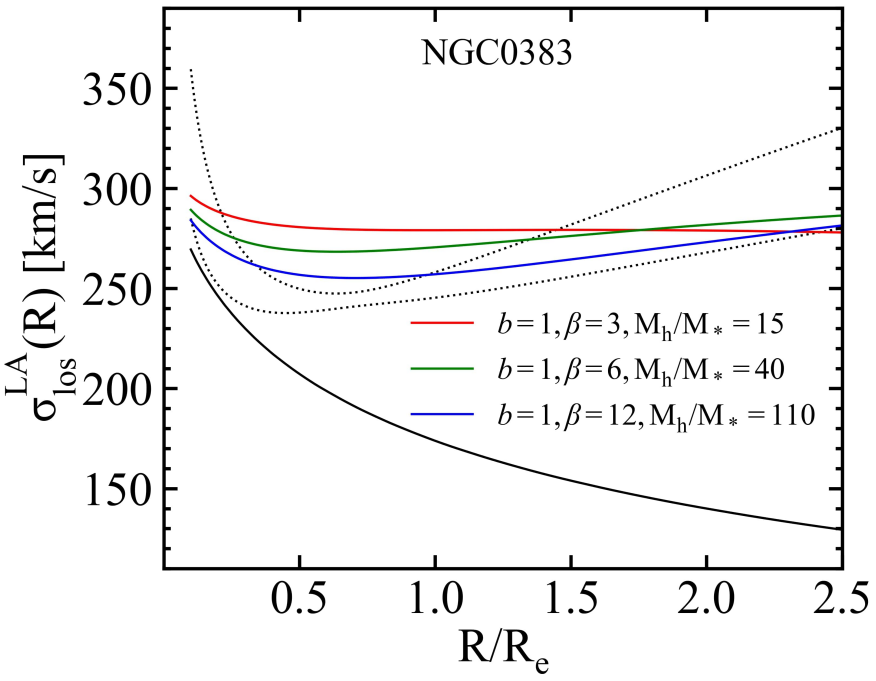

Figure 38: Velocity dispersion luminosity-weighted average $\sigma^{\rm LA}_{\rm los}(R)$ for NGC 0383. The models considered are: no dark matter (black), $\beta = 3, M_{\rm h}/M_* = 15$ (red), $\beta = 6, M_{\rm h}/M_* = 40$ (green) and $\beta = 12, M_{\rm h}/M_* = 110$ (blue). $b = 1$, $k_0 = 0.95$ and $\xi_0 = 2\,R_{\rm e}$ in all four models. The dotted black curves define the confidence region given by $\sigma(R) \pm \Delta\sigma(R)$.

I consider the case with tangential anisotropy by lowering b to 0.8 and using the previous values of $\beta = 12$ and $M_{\rm h}/M_* = 110$ (blue curve in the upper panel of 40). The observed σ in the inner regions is reproduced better with respect to the isotropic case (red line in the upper panel of 40). For the models with $b = 0.8$, $k_0 = 0.9$ and $\xi_0 = 1\,R_{\rm e}$ reproduce the observed V along the major axis, which has typical values in the range of $\sim 70 - 120$ km/s with a high statistical dispersion: I refer to the highest values of V (lower panel of Figure 40). The presence of tangential anisotropy, paired with a lower ξ_0, allows to reproduce the observed V better than in the isotropic case. A lower b determines a higher $v_{\rm los}$ (as described in Section 2.4) and allows to reproduce the observed values of V in the central regions ($\sim 100 - 120\,{\rm km/s}$).

As I find for NGC 4073, a diffuse dark matter halo ($\beta = 12$) and a high amount of dark matter ($M_{\rm h}/M_* > 100$) allow to reproduce the rising σ profile. Tangential anisotropy (if not too extreme) can be plausible, while radial anisotropy is not requested for galaxies with a velocity dispersion rise in the outer regions.

Figures 41 and 42 show the 2D maps of the velocity dispersion and velocity fields, respectively, for the model with $b = 1, \beta = 12, M_{\rm h}/M_* = 110$. As a comparison, Figure 43 shows the 2D map of $\sigma_{\rm los}$ in the presence of tangential anisotropy ($b = 0.8$).

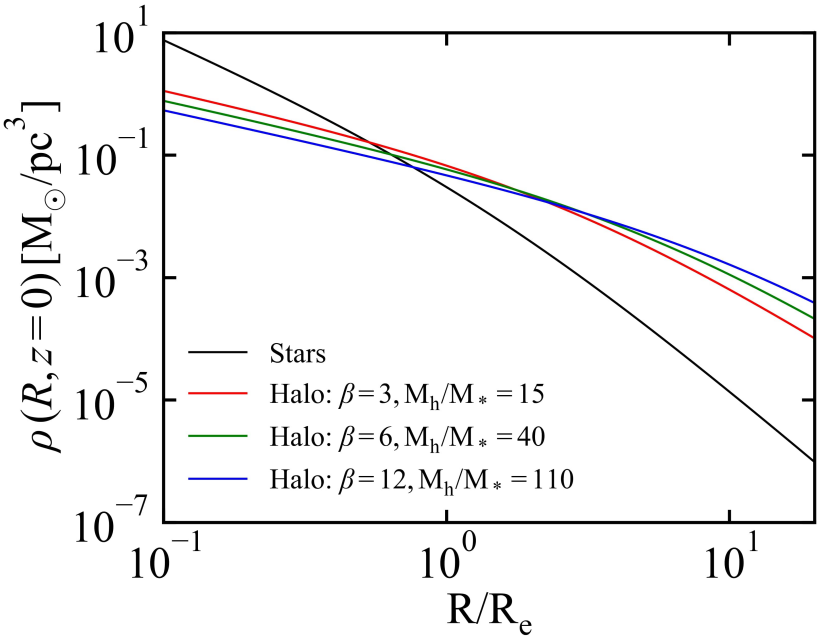

Figure 39: Density profiles for the models in Figure 38: stellar component along the major axis with $M_* = 10^{11.68}\,{\rm M}_\odot$ (black), halo component with $\beta = 3, M_{\rm h}/M_* = 15$ (red), $\beta = 6, M_{\rm h}/M_* = 40$ (green) and $\beta = 12, M_{\rm h}/M_* = 110$ (blue).

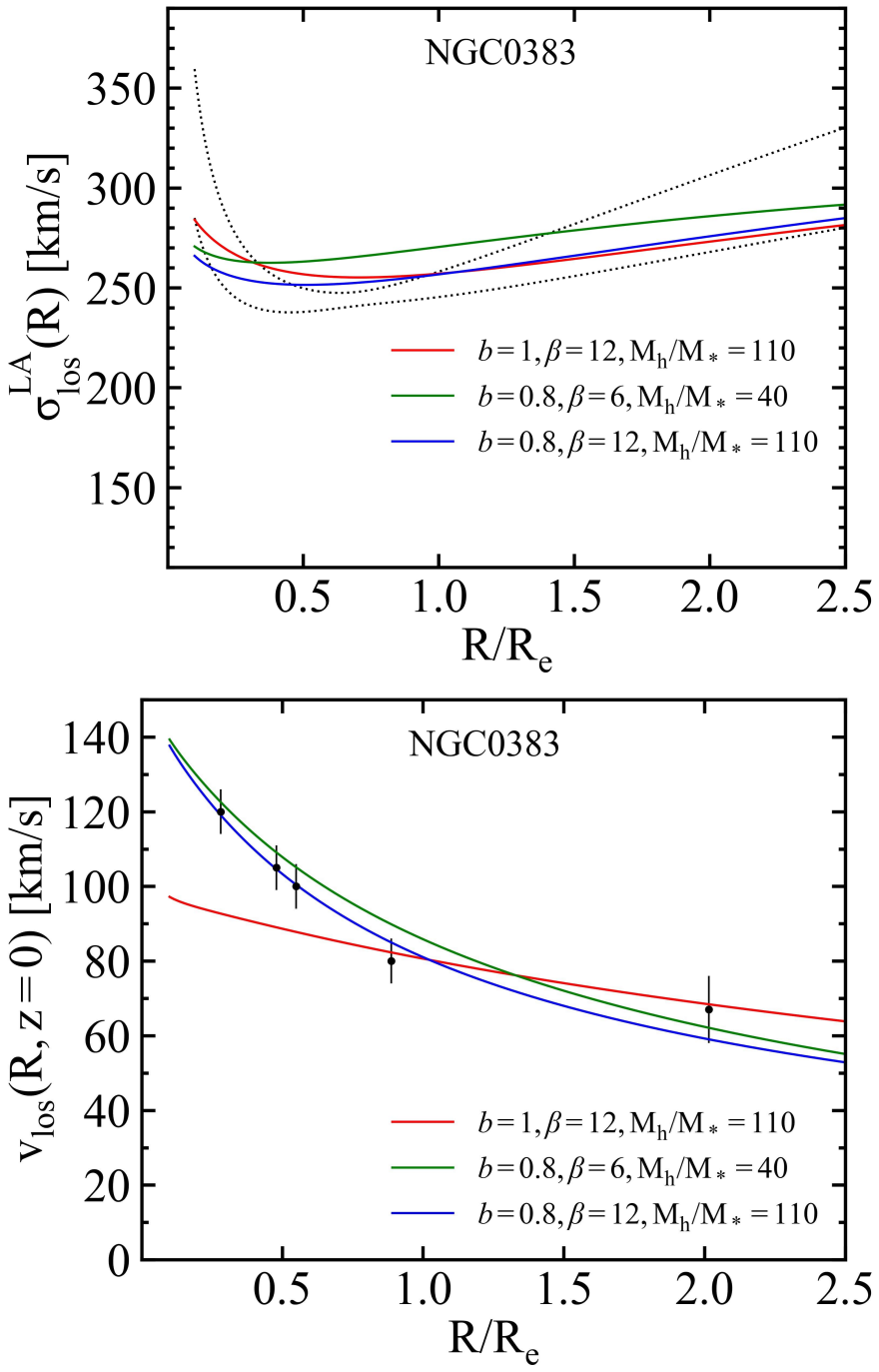

Figure 40: Velocity dispersion luminosity-weighted average $\sigma^{\rm LA}_{\rm los}(R)$ (upper panel) and line-of-sight velocity $v_{\rm los}$ along the major axis (lower panel) for NGC 0383. $k_0 = 0.95$ and $\xi_0 = 2\,R_{\rm e}$ for the model with $b = 1$ (red curve). $k_0 = 0.9$ and $\xi_0 = 1\,R_{\rm e}$ for the models with $b = 0.8$ (green and blue curves). In the upper panel, the dotted black curves define the confidence region given by $\sigma(R) \pm \Delta\sigma(R)$. In the lower panel, the black points with error bars correspond to the observed V along the major axis from Veale et al. (2016).

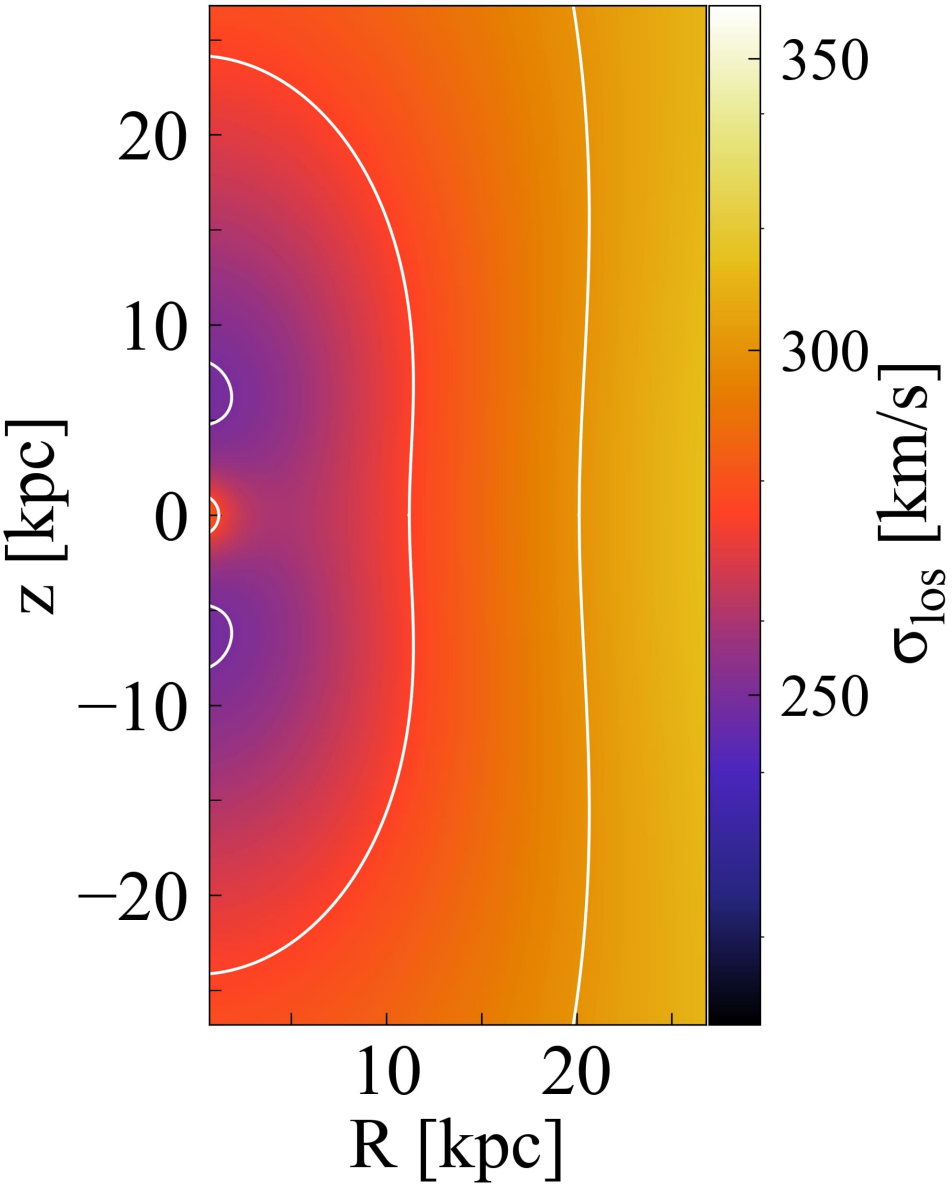

Figure 41: 2D map of the stellar velocity dispersion field $\sigma_{\rm los}$ for NGC 0383. The model considered is $M_* = 10^{11.68}\,{\rm M}_\odot, b = 1, \beta = 12, M_{\rm h}/M_* = 110$. White contours correspond to 250, 275, 300 and 325 km/s.

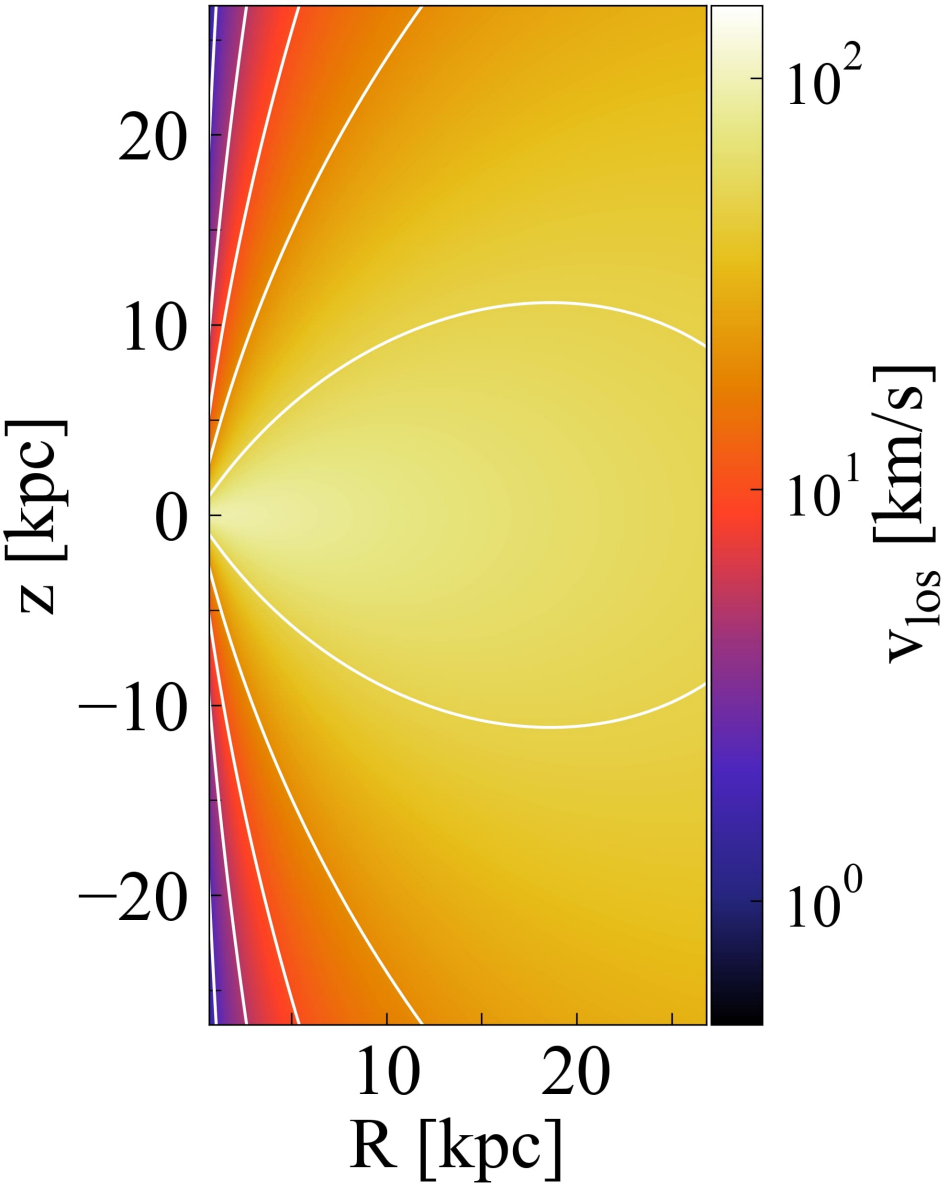

Figure 42: 2D map of the stellar velocity field $v_{\rm los}$ for NGC 0383. The model considered is $M_* = 10^{11.68}\,{\rm M}_\odot, b = 1, \beta = 12, M_{\rm h}/M_* = 110$. White contours correspond to 2, 5, 10, 20 and 50 km/s.

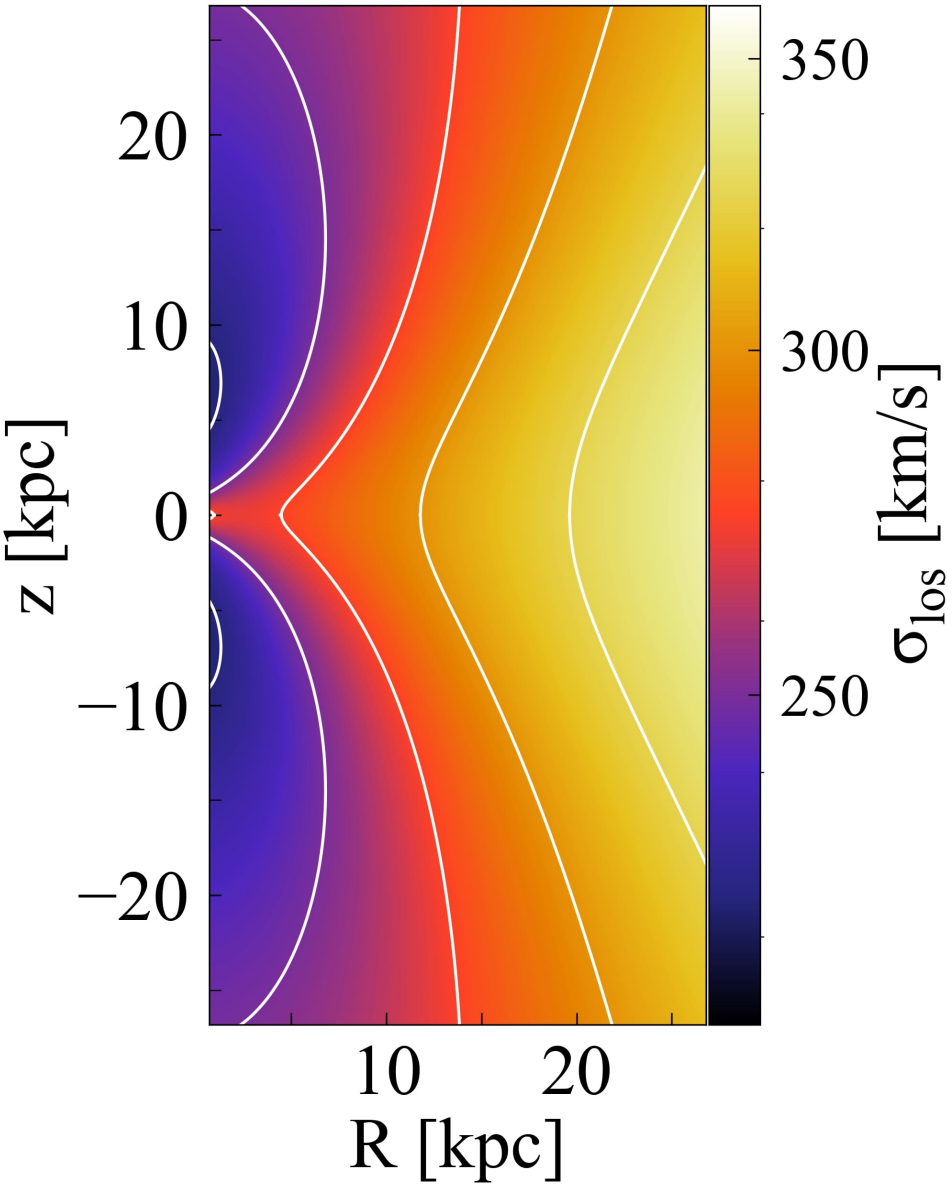

Figure 43: 2D map of the stellar velocity dispersion field $\sigma_{\rm los}$ for NGC 0383. The model considered is $M_* = 10^{11.68}\,{\rm M}_\odot, b = 0.8, \beta = 12, M_{\rm h}/M_* = 110$. White contours correspond to 225, 250, 275, 300 and 325 km/s.

4 Discussion and conclusions

In this work I modeled the internal structure (mass profile and orbital configuration) of six galaxies ($M_K < -25.8$) in the MASSIVE survey, representative of the three classes of observed outer shapes for the σ profiles. In particular, I focused on their velocity dispersion profiles in the outer regions: I compared the kinematics obtained from the Jeans equations ($\sigma_{\rm los}^{\rm LA}(R)$, and $v_{\rm los}(R)$ along the major axis) with the observed σ and $V(R)$ in Veale et al. (2016, 2018), and I derived constraints on the presence of dark matter and orbital anisotropy. This modeling leads to the following results:

- The stellar mass values estimated from M_K as in the commonly adopted relation of Cappellari (2013), distributed with a Jaffe profile, determine a $\sigma_{\rm los}^{\rm LA}(R)$ close to the observed $\sigma(R)$ in the inner regions. In particular, M_* is always equal or smaller than that resulting from the relation, but in any case within 2.6σ from it: NGC 0410, 4555, and 2340 are within $\sim 0-0.5\sigma$; NGC 3158, 4073, and 0383 are within $\sim 1-2\sigma$. This indicates that stellar mass largely dominates at the center.

- Dark matter is always needed to account for the observed $\sigma(R)$, even in the class of falling σ profiles. In this work the dark matter was modeled with a NFW profile of fixed concentration $c = 10$, and variable amount ($M_{\rm h}/M_*$) and scale-length ($\beta = r_{\rm h}/R_{\rm e}$). The modeling showed that the dark matter amount and distribution can be the same in ETGs with the same observed σ trend; in particular, this holds both for slow and fast rotators (Table 3). Isotropic models with $\beta \sim 3-6, M_{\rm h}/M_* \sim 2$ reproduce the falling σ profiles of both NGC 0410 and NGC 4555; isotropic models with $\beta \sim 3, M_{\rm h}/M_* \sim 10-15$ reproduce the flat profiles of NGC 2340 and NGC 3158; models with $\beta \sim 12, M_{\rm h}/M_* \sim 100$ reproduce the NGC 4073 and NGC 0383 observations.

- In galaxies with a falling σ profile (first row in Figure 44), radial anisotropy can be present, with the effect of making the outer σ falling faster. However, even when b is at its maximum (within the range found for fast rotators), the dark matter content remains low ($M_{\rm h}/M_* \sim 5$).

- A flat σ profile (second row in Figure 44) is produced by a halo with the same $\beta = 3$ obtained for falling profiles but the amount of dark matter must be larger ($M_{\rm h}/M_* \sim 10-15$). A β value larger than ~ 3 causes the $\sigma_{\rm los}^{\rm LA}$ profile to decline too much within $0.5\,R_{\rm e}$. Isotropic models with the previous properties can reproduce observations well; however, radial anisotropy can be present and, at its maximum value, corresponds to a dark matter amount only a bit larger ($M_{\rm h}/M_* \sim 15$).

- A rising σ profile (third row in Figure 44) requires a diffuse dark matter halo ($\beta \sim 12$) and a high amount of dark matter ($M_{\rm h}/M_* \sim 100$), in the isotropic case. Radial anisotropy is not requested, since a model with $b > 1$ would require an even higher $M_{\rm h}/M_*$ to reproduce the observations in the outer regions. Tangential anisotropy can be accomodated but it must still be paired with a high β and a high $M_{\rm h}/M_*$. If the good match with the inner observed $\sigma(R)$ is not required, then tangential anisotropy can allow for a reduction of β to 6 and $M_{\rm h}/M_*$ to 40.

Table 3. Properties of the galaxy models shown in the plots in Chapter 3 (the best model for each galaxy is highlighted)

Galaxy	$\log_{10}M_*$ ($M_\odot$)	b	k_0	ξ_0 ($R_{\rm e}$)	β	$M_{\rm h}/M_*$	$f_{\rm DM}(R_{\rm e})$	$f_{\rm DM}(5\,R_{\rm e})$
(1)	(2)	(3)	(4)	(5)	(6)	(7)	(8)	(9)
NGC 0410	11.79	1	0.1	2	3	2	0.11	0.37
NGC 0410	11.79	1	0.1	2	6	5	0.08	0.39
NGC 0410	11.79	1.2	0.2	1.5	3	2	0.11	0.37
NGC 0410	11.79	1.2	0.2	1.5	6	5	0.08	0.39
NGC 4555	11.86	1	0.65	1.5	3	2	0.11	0.37
NGC 4555	11.86	1	0.65	1.5	6	5	0.08	0.39
NGC 4555	11.86	1.1	1	1	3	2	0.11	0.37
NGC 4555	11.86	1.1	1	1	6	5	0.08	0.39
NGC 2340	11.86	1	0.05	2	3	10	0.39	0.75
NGC 2340	11.86	1	0.05	2	6	30	0.37	0.79
NGC 2340	11.79	1.4	0.1	1	3	14	0.47	0.81
NGC 2340	11.79	1.4	0.1	1	6	40	0.44	0.84
NGC 3158	11.74	1	0.95	2	3	15	0.48	0.81
NGC 3158	11.74	1	0.95	2	6	40	0.42	0.83
NGC 3158	11.74	1.1	1	2.5	3	15	0.48	0.81
NGC 3158	11.74	1.1	1	2.5	6	40	0.42	0.83
NGC 4073	11.91	1	0.05	2	6	40	0.42	0.83
NGC 4073	11.91	1	0.05	2	12	110	0.36	0.83
NGC 4073	11.91	0.8	0.05	1.5	6	40	0.42	0.83
NGC 4073	11.91	0.8	0.05	1.5	12	110	0.36	0.83
NGC 0383	11.68	1	0.95	2	6	40	0.41	0.83
NGC 0383	11.68	1	0.95	2	12	110	0.34	0.83
NGC 0383	11.68	0.8	0.9	1	6	40	0.41	0.83
NGC 0383	11.68	0.8	0.9	1	12	110	0.34	0.83

Table 3: Columns are (1) Galaxy name. (2) Total stellar mass. (3) Anisotropy parameter $b = \sigma_R^2/\sigma_z^2$. (4) Central value of $k(r)$ in Equation (29). (5) Scale radius of $k(r)$ in units of $R_{\rm e}$. (6) Ratio between $r_{\rm h}$ and $R_{\rm e}$. (7) Total halo mass M_h in units of total stellar mass M_*. (8) Dark matter fraction within $R_{\rm e}$. (9) Dark matter fraction within $5\,R_{\rm e}$.

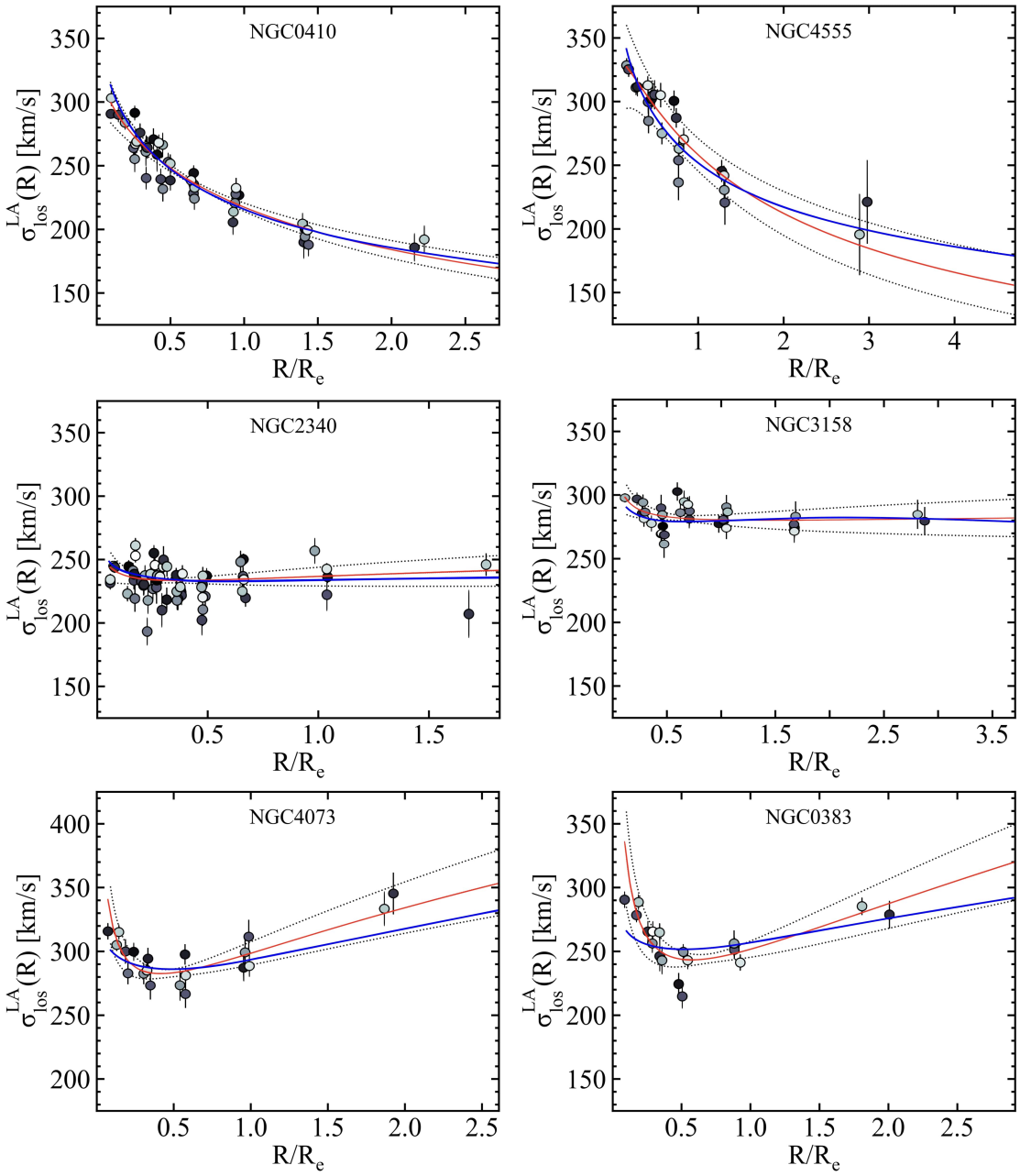

Figure 44: Comparison between the observed velocity dispersion profiles (Veale et al. 2018) and those resulting from the models highlighted in Table 3 (shown in blue). Points with error bars indicate the observed σ, with colour corresponding to the angular location of the taken spectrum at radius R: black and white points correspond to positive and negative major semi-axis respectively, and grey points correspond to positions near the minor axis. Double power-law fits $\sigma(R)$ are shown in red. The dotted black curves define the confidence region given by $\sigma(R) \pm \Delta\sigma(R)$, where $\Delta\sigma(R)$ is derived as described in Section 1.4.

- This work suggests a trend of the dark matter amount and distribution with the shape of the velocity dispersion profiles in the outer regions. From falling to rising σ profiles, thus at the increase of $\gamma_{\rm outer}$, $M_{\rm h}/M_*$ increases from ~ 2 to ~ 100. β is large (~ 12) for galaxies with rising σ profiles, and equally low (~ 3) for galaxies with falling and flat σ profiles. Figure 45 shows the ratio $M_{\rm h}/M_*$ as a function of $r/R_{\rm e}$. Galaxies with a rising σ profile have the highest $M_{\rm h}(r)/M_*(r)$ in the outer regions: this is due to the high β (~ 12) and the high $M_{\rm h}$ compared to that found for galaxies with falling and flat σ profiles.

- Orbital anisotropy alone cannot account for the different observed velocity dispersion profiles and has a minor effect compared to variations in the mass profile. A trend in the orbital configuration can help reproducing the trend in the observed $\sigma(R)$, but the key ingredient in shaping velocity dispersion in the outer regions seems to be the dark matter halo (Table 3). Isotropic models ($b = 1$), if paired with appropriate values of β and $M_{\rm h}/M_*$, can in general reproduce the observed $\sigma(R)$.

- Galaxies with similar M_* ($\sim 10^{11.7} - 10^{11.9}\,{\rm M}_\odot$) can present different velocity dispersion profiles, from falling to rising (left panel in Figure 46), and these can be reproduced by varying $M_{\rm h}/M_*$ by a large factor. Therefore, different σ profiles seem to correspond to a variation in $M_{\rm h}$ at similar M_*.

- The central and right panels in Figure 46 show the outer slope $\gamma_{\rm outer}$ versus the dark matter fraction $f_{\rm DM}$ within 1 and 5 $R_{\rm e}$, respectively. Note again the suggested trend for the dark matter distribution: $f_{\rm DM}$ within 1 and 5 $R_{\rm e}$ is higher for galaxies with flat or rising σ profiles. In particular, from the modeling $f_{\rm DM} \sim 0.1$ within $R_{\rm e}$ and < 0.4 within $5\,R_{\rm e}$ for galaxies with falling σ profiles. $f_{\rm DM}$ is instead $\sim 0.3-0.5$ within $R_{\rm e}$ and $\sim 0.7-0.8$ within $5\,R_{\rm e}$ for galaxies with flat or rising σ profiles. These values are consistent with those found previously in a number of studies based on modeling of the observed stellar kinematics and of gravitational lensing effects (Gerhard et al. 2001; Treu and Koopmans 2004; Thomas et al. 2005; Cappellari 2016; Smith, Lucey, and Edge 2017; Alabi et al. 2017; Santucci et al. 2022).

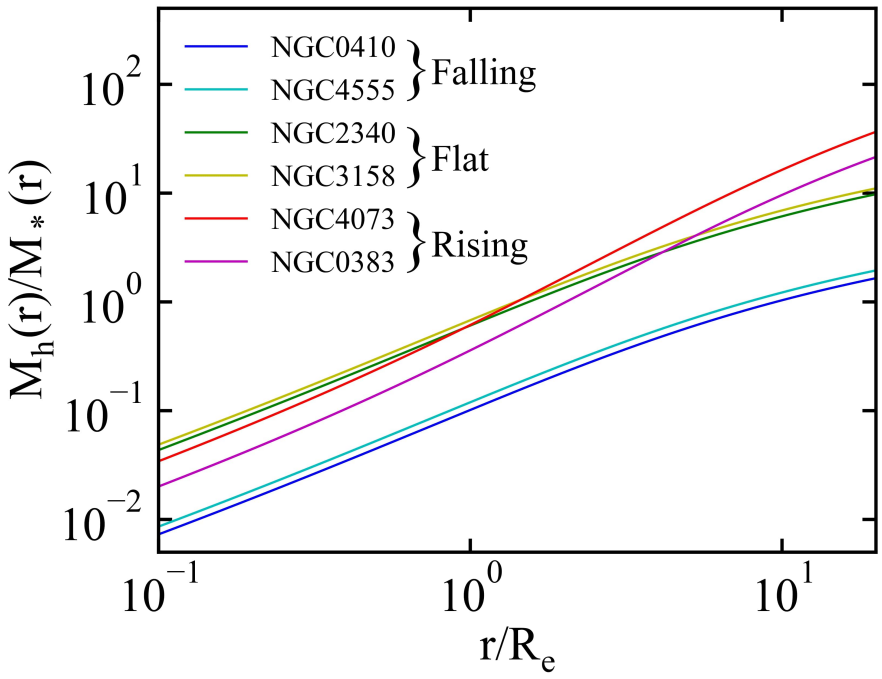

Figure 45: Ratio of the dark matter mass to the stellar mass within a radius r from the modeling of the six MASSIVE galaxies studied in this work. The models considered are those highlighted in Table 3.

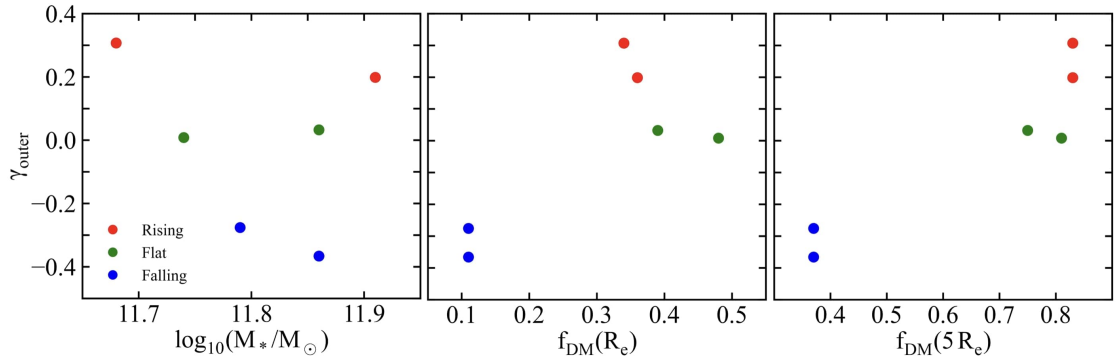

Figure 46: Outer slope $\gamma_{\rm outer}$ versus stellar mass M_* (left panel), $f_{\rm DM}$ within $R_{\rm e}$ (central panel) and $f_{\rm DM}$ within $5\,R_{\rm e}$ (right panel) from the modeling of the six MASSIVE galaxies studied in this work. Velocity dispersion trends are highlighted: rising (red), flat (green) and falling (blue). The models considered are those highlighted in Table 3.

4.1 Limits of the present work and future developments

In this section I briefly recall and discuss some of the limits of the present work and possible improvements:

- I considered an axisymmetric stellar distribution but, as reported in Ene et al. (2018), massive early-type galaxies can be mildly triaxial. Also, the stellar density profile could be steeper or shallower compared to the Jaffe profile.

- An additional dark matter component, more diffuse than the NFW halo, could help reproducing better the rising $\sigma(R)$ observed in NGC 4073 and NGC 0383 (third row in Figure 44). Also, the halo density profile could be different from the NFW profile (e.g. not spherical).

- I modeled the orbital anisotropy as spatially constant throughout the galaxy. Since galaxy formation mechanisms are thought to determine a larger radial anisotropy in the outer regions of the galaxy and positive h_4 gradients are found in Veale et al. (2018), in a more realistic modeling $b \sim 1$ in the inner regions, and it should increase with R. This improvement is not expected to affect the previous conclusions, though.

- Another limitation is that currently the JASMINE code computes the kinematic quantities only for face-on (FO) and edge-on (EO) views. Since the inclination angles of the MASSIVE early-type galaxies are not known, I assumed an EO view. If the inclination angle were instead lower, then the intrinsic axes ratio q would be lower, and the $R_{\rm e}$ for an EO view would be different. A code projecting the kinematic fields at different i would allow to use different combinations of q and $R_{\rm e}$ and then perform a more general investigation, obtaining more general results.

A Numerical grid

The JASMINE code works on three axisymmetric grids in (R, z): a principal grid, on which all quantities are computed, and two secondary grids, staggered in R and z respectively, that serve to compute the derivatives of the potentials (forces) with the centred finite-differences method of approximation.

In the original version of JASMINE (Posacki, Pellegrini, and Ciotti 2013), the physical extent of the numerical grid was proportional to the effective radius considered for the model. In this way, galaxy models with different $R_{\rm e}$ would be computed on grids with different extent and resolution. Differently from this approach, I consider a fixed numerical grid for all models, with R going from 0 to $R_{\rm grid} = 500\,{\rm kpc}$ and z going from $-z_{\rm grid}$ to $z_{\rm grid} = 500\,{\rm kpc}$. For each model $i_{\rm max} = 250$ and $j_{\rm max} = 2\,i_{\rm max} - 1 = 499$ are the number of grid points in R and z, respectively, so that the resolution is always the same and I can compare models on an equal footing. The grid is logarithmic so that there is a higher resolution at the centre of the galaxy and near its equatorial plane. In particular, the spacings dR and dz between grid points are defined as:

$$dR = dz = \frac{R_{\rm ratio} - 1}{R_{\rm ratio}^{i_{\rm max}} - 1}\, R_{\rm ratio}^{i-1}\, R_{\rm grid}, \tag{A1}$$

where $R_{\rm ratio} = 1.029$ and i goes from 1 to $i_{\rm max}$. Therefore, the resolution at the centre of the galaxy ($i = 1$) and near its equatorial plane is:

$$(dR)_{\rm min} = \frac{R_{\rm ratio} - 1}{R_{\rm ratio}^{i_{\rm max}} - 1} R_{\rm grid} \sim 2.29 \cdot 10^{-5}\, R_{\rm grid} \sim 11\,{\rm pc} \tag{A2}$$

The number of grid points in R and z significantly influences the time requested from the code to compute the outputs. Having $i_{\rm max} = 250$ and $i_{\rm max} = 499$ allows to have both a good spatial resolution and a computational time of less than two hours for the Potential solver (described at the beginning of Section 2).

B Projections

After solving the Jeans equations for the multicomponent gravitational potential (supermassive black hole, stars and dark matter halo) and deriving $\overline{v_\varphi}$ as described in Section 2.4, the JASMINE code projects the kinematic fields, together with the stellar density, for both edge-on (EO) and face-on (FO) views. The projection of ρ_* gives the surface mass density Σ_*, while $\overline{v_\varphi}$, σ_R, σ_φ and Δ are used to derive $v_{\rm los}(R,z)$ and $\sigma_{\rm los}(R,z)$, the l.o.s. velocity and velocity dispersion fields.

I recall here the projections along a general line of sight (l.o.s.) direction $\boldsymbol{n}$ of the stellar density ρ_*, streaming velocity $\boldsymbol{v}$ and velocity dispersion tensor $\boldsymbol{\sigma}^2$, which are respectively defined as

$$\Sigma_* = \int_{-\infty}^{+\infty} \rho_*\, dl \tag{B1}$$

$$\Sigma_* v_{\rm los} = \int_{-\infty}^{+\infty} \rho_* \langle \boldsymbol{v}, \boldsymbol{n}\rangle\, dl \tag{B2}$$

$$\Sigma_* \sigma_{\rm P}^2 = \int_{-\infty}^{+\infty} \rho_* \langle \boldsymbol{\sigma}^2 \boldsymbol{n}, \boldsymbol{n}\rangle\, dl, \tag{B3}$$

where Σ_* is the surface stellar density (Posacki, Pellegrini, and Ciotti 2013). In a general case (l.o.s. inclination angle $i > 0$), if rotational support is present (Satoh's parameter $k > 0$) then $\sigma_{\rm P}^2$ is not the observed velocity dispersion $\sigma_{\rm los}^2$, given instead by

$$\sigma_{\rm los}^2 = \sigma_{\rm P}^2 + V_{\rm P}^2 - v_{\rm los}^2, \tag{B4}$$

where $V_{\rm P}^2$ is the projection of $\langle \boldsymbol{n}, \boldsymbol{v}\rangle^2$. Given this, the EO projections are

$$\Sigma_*(R,z) = 2\int_R^\infty \frac{\rho_*\, \tilde{R}\, d\tilde{R}}{\sqrt{\tilde{R}^2 - R^2}} \tag{B5}$$

$$\Sigma_* v_{\rm los}(R,z) = 2R\int_R^\infty \frac{\rho_*\, \overline{v_\varphi}\, d\tilde{R}}{\sqrt{\tilde{R}^2 - R^2}} \tag{B6}$$

$$\Sigma_* v_{\rm P}^2(R,z) = 2R^2\int_R^\infty \frac{\rho_*\, \overline{v_\varphi}^2\, d\tilde{R}}{\tilde{R}\sqrt{\tilde{R}^2 - R^2}} \tag{B7}$$

$$\Sigma_* \sigma_{\rm P}^2(R,z) = 2\int_R^\infty \left[\left(\tilde{R}^2 - R^2\right)\sigma_R^2 + R^2\sigma_\varphi^2\right] \frac{\rho_*\, d\tilde{R}}{\tilde{R}\sqrt{\tilde{R}^2 - R^2}}, \tag{B8}$$

where all integrations are performed at fixed z. Note that $\Sigma_*\sigma_{\rm P}^2$ can be split into two parts as

$$\Sigma_* \sigma_{\rm P}^2 = 2 \int_R^\infty \frac{\rho_* \, \sigma_R^2 \, \tilde{R} \, d\tilde{R}}{\sqrt{\tilde{R}^2 - R^2}} + 2R^2 \int_R^\infty (1 - k^2) \frac{\rho_* \, \Delta \, d\tilde{R}}{\tilde{R} \sqrt{\tilde{R}^2 - R^2}}, \tag{B9}$$

where the former is independent from k and the latter is modulated by $(1 - k^2)$. The FO projections are instead

$$\Sigma_*(R, z) = 2 \int_0^\infty \rho_* \, dz \tag{B10}$$

$$\Sigma_* \sigma_{\rm P}^2(R, z) = 2 \int_0^\infty \rho_* \, \sigma_z^2 \, dz. \tag{B11}$$

For a face-on view ($i = 0$), $\sigma_{\rm los}^2 = \sigma_{\rm P}^2$ and $v_{\rm los} = 0$, since there are no ordered motions along the z axis, by model assumption.

Once the kinematic projections are computed by JASMINE, the `Python 3` code that I developed receives them in input (as HDF5 files) and computes the luminosity-weighted average $\sigma_{\rm los}^{\rm LA}(R)$ for each radius R:

$$\sigma_{\rm los}^{\rm LA}(R) = \left[\frac{\int_R^{R+\Delta R} \Sigma_* \, \sigma_{\rm los}^2 \, R \, dR}{\int_R^{R+\Delta R} \Sigma_* \, R \, dR} \right]^{1/2}. \tag{B12}$$

Bibliography

Alabi, A. B. et al. (2017). "The SLUGGS survey: dark matter fractions at large radii and assembly epochs of early-type galaxies from globular cluster kinematics". In: *Monthly Notices of the Royal Astronomical Society* **468**, 3949.

Arnold, J. A. et al. (2014). "The SLUGGS survey: wide-field stellar kinematics of early-type galaxies". In: *The Astrophysical Journal* **791**, 80.

Binney, J. and S. Tremaine (1987). *Galactic Dynamics*. Princeton University Press.

Brodie, J. P. et al. (2014). "The SAGES Legacy Unifying Globulars and Galaxies Surveys (SLUGGS): sample definition, methods, and initial results". In: *The Astrophysical Journal* **796**, 52.

Cappellari, M. (2008). "Measuring the inclination and mass-to-light ratio of axisymmetric galaxies via anisotropic Jeans models of stellar kinematics". In: *Monthly Notices of the Royal Astronomical Society* **390**, 71.

— (2013). "Effect of environment on galaxies' mass-size distribution: unveiling the transition from outside-in to inside-out evolution". In: *The Astrophysical Journal Letters* **778**, L2.

— (2016). "Structure & kinematics of early-type galaxies from integral-field spectroscopy". In: *Annual Review of Astronomy and Astrophysics* **54**, 597.

Cappellari, M. and E. Emsellem (2004). "Parametric recovery of line-of-sight velocity distributions from absorption-line spectra of galaxies via penalized likelihood". In: *The Astronomical Society of the Pacific* **116**, 138.

Cappellari, M. et al. (2007). "The SAURON project - X. The orbital anisotropy of elliptical and lenticular galaxies: revisiting the $(V/\sigma, \varepsilon)$ diagram with integral-field stellar kinematics". In: *Monthly Notices of the Royal Astronomical Society* **379**, 418.

— (2013). "The ATLAS^{3D} project - XV. Benchmark for early-type galaxies scaling relations from 260 dynamical models: mass-to-light ratio, dark matter, Fundamental Plane and Mass Plane". In: *Monthly Notices of the Royal Astronomical Society* **432**, 1709.

Caravita, C., L. Ciotti, and S. Pellegrini (2021). "Jeans modelling of axisymmetric galaxies with multiple stellar populations". In: *Monthly Notices of the Royal Astronomical Society* **506**, 1480.

Carter, D., T. J. Bridges, and G. K. T. Hau (1999). "Kinematics, abundaces and origin of brightest cluster galaxies". In: *Monthly Notices of the Royal Astronomical Society* **307**, 131.

Crook, A. C. et al. (2007). "Groups of galaxies in the Two Micron All Sky Redshift Survey". In: *The Astrophysical Journal* **655**, 790.

— (2008). "Erratum: "groups of galaxies in the Two Micron All Sky Redshift Survey" (Apj, 655, 790 [2007])". In: *The Astrophysical Journal* **685**, 1320.

Davies, R. L. and G. Illingworth (1983). "Dynamics of yet more ellipticals and bulges". In: *The Astrophysical Journal* **266**, 516.

Davis, T. A. et al. (2016). "The MASSIVE survey - III. Molecular gas and a broken Tully-Fisher relation in the most massive early-type galaxies". In: *Monthly Notices of the Royal Astronomical Society* **455**, 214.
— (2019). "The MASSIVE survey – XI. What drives the molecular gas properties of early-type galaxies". In: *Monthly Notices of the Royal Astronomical Society* **486**, 1404.
Dutton, A. A. and A. V. Macciò (2014). "Cold dark matter haloes in the Planck era: evolution of structural parameters for Einasto and NFW profiles". In: *Monthly Notices of the Royal Astronomical Society* **441**, 3359.
Emsellem, E. et al. (2007). "The SAURON project - IX. A kinematic classification for early-type galaxies". In: *Monthly Notices of the Royal Astronomical Society* **379**, 401.
— (2011). "The ATLAS^{3D} project - III. A census of the stellar angular momentum within the effective radius of early-type galaxies: unveiling the distribution of fast and slow rotators". In: *Monthly Notices of the Royal Astronomical Society* **414**, 888.
Ene, I. et al. (2018). "The MASSIVE survey - X. Misalignment between kinematic and photometric axes and intrinsic shape of massive early-type galaxies". In: *Monthly Notices of the Royal Astronomical Society* **479**, 2810.
— (2019). "The MASSIVE survey XIII – Spatially resolved stellar kinematics in the central 1 kpc of 20 massive elliptical galaxies with the GMOS-North integral-field spectrograph". In: *The Astrophysical Journal* **878**, 57.
— (2020). "The MASSIVE survey XIV - Stellar velocity profiles and kinematic misalignments from 200 pc to 20 kpc in massive early-type galaxies". In: *The Astrophysical Journal* **891**, 65.
Franx, M., G. Illingworth, and T. Heckman (1989). "Major and minor axis kinematics of 22 ellipticals". In: *The Astrophysical Journal* **344**, 613.
Gerhard, O. et al. (1998). "Breaking the degeneracy between anisotropy and mass: the dark halo of the E0 galaxy NGC 6703". In: *Monthly Notices of the Royal Astronomical Society* **295**, 197.
— (2001). "Dynamical family properties and dark halo scaling relations of giant elliptical galaxies". In: *The Astronomical Journal* **121**, 1936.
Goulding, A. D. et al. (2016). "The MASSIVE survey. IV. The X-ray halos of the most massive early-type galaxies in the nearby universe". In: *The Astrophysical Journal* **826**, 167.
Goullaud, C. F. et al. (2018). "The MASSIVE survey. IX. Photometric analysis of 35 high-mass early-type galaxies with HST WFC3/IR". In: *The Astrophysical Journal* **856**, 11.
Greene, J. E. et al. (2015). "The MASSIVE survey. II. Stellar population trends out to large radius in massive early-type galaxies". In: *The Astrophysical Journal* **807**, 11.
— (2019). "The MASSIVE survey. XII. Connecting stellar populations of early-type galaxies to kinematics and environment". In: *The Astrophysical Journal* **874**, 66.

Gu, M. et al. (2022). "The MASSIVE survey. XVI. The stellar initial mass function in the center of MASSIVE early-type galaxies". In: *The Astrophysical Journal* **932**, 103.

Jaffe, W. (1983). "A simple model for the distribution of light in spherical galaxies". In: *Monthly Notices of the Royal Astronomical Society* **202**, 995.

Lanzoni, B. and L. Ciotti (2003). "Projection effects on the FP thickness". In: *Astronomy and Astrophysics* **404**, 819.

Lovell, M. R. et al. (2018). "The fraction of dark matter within galaxies from the IllustrisTNG simulations". In: *Monthly Notices of the Royal Astronomical Society* **481**, 1950.

Ma, C.-P. et al. (2014). "The MASSIVE survey. I. A volume-limited integral-field spectroscopic study of the most massive early-type galaxies within 108 Mpc". In: *The Astrophysical Journal* **795**, 158.

McConnell, N. J. and C.-P. Ma (2013). "Revisiting the scaling relations of black hole masses and host galaxy properties". In: *The Astrophysical Journal* **764**, 184.

Moster, B. P. et al. (2010). "Constraints on the relationship between stellar mass and halo mass at low and high redshift". In: *The Astrophysical Journal* **710**, 903.

Murphy, J. D., K. Gebhardt, and M. Cradit (2014). "The rising stellar velocity dispersion of M87 from integrated starlight". In: *The Astrophysical Journal* **785**, 143.

Murphy, J. D. et al. (2011). "Galaxy kinematics with VIRUS-P: the dark matter halo of M87". In: *The Astrophysical Journal* **729**, 129.

Naab, T. et al. (2014). "The ATLAS^{3D} project: XXV. Two-dimensional kinematic analysis of simulated galaxies and the cosmological origin of fast and slow rotators". In: *Monthly Notices of the Royal Astronomical Society* **444**, 3357.

Navarro, J. F., C. S. Frenk, and S. D. M. White (1997). "A universal density profile from hierarchical clustering". In: *The Astrophysical Journal* **490**, 493.

Negri, A., L. Ciotti, and S. Pellegrini (2014). "The effects of stellar dynamics on the X-ray emission of flat early-type galaxies". In: *Monthly Notices of the Royal Astronomical Society* **439**, 823.

Newman, A. B. et al. (2013). "The density profiles of massive, relaxed galaxy clusters. I. The total density over three decades in radius". In: *The Astrophysical Journal* **765**, 24.

Pandya, V. et al. (2017). "The MASSIVE survey. VI. The spatial distribution and kinematics of warm ionized gas in the most massive local early-type galaxies". In: *The Astrophysical Journal* **837**, 40.

Posacki, S., S. Pellegrini, and L. Ciotti (2013). "The effects of galaxy shape and rotation on the X-ray haloes of early-type galaxies". In: *Monthly Notices of the Royal Astronomical Society* **000**, 1.

Richtler, T. et al. (2011). "The dark halo of the Hydra I galaxy cluster: core, cusp, cosmological? Dynamics of NGC 3311 and its globular cluster system". In: *Astronomy & Astrophysics* **531**, A119.

Richtler, T. et al. (2014). "The globular cluster system of NGC 1316. III. Kinematic complexity". In: *Astronomy & Astrophysics* **569**, A41.

Santucci, G. et al. (2022). "The SAMI galaxy survey: the internal orbital structure and mass distribution of passive galaxies from triaxial orbit super-position Schwarzschild models". In: *The Astrophysical Journal* **930**, 153.

Satoh, C. (1980). "Dynamical models of axisymmetric galaxies and their application of the elliptical galaxy NGC 4697". In: *Publications of the Astronomical Society of Japan* **32**, 41.

Schauer, A. T. P. et al. (2014). "The mystery of the σ-bump - A new signature for major mergers in early-type galaxies?" In: *The Astrophysical Journal Letters* **783**, L32.

Smith, R. J., J. R. Lucey, and A. C. Edge (2017). "Stellar dynamics in the strong-lensing central galaxy of Abell 1201: a low stellar mass-to-light ratio, a large central compact mass and a standard dark matter halo". In: *Monthly Notices of the Royal Astronomical Society* **471**, 383.

Thomas, J. et al. (2005). "Regularized orbit models unveiling the stellar structure and dark matter halo of the Coma elliptical NGC 4807". In: *Monthly Notices of the Royal Astronomical Society* **360**, 1355.

Tonry, J. L. (1985). "Observations of a complete sample of brightest cluster galaxies with multiple nuclei". In: *The Astronomical Journal* **90**, 12.

Treu, T. and L. V. E. Koopmans (2004). "Massive dark matter halos and evolution of early-type galaxies to $z \approx 1$". In: *The Astrophysical Journal* **611**, 739.

van de Sande, J. et al. (2017). "The SAMI galaxy survey: revisiting galaxy classification through high-order stellar kinematics". In: *The Astrophysical Journal* **835**, 104.

— (2021). "The SAMI galaxy survey: mass and environment as indipendent drivers of galaxy dynamics". In: *Monthly Notices of the Royal Astronomical Society* **508**, 2307.

Veale, M. et al. (2016). "The MASSIVE survey - V. Spatially-resolved stellar angular momentum, velocity dispersion, and higher moments of the 41 most massive local early-type galaxies". In: *Monthly Notices of the Royal Astronomical Society* **464**, 356.

— (2017). "The MASSIVE survey – VII. The relationship of angular momentum, stellar mass and environment of early-type galaxies". In: *Monthly Notices of the Royal Astronomical Society* **471**, 1428.

— (2018). "The MASSIVE survey – VIII. Stellar velocity dispersion profiles and environmental dependence of early-type galaxies". In: *Monthly Notices of the Royal Astronomical Society* **473**, 5446.